

Direction Selectivity and Receptive Fields of Zebrafish Tectal and Pretectal Neurons

Dissertation

zur Erlangung des Grades eines
Doktors der Naturwissenschaften

der Mathematisch-Naturwissenschaftlichen Fakultät
und
der Medizinischen Fakultät
der Eberhard-Karls-Universität Tübingen

vorgelegt

von

Kun Wang
aus Qian'an, China

März - 2020

Tag der mündlichen Prüfung:08.05.2020.....

Dekan der Math.-Nat. Fakultät: Prof. Dr. W. Rosenstiel

Dekan der Medizinischen Fakultät: Prof. Dr. T. Gasser

1. Berichterstatter: Prof. Dr. / PD Dr. / Dr.Aristides Arrenberg.....

2. Berichterstatter: Prof. Dr. / PD Dr. / Dr.Hanspeter A. Mallot.....

Prüfungskommission: Prof. Dr. / PD Dr. / Dr.Aristides Arrenberg.....

Prof. Dr. / PD Dr. / Dr.Hanspeter A. Mallot.....

Prof. Dr. / PD Dr. / Dr.Frank Schaeffel.....

Prof. Dr. / PD Dr. / Dr.Olga Garaschuk.....

Erklärung / Declaration:

Ich erkläre, dass ich die zur Promotion eingereichte Arbeit mit dem Titel:

„.....“
.....“

selbständig verfasst, nur die angegebenen Quellen und Hilfsmittel benutzt und wörtlich oder inhaltlich übernommene Stellen als solche gekennzeichnet habe. Ich versichere an Eides statt, dass diese Angaben wahr sind und dass ich nichts verschwiegen habe. Mir ist bekannt, dass die falsche Abgabe einer Versicherung an Eides statt mit Freiheitsstrafe bis zu drei Jahren oder mit Geldstrafe bestraft wird.

I hereby declare that I have produced the work entitled “.....”, submitted for the award of a doctorate, on my own (without external help), have used only the sources and aids indicated and have marked passages included from other works, whether verbatim or in content, as such. I swear upon oath that these statements are true and that I have not concealed anything. I am aware that making a false declaration under oath is punishable by a term of imprisonment of up to three years or by a fine.

Tübingen, den

.....

Datum / Date

Unterschrift /Signature

Table of Contents

Abstract	1
Introduction	3
<i>Optic flow</i>	3
<i>Accessory optic system</i>	4
<i>Optokinetic response (OKR)</i>	8
<i>Optomotor response (OMR)</i>	8
<i>Calcium imaging</i>	10
<i>Zebrafish are emerging as an ideal model organism for visual neuroscience</i>	11
<i>Receptive field</i>	13
<i>DS cells in zebrafish optic tectum</i>	15
<i>Binocular neurons in the AOS and pretectum</i>	16
Project goals	20
Discussions	23
<i>Both tectal and pretectal neurons are each tuned to one of the four preferred directions</i>	23
<i>Tectal RFs are relatively small and bias to the upper nasal view field</i>	24

<i>Pretectal neurons have large-size RFs and bias to the ventral visual field</i>	25
<i>Three rotational/translational axes are represented by the tectal and pretectal binocular neurons</i>	25
<i>The optomotor response is driven strongest by motion in the lower-temporal visual field</i>	26
Limitation of the experiments	28
<u>Reflections of the experimental setup</u>	28
<u>Limited whole view field</u>	31
<u>Drifting of the fish along z axis during calcium imaging recordings</u>	32
<u>RFs were mapped only with horizontally moving gratings monocularly</u>	34
<u>Limitation of the visual stimulus size in the RF mapping experiment</u>	34
<u>Two-dimensional Gaussian fitting of receptive fields</u>	36
<u>Indirect measurement of the inhibitory RFs</u>	38
<u>Limitations of the binocular DS data</u>	39
<u>Defining the brain region of pretectum</u>	40
Future directions	43
List of papers/manuscripts	45
Statement of contributions	46
Acknowledgements	49
Reference	51

Appendix.....	65
<i>Abbreviation.....</i>	<i>65</i>
<i>Appended mathematical equations.....</i>	<i>66</i>
<i>Appended papers/manuscripts.....</i>	<i>67</i>

Abstract

Optic flow processing by neurons in the diencephalic pretectum is essential for visually guided behaviours in vertebrates, such as the optokinetic and optomotor responses. Animals actively stabilize both their gaze and position relative to their surroundings when exposed to translational and rotational stimuli. Recently, pretectal neurons distinguishing these moving patterns have been identified in the zebrafish brain and they are thought to mediate downstream motor outputs. It is still unclear whether binocular stimulus motion in other planes besides the horizontal plane is also represented in the zebrafish brain. Furthermore, while receptive field sizes and centres of tectal neurons have been reported, those of zebrafish pretectal neurons remain mainly elusive. We elucidate these crucial features with *in vivo* calcium imaging.

First, we find that both pretectal and tectal neurons are each tuned to one out of four (roughly equally spaced) preferred directions. No anatomical segregation of direction-selective tectal neurons was identified. Second, we identified neurons responding to specific translational or rotational whole-field patterns by presenting all possible binocular combinations of the four (monocularly) preferred stimulus directions to both eyes of the fish. These binocular selective neurons could – in principle – directly instruct appropriate compensatory eye and tail movements during optokinetic and optomotor behaviour, respectively.

Furthermore, monocular receptive field mapping shows that the vast majority of tectal motion-sensitive neurons are tuned to small-size motion, many with reduced neural activities when the motion-covered region increases. The visual space of the small-size tectal receptive fields is over-represented in the nasal-dorsal visual field. In contrast, many pretectal neurons have large-sized receptive fields ($> 60^\circ \times 30^\circ$, in azimuth, and elevation) with centres of receptive fields in the ventral visual field. Finally, besides full-field motion, the larval zebrafish optomotor response was preferably evoked by binocular forward translational motion located in the ventral temporal visual field, which mainly overlaps with the receptive field centres of the pretectal large-size receptive fields.

Our study characterizes fundamental features of tectal and pretectal information processing and provides the basis for further investigations into visuomotor transformations in zebrafish.

Introduction

Optic flow

Optic flow results from the relative motion of an observer (an animal or a camera) to the visual scene. It is the vector field of the apparent motion of objects or surfaces in the visual scene (Figure 1A) (Gibson, 1950; Serres and Ruffier, 2017). The patterns of the optic flow can be very complex depending on the relative motion. In principle, the patterns of the optic flow can be decomposed into rotational and translational motions (Figure 1B-D) (Koenderink and van Doorn, 1987).

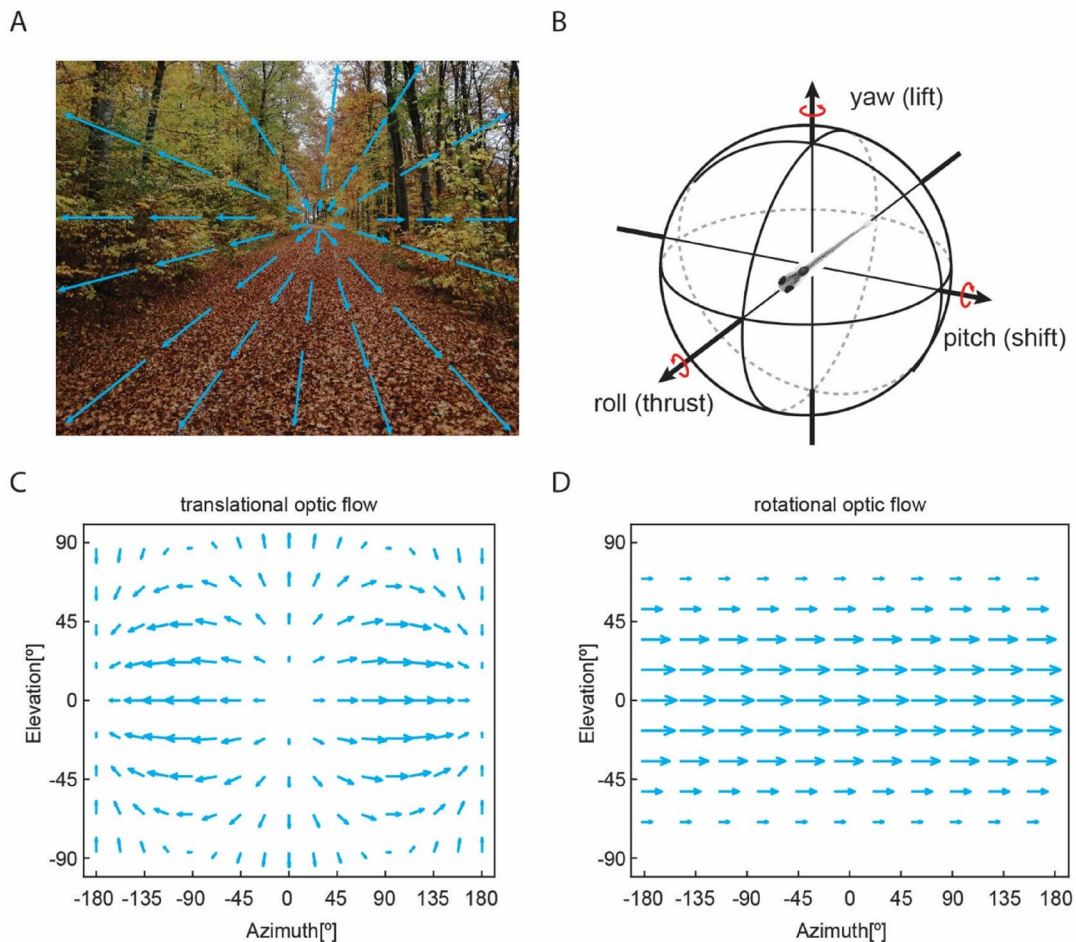


Figure 1. Optic flow patterns during translational and rotational ego-motion. (A) Optic flow generated when approaching an object via forward translational motion. The arrows indicate the velocity vectors of image points projected onto the retina. The whole moving pattern of the optic flow expanded from the location of the target (focus of expansion). (B) Three axes in the three dimensional Cartesian coordinate system with a larval zebrafish in the centre of the sphere. The corresponding

rotational and translational motions around/along these axes are yaw/lift, roll/thrust and pitch/shift axes. These three axes are represented by black arrows and the rotational motions are indicated with red curved arrows. (C) and (D) Two basic optic flow patterns (azimuth, $[-180^\circ, 180^\circ]$; elevation, $[-90^\circ, 90^\circ]$) generated by forward translational motion and rotational movement around the yaw axis, respectively. In panel (C), the motion expands from the focus of expansion $[0^\circ, 0^\circ]$ with increasing velocity and retracts on the opposite side $[180^\circ, 0^\circ]$. In panel (D), the velocity increases from North pole (90° in elevation) to the equator (0° in elevation), then reduces to zero at the South pole (-90° in elevation). On the same elevation level, the velocity is constant for all the azimuth angles.

Through the optic flow, animals can perceive their own locomotion, actively adjust their trajectory and navigate in the environment (Baird et al., 2011; Cabrera and Theobald, 2013; Serres and Ruffier, 2017). The ratio between the relative linear speed of the visual scene from the perspective of the observer and the distance between the observer and obstacles in the surrounding environment is a key factor for translation optic flow. Several hypothetical mechanisms underlying the optic flow-based guidance of navigation have been proposed, though the neural circuits are mainly unclear (Serres and Ruffier, 2017). On the other hand, animals perform compensatory behaviours such as optokinetic and optomotor responses (OKR and OMR), to stabilize the images on the retina (counteract the retinal slip) when exposed to moving surroundings (Eckmeier and Bischof, 2008; Lappe et al., 1998; Masseck et al., 2010; Miles and Busetini, 1992; Najafian et al., 2014). The corresponding sensory neural circuits are mainly located in the vertebrate accessory optic system (or pretectum for fish), but the detailed neural mechanisms mainly remain elusive.

Accessory optic system

The accessory optic system (AOS) is a primary visual system present in all vertebrates, including humans (Clement and Magnin, 1984; Fredericks et al., 1988; Kubo et al., 2014; Simpson, 1984; Wylie, 2000). In mammalian brains, the AOS is located in the dorsal midbrain anterior to the superior colliculus (SC) (Simpson, 1984) and receives direct retinal input from both ON-retinal ganglion cells (ON-RGCs) and a subpopulation of ON-OFF-retinal

ganglion cells (ON-OFF-RGCs) (Oyster et al., 1980). Most of the ON-RGCs are direction selective (DS) and each is tuned to low speed motion in one of the three different preferred directions (PDs, shown in Figure 2, middle bottom) (Borst and Euler, 2011; Oyster and Barlow, 1967). The mammalian AOS, responsive to optic flow like fish pretectum, contains several neural clusters, the dorsal terminal nucleus (DTN), lateral terminal nucleus (LTN) and medial terminal nucleus (MTN), each composed of neurons with a distinct directional preference (Giolli et al., 2006; Masseck and Hoffmann, 2009a). Due to the functional similarities, the pretectal nucleus of the optic tract (NOT), which is direction selective to ipsiversive motion, and the DTN are regarded as one functional entity, known as NOT-DTN (Figure 3C). However, these mammalian AOS neurons only represent three directions, lacking of contraversive direction in each hemisphere (Masseck and Hoffmann, 2009a). Functionally, consistent with the PDs of the nuclei, innervation of the DTN/NOT induces horizontal OKRs (hOKRs). For example, electrical stimulation and pharmacological inactivation of the NOT-DTN exclusively induced hOKRs with ipsiversive slow phases but did not influence the vertical eye position (Hoffmann and Fischer, 2001). Similarly, only vertical OKRs (vOKRs) were evoked by the stimulation of the LTN-MTN.

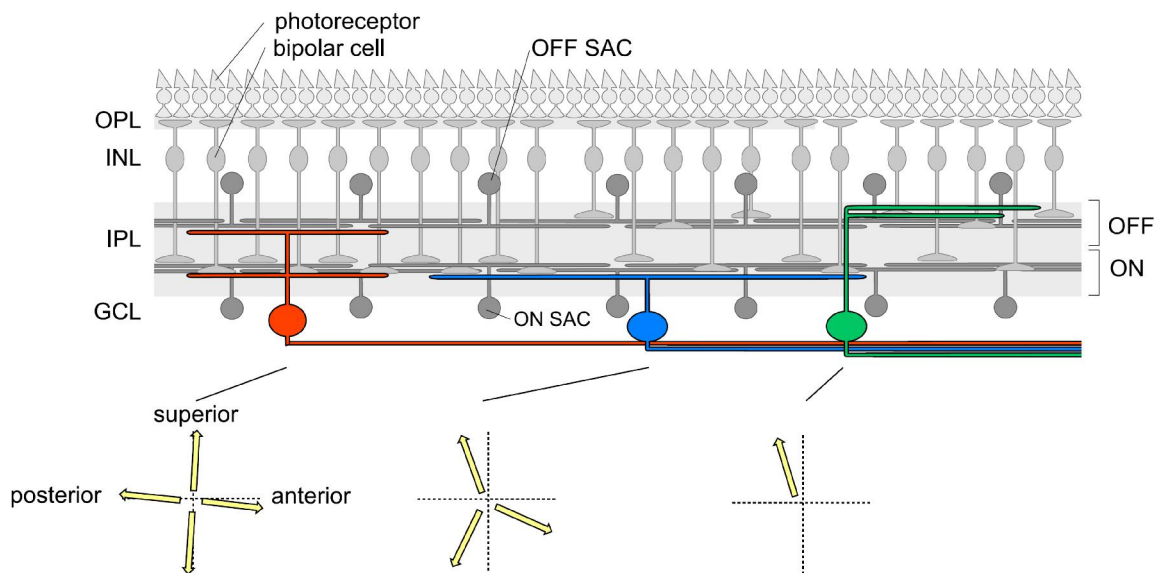


Figure 2. Diagram section (vertical) of the retina with the dendritic stratification of three types of DS (ON/OFF-DS, ON-DS, and OFF-DS) cells. The preferred directions of motion with respect to the visual field for each (sub-)types are indicated below. SAC, starburst amacrine cell; OPL, outer plexiform

layer; INL, inner nuclear layer; IPL, inner plexiform layer; GCL, ganglion cell layer. (adapted from Figure 3D of Borst and Euler, 2011)

The AOS projects to various brain areas, including inferior olive (IO), vestibular nuclei and the basal pontine nuclei (Giolli et al., 2006). For example, the direct AOS–olivary pathway of the rabbit MTN conveys visual/optokinetic signals from the MTN through the IO to the Purkinje cells of the cerebellar flocculus (Giolli et al., 2006).

In amphibians, reptiles and birds, similarly, the AOS contains two nuclei. The pretectal nucleus lentiformis mesencephalic (LM) encodes the ipsiversive motion, homologous to the mammalian NOT-DTN (Masseck and Hoffmann, 2009a; Xiao and Frost, 2009). The other nucleus, the tegmental nucleus of the basal optic root (nBOR) responds to the movements in the other three directions (Figure 3B), as the counterpart of LTN and MTN in mammals. However, the fish pretectal neurons in one specific region, representing the AOS of tetrapod, were also direction selective but showed no functionally separated nuclei (Figure 3A) (Klar and Hoffmann, 2002; Masseck and Hoffmann, 2009a).

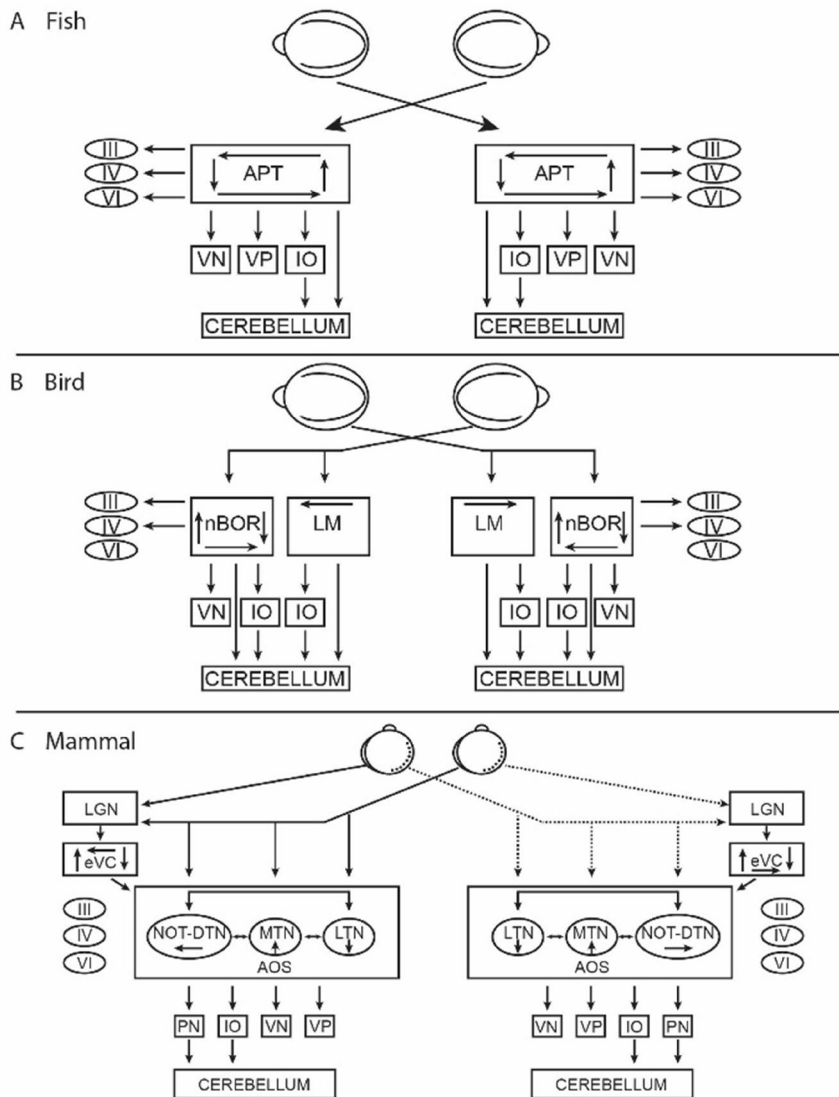


Figure 3. Neural circuit of OKR in fish (A), birds (B), representing non-mammalian tetrapod, and frontal-eyed mammals (C). Arrows between the boxes represent confirmed anatomical connections. (A) Arrows in the box APT indicate that neurons represented all the four moving directions in the left as well as in the right nucleus. (B) The two boxes indicate that the monocular moving directions are separately represented by two different nuclei, LM mainly encoding ipsiversive motion and nBOR representing contraversive, up and down directions of stimulus movement on the contralateral side. (C) Arrows in the circles NOT-DTN, LTN, and MTN show that only stimulus movement in ipsiversive, downward or upward directions are represented by neurons in these nuclei respectively. III, nucleus oculomotorius; IV, nucleus trochlearis; VI, nucleus abducens. APT, area pretecalis; eVC, extrastriate visual cortex; IO, inferior olive; LGN, lateral geniculate nucleus; PN, pontine nuclei; VP, velocity-to-position integrator; VN, vestibular nuclei; The figure is adapted based on the Figure 1 in (Masseck and Hoffmann, 2009a).

Optokinetic response (OKR)

OKR is an innate reflexive eye movement behaviour induced by whole-field rotational visual motion (Tauber and Atkin, 1968). The behaviour is evolutionally highly conserved across the vertebrates in spite of species specialisations (Masseck and Hoffmann, 2009a). OKR is composed of two different eye movement phases. The slow phase is characterized with the smooth eye movement pursuing the moving visual stimulus to counteract the retinal slip of the images. When the eyes moved to the extreme position at the end of the slow phase, the fast phase (saccade) during which the eyes were reset rapidly back to the initial eye position started (Figure 4) (Masseck and Hoffmann, 2009a; Mueller and Neuhauss, 2010; Tauber and Atkin, 1968). The gain (eye velocity over the velocity of the stimulus) during the slow phase is mainly influenced by the contrast, spatial and temporal frequencies of the visual stimulus (Rinner et al., 2005).

The amplitude of the OKR eye movement varies much among different species. While other animals, such as birds, maintain their visual stabilization mainly with head rotation, fish and mammals rely predominantly on the OKR. In most species, the amplitude of OKR is asymmetrical regarding the horizontal moving direction of the visual stimulus. Motion in the temporal-nasal (TN) direction induced larger eye movement than motion in the opposite direction (Knapp et al., 2013; Masseck and Hoffmann, 2009a; Matsuo and Cohen, 1984).

Optomotor response (OMR)

The optomotor response (OMR) is the stereo-typed locomotor behaviour of an animal following the translational shifting visual patterns to maintain the body location relative to the moving surroundings and counteract the retinal slip (Figure 4) (Arnold, 1974; Krauss and Neumeyer, 2003; Pflugfelder and Heisenberg, 1995). The OMR has been reported in different animal species, including insects, fish, salamander, mice and humans (Besharse and A. Brandon, 1973; Kretschmer et al., 2017; Orger and Baier, 2005; Tauber and Koffler,

1966; Theobald et al., 2010). In zebrafish, the OMR behaviour is visually induced by forward translational motion and tuned preferably to moving patterns with low spatial and temporal frequencies (Maaswinkel and Li, 2003).

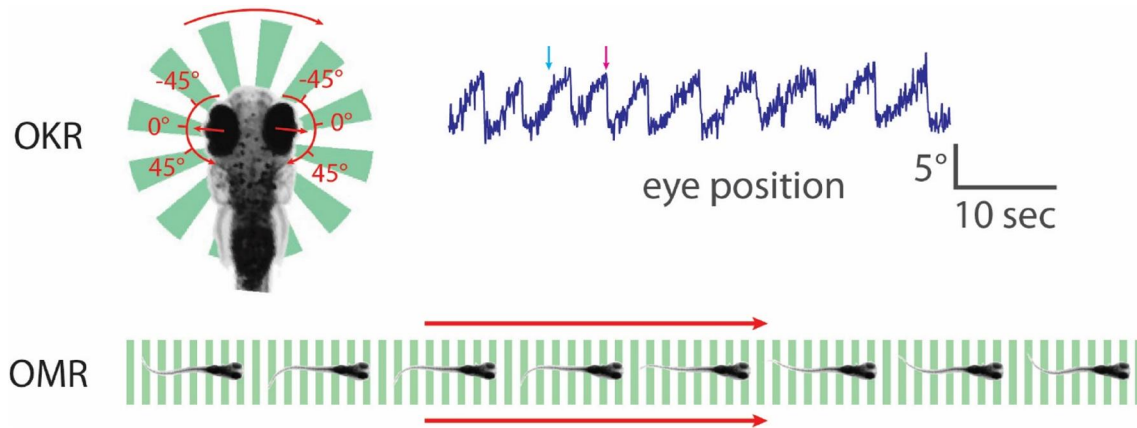


Figure 4. Schematics of larval zebrafish OKR and OMR. Upper panel, a larval zebrafish embedded in low melting agarose was presented with clockwise rotational visual stimulus from below indicated by the green bars. The rotational direction is indicated with the red curved arrow. The movement of the eyes was monitored with an infrared camera and the (angular) position of the right eye was plotted on the right side. The cyan and magenta arrows indicate a slow eye movement phase and a saccade, respectively. The eye position curve in blue is adapted from (Dehmelt et al., 2018). Bottom panel, a free-swimming larval zebrafish was stimulated with forward translational gratings from below. The larva followed after the motion to the right side as indicated by the red arrows.

The sensory neurons underlying the invertebrate OMR neural network have been widely investigated. The tangential horizontal system (HS) cells in drosophila are direction selective to the motion in the front-to-back direction and are suppressed by the motion in the opposite direction (Schnell et al., 2010). These neurons have been reported to be crucial for the OMR. The HS cells defective mutants and flies whose HS cells axons were cut off showed much weaker optomotor response (K. Hausen and Wehrhahn, 1983; M. Heisenberg et al., 1978). Particularly, optogenetic manipulation of the HS cells were able to elicit robust head tuning behaviour in free-moving drosophila (Haikala et al., 2013). In contrast, the neural circuitry underlying the vertebrate OMR is mainly unclear, though optic tectum (OT) and pretectum of

fish have been reported to be involved in the OMR and binocular forward motion selective neurons were identified in the fish pretectum (Kubo et al., 2014; Naumann et al., 2016; Springer AD et al., 1977).

On the retinal level, vertebrate L-cone photoreceptors and ON-RGCs dominate the OMR. Therefore, the zebrafish OMR depends on the wavelength with a peak around 550-600 nm and 'colour-blind' (Krauss and Neumeier, 2003; Schaerer and Neumeier, 1996).

Calcium imaging

Calcium ions are universal second messengers in the cells and play vital roles in various physiological processes, ranging from neuronal signalling and exocytosis to muscle contraction and bone formation (Barclay et al., 2005; Jiang and Stephens, 1994; Paredes et al., 2008). For example, the calcium ions flow into neurons upon the depolarization of the cellular membrane and the calcium concentration increases dramatically in the cytosol (Rosen et al., 1994). In the presynaptic zone, high concentration of calcium triggers the release of vesicles and neurotransmitters (Kyoung et al., 2013).

Chemical calcium indicators, usually small molecules based on BAPTA, bind to calcium ions and emit fluorescence upon light excitation (Nakai et al., 2001; Paredes et al., 2008). Through the changes of the fluorescence, neural activities of the neurons can be reliably read out. Chemical indicators and genetically encoded calcium indicators (GECI) are widely used in the field of neuroscience (Stosiek et al., 2003; Tian et al., 2012). But the former has several disadvantages. First of all, invasive injection of the indicators into the animal or tissue is required, which is elaborate and harmful to the experimental organism (Niell and Smith, 2005; Tischbirek et al., 2015). Second, the chemical indicators tend to compartmentalize and are finally extruded from the cell during long recordings, allowing functional recordings only for a couple of hours (Paredes et al., 2008).

In comparison, GECI can be specifically, stably or inheritably expressed in the tissues or cells with genetic modification (Figure 5) (Muto and Kawakami, 2011; Muto et al., 2011). GCaMP is a GECI and established based on the green fluorescent protein (GFP). GCaMP binds to or releases the calcium ions upon calcium concentration changes in the neurons and emits green fluorescence (Figure 5) (Nakai et al., 2001). Red fluorescent protein (RFP)-based GECIs, which are applicable in deeper tissue and enable multicolour visualization, lead to new applications recently (Shen et al., 2018).

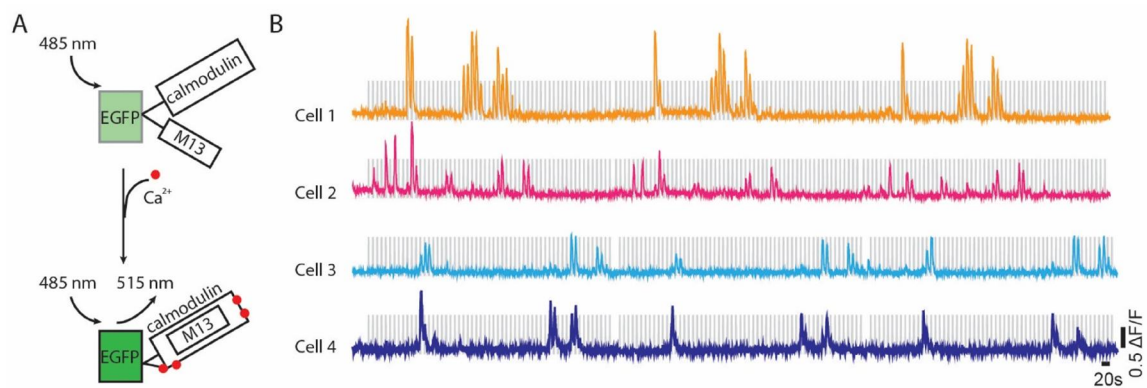


Figure 5. A schematic of GCaMP binding to calcium ions and emitting light. (A) The conformational change of GCaMP protein in presence of Ca^{2+} . M13, a peptide sequence from myosin light chain kinase. Adapted from (Grienberger and Konnerth, 2012). **(B)** Calcium traces from four cells recorded with 2-Photon microscopy. The curves in colors are the $\Delta F/F$ and the grey background indicates the motion and stationary phases of the visual stimulus to the neurons.

Zebrafish are emerging as an ideal model organism for visual neuroscience

Zebrafish (*Danio rerio*) are tropical freshwater fish originating from South Asia. The adult fish are around 1.8-3.7 centimetres long and preferably live in the shallow streams and rivers (Engeszer et al., 2007). Owing to easy genetic modification and fast development, zebrafish have been widely used in genetic and biological developmental research (Irion et al., 2014; Ma et al., 2016; Xiao et al., 2005). In the last decades, many inheritable mutants and transgenic fish lines have been screened or established for different studies (Muto et al., 2005; Scott and Baier, 2009). For example, nacre mutants are transparent, which makes

them a perfect model for *in vivo* microscopy and non-invasive optogenetic manipulation (Lister et al., 1999). Genetically encoded calcium indicators (GECI) have been widely used in the research of neuronal encoding in intact larval zebrafish as well (Ahrens et al., 2013b; Kubo et al., 2014; Muto and Kawakami, 2011; Naumann et al., 2016).

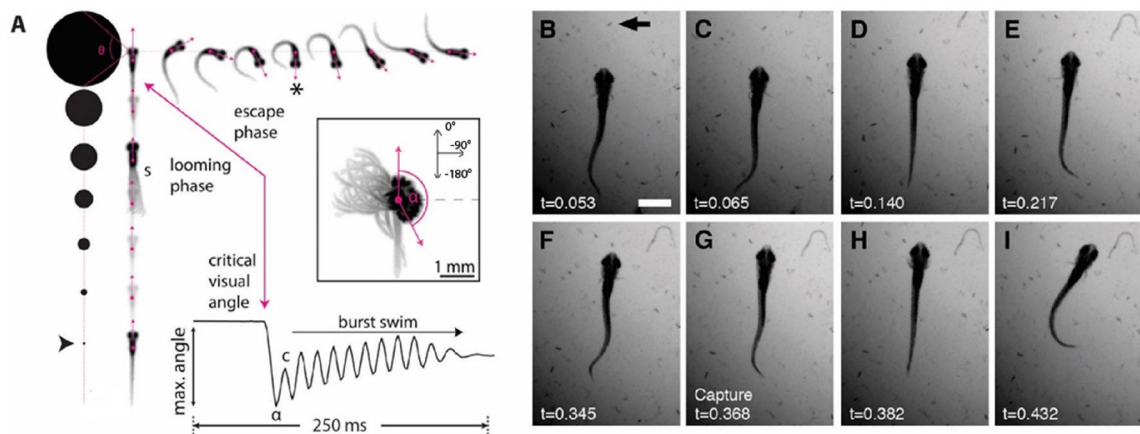


Figure 6. Looming-induced larval escape response and small moving dots evoked prey capture behaviour in zebrafish. (A) Looming visual stimulus induced escape behaviour of a larval zebrafish. A large-angle, long-distance escape response towards the right side was evoked when a looming disk expanded in the left visual field. The direction of the fish head or body axis (relative to vertical up direction; vertical up direction corresponds to 0° and the value decreases clockwise) was represented by the α angle. When the critical visual angle (Θ) of the looming disk is reached (indicated with the magenta arrow), the fish turned to the right immediately with a high angle velocity. The centre of the looming visual stimulus is 1 cm away from the fish. The figure is adapted from (Dunn et al., 2016). (B-I) A maneuver of prey capture behaviour of a larval zebrafish. The black arrow indicates the prey, a swimming paramecium. The figure is adapted from (McClenahan et al., 2012).

Zebrafish navigate in the environment and hunt for prey mainly depending on their vision (Figure 6) (Burgess et al., 2010; Gahtan et al., 2005). The visual system of zebrafish develops and matures rather fast. As early as 4 days post fertilization (dpf), the larvae showed stable OKR behaviour evoked with rotational motion (Brockerhoff, 2006). Meanwhile, they start hunting swimming paramecia actively guided by the visual system (Muto and Kawakami, 2013). By 5 dpf, the OKR behaviour can be used in the laboratory for the mutant screening and visual function study in larval zebrafish (Huber-Reggi et al., 2013). The

development of the OMR behaviour is relatively slower, and most of larvae show OMR, following the forward translational moving gratings, reliably on 7 dpf (Fleisch and Neuhauss, 2006; Orger and Baier, 2005).

With various behavioural readouts and the availability of *in vivo* functional calcium imaging with cellular resolution, zebrafish are emerging as an important animal model for visual neuroscience (Ahrens et al., 2013b; Huang and Neuhauss, 2008; Robles et al., 2014).

Receptive field

Visual receptive fields (RFs) are regions within the visual field in which the visual stimulus changes the neuronal firing status (Figure 7A) (Spillmann, 2014). The shape and size of the RFs vary among neurons from the retinal ganglion cells to the cortical neurons in the brain, and the diversity is considered as the basis of visual functions (Hirsch, 2003). For example, the RFs of the simple cells from the primary visual cortex (V1) of monkeys and cats are elongated with a narrow excitatory centre and inhibitory flanks (often asymmetric) in the surround or vice versa (Field and Tolhurst, 1986; Hamilton et al., 1989). These antagonistic arrangements enable the simple cell RFs to optimally detect lines, bars, and edges (Hubel and Wiesel, 1968; Ringach, 2004; Ringach et al., 2002).

In adult zebrafish, the average RF size of the tectal neurons is relatively small, ranging from 25 to 39 degrees (Sajovic and Levinthal, 1982). Furthermore, the tectal RFs from larval zebrafish are even smaller as revealed with calcium imaging method. Some of these neurons selectively responded to small-size moving objects of 2° (Preuss et al., 2014). During the early development of the larval zebrafish, tectal RF sizes increase from 4 to 6 dpf and then undergo refinement afterwards. As a result, the RF sizes at 4 dpf and 8 to 9 dpf are similar to each other (Figure 7B) (Zhang et al., 2011).

In comparison, neurons from the tetrapod AOS and teleost pretectum have large RFs with broad DS tuning curves (Figure 7C) (Britto et al., 1981; Grasse and Cynader, 1984; Masseck

and Hoffmann, 2008; Simpson, 1984; Walley, 1967). The RFs even cover nearly the whole lower view field of the contralateral eye (Masseck and Hoffmann, 2008). These AOS and pretectal neurons process optic flow and drive compensatory behaviours to control body posture and stabilize the gaze via OMR and OKR (Giolli et al., 2006; Kubo et al., 2014; Lazar, 1972; McKenna and Wallman, 1985; Naumann et al., 2016).

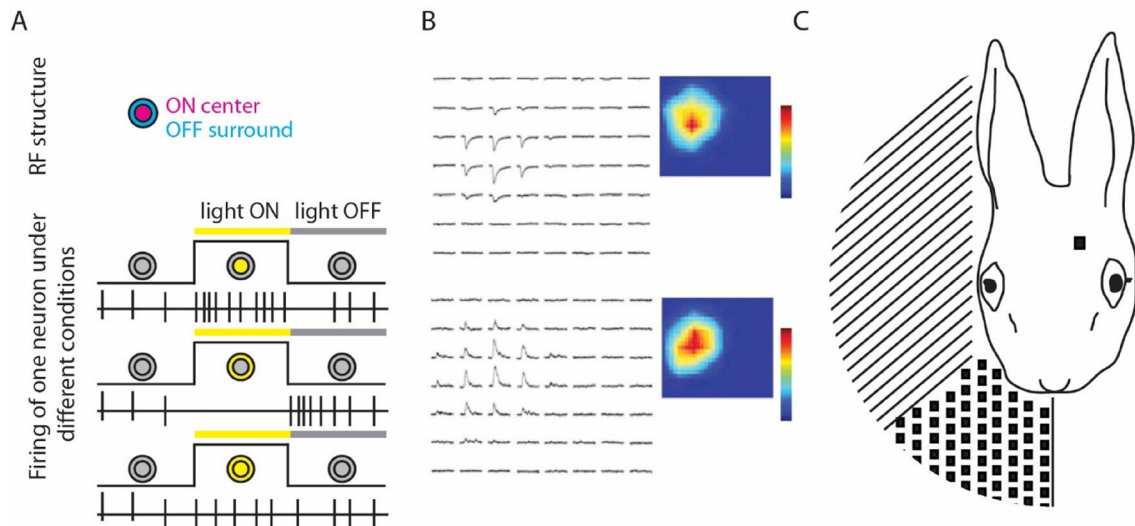


Figure 7. (A) A schematic of an ON-centre, OFF-surround retinal ganglion cell. Upper, the structure of the RF from a neuron. The centre of the RF responds to increase of light intensity and the surround to reduce of light intensity. Bottom, responses of the neuron above stimulated with three different protocols. The neuron responded maximally when the ON-centre is stimulated with increase of the light intensity. On the contrary, the firing frequency of this neuron drops dramatically when the increase of the light intensity occurs exclusively within OFF-surround region. The firing frequency is between those under the first two conditions when both the ON-centre and OFF-surround regions are stimulated with light intensity increase. Yellow colour indicates light ON. Vertical bars below represent single action potentials. (B) Light ON (upper) and OFF (bottom) receptive fields of one zebrafish tectal neuron (8 dpf) recorded with patch clamp. The original responses evoked by small-size light ON/OFF patches were plotted on the left side (adapted from (Zhang et al., 2011)) and the interpolated heat maps are on the right. 56 small light ON-OFF stimulus patches were used to evoke the neuron activities corresponding to the 7 x 8 signal matrix. (C) The large-size receptive field of one neuron recorded from a rabbit median lateral nucleus. The strips and small rectangles covered the receptive field sub-regions with opposite preferred directions. The black square on the rabbit head indicates the recorded brain region (adapted from (Simpson et al., 1988b)).

DS cells in zebrafish optic tectum

Direction selectivity is a fundamental mechanism for motion perception (Mateeff et al., 1991; Pasternak, 1986). Direction selective (DS) cells discharge robustly when a stimulus moves through the RF of the cells in a certain direction and discharge weakly or even stop firing to motions in other directions (Figure 8A) (Barlow and Levick, 1965). DS neurons are also frequent in zebrafish tectum, one of the primary retino-recipient brain regions of retina ganglion cells (RGCs) (Burrill and Easter, 1994). Previous studies have identified four subtypes of DS neuron groups, with an overlapping cardinal direction representation in zebrafish stratum periventriculare (SPV) (Hunter et al., 2013), although another research showed all directions were represented, with a preponderance of nasal-ward motion in the tectum (Niell and Smith, 2005). The four PDs of the periventricular neurons (PVNs) are nearly parallel to the rostro-caudal and dorsal-ventral axes (Figure 8B). However, the direction space is represented by three functional subtypes of RGCs with triangularly distributed tiled tuning curves. In the retinae of mammals, on the contrary, the direction space of the ON-OFF-RGCs is represented with four PDs, similar to the space representation of zebrafish tectal neurons. But the “ON” DS cells, which are sensitive to the whole field motion, only have three PDs like zebrafish RGCs (Oyster and Barlow, 1967). PD differently tuned tectal neurons showed stereotypic, different projecting laminae in the tectal neuropil (Lowe et al., 2013). They receive excitatory input from the neuropil layers where the PDs have been represented. Also, tectal neurons representing different directions seem to be equally distributed spatially (Masseck and Hoffmann, 2009a; Niell and Smith, 2005).

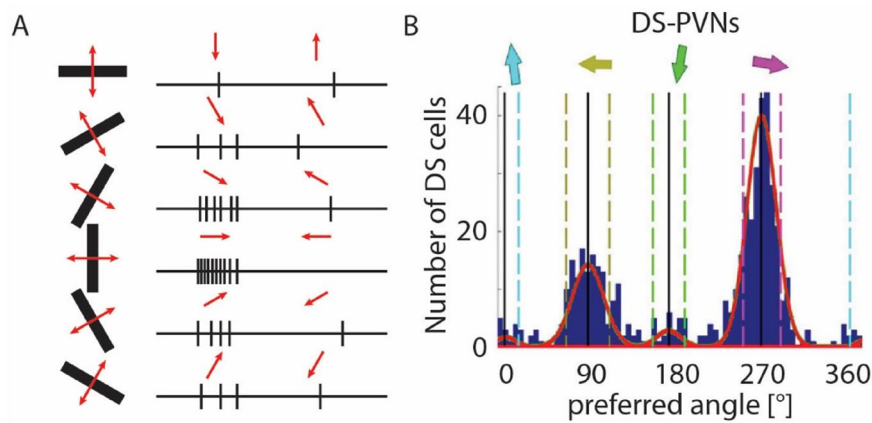


Figure 8. (A) A schematic of the firing frequency of a direction selective neuron stimulated with a bar moving in different directions. The moving directions, orthogonal to the black bar, are indicated by the red arrows. The small vertical black bars on the right side represent action potentials. (B) Histogram analysis of the preferred directions of the zebrafish direction selective periventricular neurons (DS-PVN). The total number of the neurons was fitted with a four-peak Von Mises function shown in red. The four preferred directions were indicated with coloured arrows on the top (adapted from (Hunter et al., 2013)).

Binocular neurons in the AOS and pretectum

Intriguingly, various types of binocular neurons were also identified in the tetrapod AOS and teleost pretectum, despite the completely crossed projection of the optic nerves in non-mammalian vertebrates (Manteuffel, 1984, 1987; Wylie, 2000). These neurons are direction selective to translational or rotational visual stimuli with PDs or preferred axes (PAs). In many species, such as rabbits, pigeons and goldfish, the PDs and PAs of AOS and pretectal binocular neurons are parallel or orthogonal to the internal reference frame shared by the extraocular muscles and vestibular canals, respectively (Figure 7C, 9A, B and C) (Masseck and Hoffmann, 2009b; Simpson et al., 1988a, b; Wylie and Frost, 1996). Binocular DS neurons responsive to motion in the horizontal plane are also found in the larval zebrafish pretectum. Some of forward motion selective neurons are exclusively activated by forward translational motion from both sides. And other forward motion selective neurons are also responsive to monocular visual stimuli and inhibited by rotational motion. These results indicate that the horizontally rotational and translational movements can be distinguished by

the pretectal sensory neurons, which are likely to relay the information to motor control units and affect motor outputs (Kubo et al., 2014). Besides, roll and pitch rotational selective pretectal neurons have been recorded from dogfish (Masseck and Hoffmann, 2008). It still remains unknown whether zebrafish also have these kinds of neurons or up- and downward binocular selective neurons to differentiate translational and rotational movements.

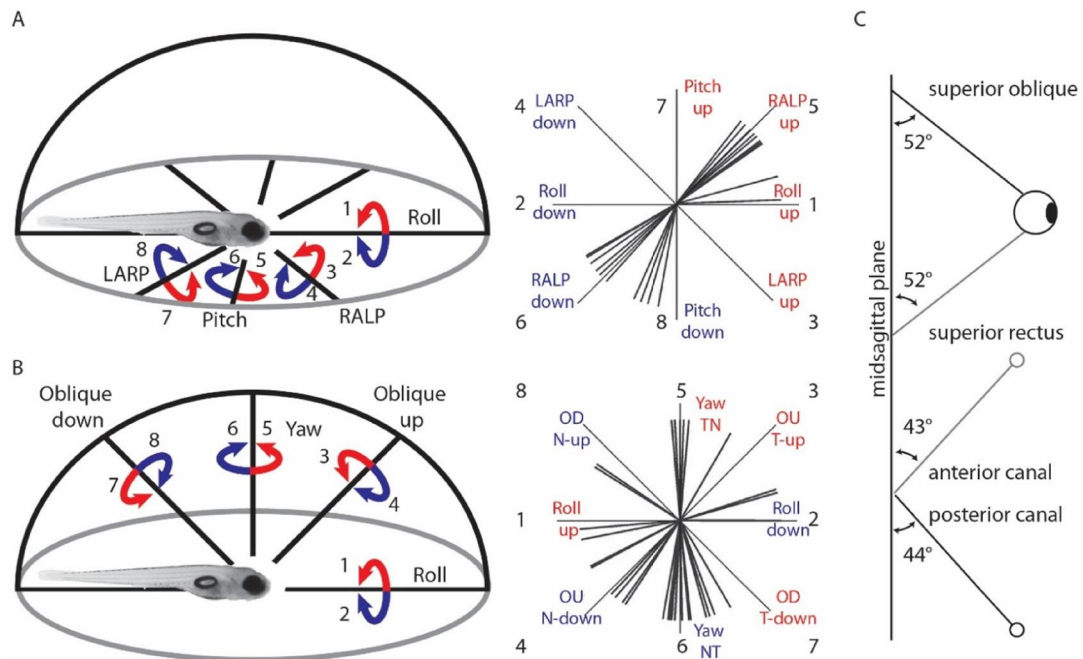


Figure 9. (A) Left, four rotational optic flow axes in the horizontal plane were tested by (Masseck and Hoffmann, 2009b) from the goldfish pretectum. The tested rotational axes are 45° apart from neighbouring axes. RALP, right anterior left posterior; LARP, left anterior right posterior. The rotational directions are labelled with blue and red arrows. To illustrate the directions explicitly, all the arrows are assigned with a single number corresponding to the numbers on the right side. Right, distribution of preferred axes of direction-selective neurons stimulated with axes in the horizontal plane. Each line indicates the preferred rotational axis of a single neuron. Additional notations refer to the optic flow moving direction sensed by the nasal visual field of the right eye (neurons were recorded from the left pretectum). For instance, 'RALP up' means clockwise rotational motion along the right anterior left posterior axis from the perspective of the fish. In the nasal visual field of the right eye, the moving direction is 'upwards'. The letter colours and the numbers correspond to those on the left side. (B) Left, four rotational optic flow axes in the midsagittal plane were tested by (Masseck and Hoffmann, 2009b) from the goldfish pretectum. The tested rotational axes are 45° apart from neighbouring axes. Right, distribution of preferred axes of direction-selective neurons stimulated with axes in the midsagittal plane. Each line indicates the preferred rotational axis of a single neuron. The letter colours and the numbers correspond to those on the left side. Roll up and down, roll motion

around the anterior-posterior axis. 'Up' and 'down' refer to the moving direction of the optic flow in the nasal visual field of the right eye. Yaw NT and TN, yaw motion in the nasaltemporal (NT) and temporalnasal (TN) directions to the right eye. OU T-up and N-down, motion along the oblique up axis from nasal-down to the temporal-up region and from temporal-up to nasal-down region, respectively. OD N-up and T-down, motion along the oblique down axis from temporal-down to the nasal-up region and from nasal-up to temporal -down region, respectively. (C) Spatial orientation of the planes of the semi-circular canals and extraocular muscles planes in goldfish. (Figure 9 is adapted from (Masseck and Hoffmann, 2009b))

Like the monocular AOS and pretectal neurons, the binocular neurons also have quite large RFs and respond to specific binocular visual stimulus patterns (Simpson et al., 1988a). RFs of rabbit binocular neurons from the rostral dorsal cap are mainly larger than 225° in azimuth. Intriguingly, in the sub-regions divided by either of the vertical plane 45° apart from the midsagittal plane, the RFs often show bipartite profile with opposite PDs, making the binocular neurons ideal candidates to detect rotational motion (Figure 7C) (Simpson et al., 1988a, b). In zebrafish and lizards, some of the binocular cells were responsive to clockwise rotational visual stimuli with temporonasal (TN) and nasotemporal (NT) movements to ipsilateral and contralateral eyes respectively, while the forward moving patterns (NT to both eyes) strongly inhibited the activation of these cells (Figure 10) (Kubo et al., 2014; Manteuffel, 1987). Nonetheless, the sizes, location and PDs of the RFs from the binocular neurons and how the excitatory and inhibitory inputs are integrated into these neurons are still unknown.

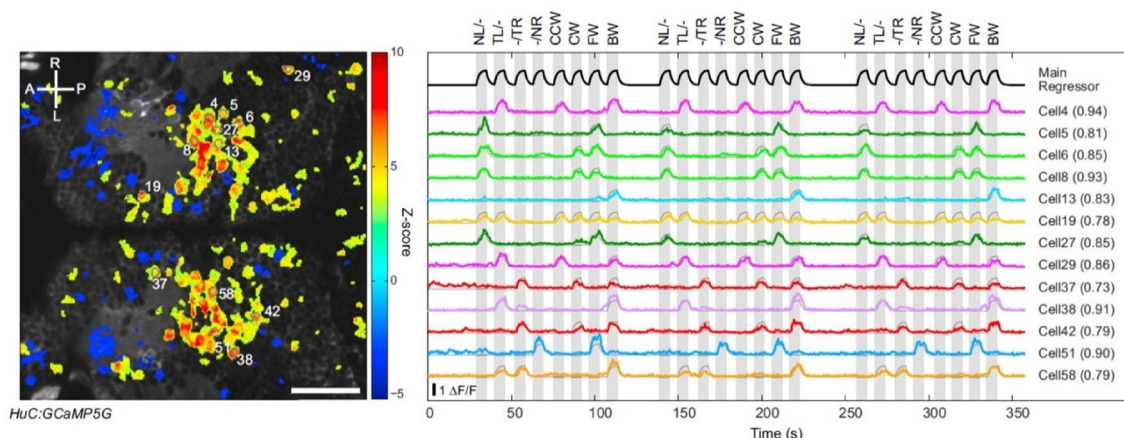


Figure 10. Calcium traces of responsive pretectal neurons to 8 different combinations of horizontal motion presented to both eyes of a larval zebrafish. Left side, Z-score map of one recording from zebrafish pretectum with motion-correlated pixels highlighted in warm colours. Right side, example fluorescence ($\Delta F/F$) traces (coloured lines) from the recording shown on the left. The eight different stimulus phases (represented by grey vertical bars) had three repetitions in each recording. The grey lines, overlaid on $\Delta F/F$ traces, are the best-performing regressor traces. Correlation coefficients calculated from the best regressors are shown in parentheses. A, anterior; P, posterior; R, right; L, left. NL/-, nasalward motion to left eye; TL/-, temporalward motion to left eye; -/TR, temporalward motion to right eye; -/NR, nasalward motion to right eye; CCW, counter-clockwise motion; CW, clockwise motion; FW, forward; BW, backward. Scale bar shows 50 μm . (adapted from (Kubo et al., 2014)).

Project goals

(1) What are the PDs of zebrafish pretectal neurons? Do pretectal and tectal neurons of zebrafish share the same spatial coordinate system?

While the tectal space is represented by four different directions, zebrafish retinal ganglion cells are directional selective to three different directions on the population level (Hunter et al., 2013). Certain directional transform mechanism is supposed to exist to mediate the changing of preferred directions between the tectum and neuropils (Abbas et al., 2017; Grama and Engert, 2012). The pretectum receives direct projections from retinal ganglion cells and is involved in both OKR and OMR behaviours, which are induced by large-size rotational and translational motion, respectively. Rotational and translational patterns are likely distinguished by direction selective pretectal neurons (Kubo et al., 2014). Mapping the pretectal directional space advances our understanding about the visual adaptations of animals to their natural habitats and life styles.

(2) Do RF sizes of zebrafish tectal and pretectal neurons differ? How are the RFs distributed in the whole visual field? And how do the shapes of the RFs look like?

Zebrafish tectal RFs are relatively small, ranging from 25°-39° in size. Pretectal RFs from zebrafish have not been studied yet. Given the large size of the pretectal RFs in other teleosts and that pretectum is involved in OKR behaviour, zebrafish pretectal RFs are most likely large as well.

In the primate superior colliculus, neurons encoding the upper visual field, in which higher spatial resolution is preferable for the animals in natural habitats, have smaller RFs and are more sensitive to image contrast than those encoding lower visual field, indicating the visual system adapts to the animals' living environment (Hafed and Chen, 2016). In addition, the

distribution of four types of photoreceptors has been shown to be highly asymmetrical in larval zebrafish retinae (Zimmermann et al., 2018).

(3) What kind of binocular rotational or translational selective neurons exist in the zebrafish tectum and pretectum? Which translational directions and rotational axes do these binocular neurons prefer?

The RF sizes of the tetrapod AOS and teleost pretectal neurons are relatively large (Masseck and Hoffmann, 2008; Simpson et al., 1988a). The sub-regions of the RFs from these neurons are oftentimes divided by the vertical plane along 45° in azimuth on either side of the brain hemisphere. Especially, the PDs in these adjacent sub-regions are opposite, indicating that the binocular neurons detect rotational motion, with the lines along 45° azimuthally in the horizontal plane as the PAs (Simpson et al., 1988a, b). Similarly, neurons encoding the translational or rotational optic flow respond best to the yaw axis and two horizontal axes orientated at 45° to either side of the body midline in pigeons (Wylie et al., 1998). Binocular neurons selective to rotation around the yaw axis or translational motion along the thrust axis have been identified in the zebrafish pretectum (Kubo et al., 2014). It is still unknown whether other rotational axes or translational directions are also represented by binocular selective neurons.

(4) Regarding the RFs, from which regions of the visual view does the binocular forward motion induce OMR behaviour most effectively?

Zebrafish OMR behaviour has been reliably induced with whole-field binocular forward motion projected to the animal both from sides and below (Naumann et al., 2016; Orger and Baier, 2005; Thiele et al., 2014). Zebrafish retinae, projecting to the pretectum directly, are highly asymmetric anatomically and functionally (Zimmermann et al., 2018). Though binocular motion presented below the equator line of the retina is obviously sufficient to

evoke the OMR behaviour (Naumann et al., 2016; Orger and Baier, 2005), the effective visual field of the zebrafish OMR behaviour is still unknown.

Discussion

Both tectal and pretectal neurons are each tuned to one of four preferred directions

Neurons from both tectum and pretectum are tuned to four PDs which are roughly parallel to the horizontal or vertical directions. Therefore, all the motion in a vertical plane can be represented or detected by these tectal or pretectal neurons. Moreover, the four PDs resemble the direction preferences of the tetrapod AOS neurons. While mammalian AOS neurons with different PDs are spatially distributed in various clusters, neurons with different PDs are intermingled in the zebrafish pretectum, same as the pretectal neurons in other fish (Klar and Hoffmann, 2002). On the retinal ganglion cell level, the directional space is represented by three PDs, but both the tectal and pretectal space shows four PDs (Hunter et al., 2013). Inhibitory neurons are involved in the spatial transformation of the PDs though the whole mechanism is still unclear (Grama and Engert, 2012; Sajovic and Levinthal, 1983).

Furthermore, each PD is represented by roughly the same number of neurons, which indicates that all the directions are equally represented by pretectum, without a clear bias. Given that pretectal neurons are involved in zebrafish OKR and OMR behaviours (Kubo et al., 2014; Naumann et al., 2016), these neurons likely send presynaptic inputs to more complex binocular rotational or transitional selective neurons which serve as the detectors of optic flow patterns and instruct behaviours.

Notably, in this monocular direction selective analysis experiment, only large-size whole-field motion stimulus was presented to the animals. Neurons selective to smaller-size motion are undetectable with our current experiment protocol (see our monocular receptive field mapping experiments). Also, the PDs were calculated from the data fitting of Von Mises distribution with only 8 data points (three repetitions), corresponding to neural responses to the moving gratings used in the experiment. Additionally, since the neural activities were recorded indirectly with GCaMP5G, due to the limitation of the calcium imaging method, the inhibitory effects in the null direction are also undetectable.

Tectal RFs are relatively small and bias to the upper nasal view field

Consistent with previous research results, the RFs of zebrafish tectal neurons are relatively small (Bergmann et al., 2018; Niell and Smith, 2005; Zhang et al., 2011). In adult zebrafish, the typical RF size of the neurons in the tectum ranges from 25 to 39 degrees and many tectal neurons were also strongly activated by small moving dots (Sajovic and Levinthal, 1982). In our current study, however, the smallest visual stimulus covered 30° x 13° (azimuth x elevation) in the visual field, which is too large for the measurement of the smallest RFs, given that larval tectal neurons, which were size-selective to moving visual stimulus of 2°, have been reported (Preuss et al., 2014).

Zebrafish tectum has been reported to be involved in the prey capture behaviour. Larval zebrafish prefer to hunt swimming preys located above the visual field equator, in front and within 60° temporalwards of the fish (Bianco et al., 2011; Romano et al., 2015). Intriguingly, the RF centres of the small-size selective tectal neurons are much denser in the nasal upper visual field, in agreement with the 'striking zone' of the larval hunting behaviour (Zimmermann et al., 2018). In spite of that, larval zebrafish initiate the hunting behaviour towards a prey with a size of smaller than 5 visual degrees (Bianco et al., 2011), which is much smaller than the visual stimulus (30° x 13°, azimuth x elevation) used in this study though the visual angle size of the prey perceived by the animal retinae increases as the animal approaches the prey. Plus, our visual stimulus was horizontally moving gratings instead of a moving dot. The absence of tectal neurons with RF centres in the temporal lower visual field is most likely not due to the physical structure of the setup itself, though the setup (metal holder) of the experiment might block part of the temporal visual field of the animals.

Consistent with the anatomical projections of the retinal ganglion cells (Baier et al., 1996; Trowe et al., 1996), small-size RF tectal neurons are aligned in a topographic pattern as reported previously (Bergmann et al., 2018; Niell and Smith, 2005). In this study, the monocular visual field is represented by a topographic map comprised of small-size RF tectal neurons as revealed with precise measurement.

Pretectal neurons have large-size RFs and bias to the ventral visual field

Neurons in the pretectal region (more prominent in the caudal region) often show large-size RFs, occasionally even covering the whole monocular visual field. These large-size RF neurons selectively responded to large moving gratings, but ignoring the small-size local motion. The pretectal region correspond likely to the pretectal anterior medial cluster (AMC) reported before based on the anatomical location. This AMC was considered to process optic flow and involved in the OKR (Kubo et al., 2014). Notably, the RF centres of these neurons tend to be located in the lower visual field, which resembles the pretectal RFs from the dogfish (Masseck and Hoffmann, 2008). Large-size RFs are considered as excellent detectors to perceive the optic flow and potentially mediate visuomotor transformation (Krapp et al., 1998; Simpson et al., 1988a). Regarding the bias of the pretectal RF centre towards the lower visual field, these zebrafish pretectal neurons likely sample visual inputs from the river bed below the animals.

Three rotational/translational axes are represented by the tectal and pretectal binocular neurons

Fish pretectum is functionally similar to the tetrapod AOS and is involved in OKR and OMR behaviour (Kubo et al., 2014; Masseck and Hoffmann, 2008, 2009b; Naumann et al., 2016). Some of the zebrafish pretectal neurons were shown previously to selectively respond to binocular rotational or translational motion in the horizontal plane (Kubo et al., 2014). In this study, neurons exclusively responsive to the rotational or translational binocular motion around/along three Cartesian coordinate axes have been identified (translational motion along left-right axis was analysed from the data kindly offered by Prof. Florian Engert (Naumann et al., 2016)), though the number of the neurons is relatively low. These binocular selective neurons resemble the binocular cells in the tetrapod AOS. However, the preferred rotational axes or preferred translational orientations in the horizontal plane are about 45°

apart from the anterior-posterior axis on either side of the midsagittal plane in previous reports (Masseck and Hoffmann, 2009b; Simpson et al., 1988b; Wylie et al., 1998). Our experimental protocol didn't include motion along/around these two axes, since only a few neurons selective to these axes were identified in our pilot experiments. The pitch and roll axes are possibly not the optimal axes of these binocular neurons. A new experimental protocol with more binocular visual stimulus combinations is needed to identify the optimal translational/rotational axes of these neurons.

The binocular motion encoding of these neurons is highly specific regarding the large number of possible binocular motion combinations in our current protocol. Particularly, the rotational and translational motion selective neurons are potentially able to code and differentiate rotational and translational optic flow and instruct the behavioural choice of the animals directly.

The optomotor response is driven strongest by motion in the lower-temporal visual field

Zebrafish OMR behaviour can be stably elicited with large-size forward binocular motion projected from below or both sides of the animals (Severi et al., 2014; Thiele et al., 2014). The behavior consists of symmetrical tail undulation and locomotion following the large-size forward motion (Ahrens et al., 2013a). For the free-swimming larvae, the tail-beat frequency is positively correlated with the velocity of the stimulus (Severi et al., 2014). In our experiment, the larval zebrafish were head-fixed embedded in low melting agarose. Symmetrical tail beats, typically higher than 25 Hz, were successfully induced with our forward translational motion protocol, but the intended locomotion of the animals is actually unknown. Furthermore, we confirmed that free-swimming larvae showed OMR behavior following the motion with the same setup and whole-field motion protocol, which strongly indicates that the head-fixed larvae were performing virtual OMR swimming. Regarding

head-fixed larvae, it has been reported that the tail-beat frequency often contained a maximum around 30 Hz, even induced by fast grating speeds. The lowest maximal tail-beat frequency centred around 25 Hz (Severi et al., 2014). We used 25 Hz as a threshold to detect OMR tail beats in our study while no frequency threshold was applied in the previous report (Severi et al., 2014). Some OMR tail beats might be filtered out in our results compared to the those from Severi et al.. But the differences in setups and protocols should be taken into consideration as well.

In our recordings, visually inspected zebrafish struggle behavior is rather rare. Only one fish struggled severely and the dataset was not included for the OMR behavior analysis. Therefore, strict thresholds of the tail-beat frequency and amplitude for the OMR behavior are not critical for the data analysis. Nevertheless, the amplitude of the tail undulation is dramatically smaller than that of the struggle behavior, in which the tail often bends until close to the fish head in a 'C'-shape, in our study.

Here we show that the forward motion in the lower-temporal visual field, even as small as $45^\circ \times 20^\circ$ (azimuth \times elevation), was able to induce larval OMR behaviour. Thus, unexpectedly, whole-field forward translational motion is not necessary for the larval OMR. But the exact size and location of the OMR behaviour 'receptive field' cannot be precisely measured with our experimental protocol. A more flexible setup, presenting visual stimulus in various sizes and locations, is ideal to overcome this limitation. In comparison, visual stimulus in the upper nasal visual field, mainly corresponding to the RF centres of the small-size RF tectal neurons, is insufficient to elicit OMR swim. Since zebrafish preferably live in shallow water or streams (Engeszer et al., 2007), in the OMR visuomotor system, the visual information is most likely gathered from the lower-temporal visual field, in this case, the river bed with high visual contrast below the animals instead of the sky above the visual field equator.

The lower-temporal visual field, the 'hotspot' to induce OMR behavior, coincides largely with the RF centres of large-size RF pretectal neurons. Given the involvement of the zebrafish pretectum in the OMR behavior, though causative experiments are still missing, these large-

size RF pretectal neurons are potentially the upstream sensory neurons and mediate the OMR behavior in the visuomotor pathway. Optogenetic manipulation has been widely applied in zebrafish (Kubo et al., 2014; Schoonheim et al., 2010), but transgenic fish lines with caudal pretectal neurons labelled are still needed for further tests of the OMR neural pathway.

Limitation of the experiments

Reflections in the experimental setup

In our *in vivo* calcium imaging experiment, the animals were embedded on a triangular stage located in the centre of a glass bulb when the visual stimulus was presented from the right side. Since the optic nerves totally cross the chiasm and project to the contralateral side of the eyes, only a few ipsilateral responsive neurons were expected in our experiment. However, reflection of the monocular visual stimulus to the other side (left side in our case) of the animals was noticed and so were many responsive neurons on the ipsilateral side of the visual stimulus (Figure 11A).

According to the Fresnel Equations, the intensity of final reflected light reaching the unstimulated eye was about 4% of that of the grating's light emitted from the cylindrical arena (only the main light refraction and reflection towards the animal were taken into account, Figure 11B-E). The reflection is visible to the fish for two main reasons. First of all, when the incidence angle of the visual stimulus is small, the reflected light can be shed into the opposite eye (left eye) due to the large size of the fish eyes (Figure 11A). In this case, the reflected light intensity is low (less than 4%, Figure 11D, E). Second, the reflected light can reach the fish eyes directly when the incidence angle of the visual stimulus is large since the glass bulb is not totally spherical and the fish eyes are not exactly located in the glass bulb centre. We should note that with a large incidence angle using an ideal spherical glass bulb

and perfect alignment of the fish, the fish could not see the reflected light according to the Snell's law (Figure 11B, C).

The reflection was weak, but strong enough to evoke neural activities in the fish brain. In the new experiments of 14 animals, the left eyes of the animals were covered with a piece of black foil. As expected, most of the neural activities in the ipsilateral tectum disappeared.

In the monocular direction selectivity analysis and RF mapping experiments, the old and new datasets were merged together. But the ipsilateral tectal neurons were excluded in the analysis for the old data (without covering the left eye). Parts of the ipsilateral pretectal neurons are likely activated by the reflection in our old dataset, though binocular pretectal neurons are frequent on both hemispheres of the zebrafish brain (Kubo et al., 2014).

The binocular direction selectivity analysis experiment is also influenced by the reflection in spite of the weak light of the reflection. The original protocol contained 63 (8x8-1) visual stimulus phases, including 14 (2x7) phases with one eye (unstimulated eye) presented with a totally dark half arena. The reflection of the visual stimulus to the unstimulated eye made the result from these 14 phases very complex. Therefore, the data of these 14 phases were excluded in the final analysis. In comparison, the reflected light was much weaker when both of the two half arenas presented contrast rich visual stimulus. The influences of the reflection in the other 49 (8x8-1-2x7) stimulus phases are negligible.

Coating the glass bulb with anti-reflective materials, such as silicon nanotips and random GaN nanopillars, from inside is likely a good option to reduce the reflection of the glass surface for our experiment (Raut et al., 2011). But this coating method is quite expensive and might lead to other physical optical problems. Alternatively, casting visual stimulus patterns using a back-projected stimulus system to a screen outside of a frosted glass bulb provides stimulation with minimised reflection (Fuller et al., 2014) .

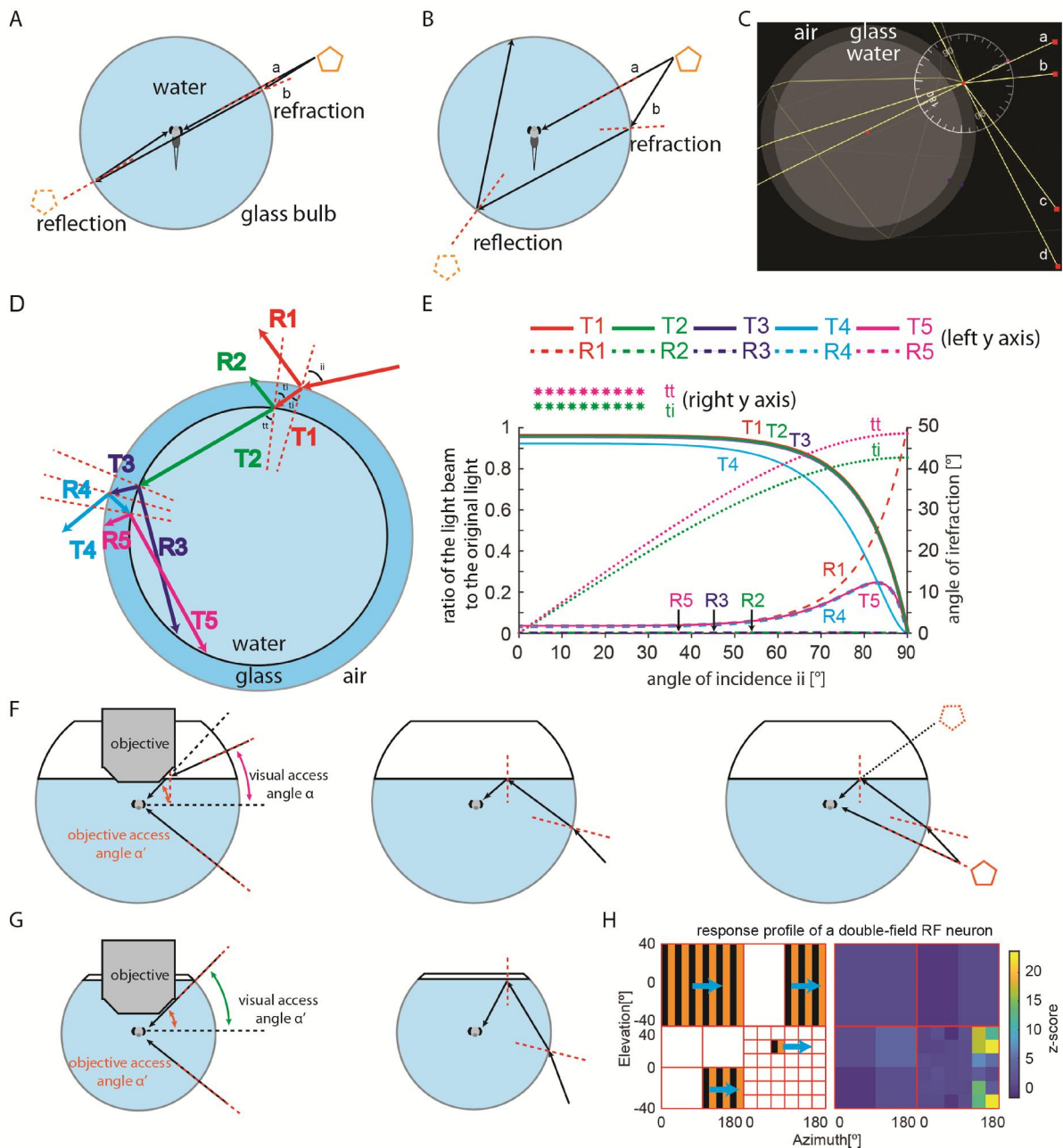


Figure 11. A schematic of the light refraction and reflection in the glass bulb. (A) Light beam a is perpendicular to the air-glass-water interface and reaches the right eye of the fish directly without refraction. The light beam is absorbed by the fish right eye and no reflection occurs on the opposite side (relative to the fish) of the light source. Due to the refraction and reflection of the air-glass-water interface, light beam b is reflected back to the left eye of the fish when the incidence angle of light beam b is almost (but not) perpendicular to the glass surface (as will be the case for many photons emitted by our cylindrical stimulus arena, not depicted). The black circle with cyan shade represents a glass bulb filled with water. The pentagon and the dashed pentagon are corresponding to the visual stimulus and its reflection. Red dashed lines, normal planes. To simplify discussion, only two media (air and water) are considered in panels (A), (B), (F) and (G), although in reality three media (air, glass, water) are present (see panels (D) and (E)). **(B)** Light beam b is reflected back but cannot reach fish eye when the incidence angle of light beam b is large. **(C)** Four light beams (a, b, c and d) are

shed into the glass bulb with different angles of incidence simulated with software (Ray Optics Simulation). The indices of refraction from water (inner circle) and glass (outer ring) are 1.333 and 1.47. The reflected light reaches the unstimulated eye of the fish (left eye) only when the incidence angle of the visual stimulus is small (e.g., beam a). **(D)** The light pathway of reflection and refraction with the air-glass-water interface taken into consideration. The outer cyan ring represents the glass bulb and the lighter cyan inside corresponds to the water. T, transmitted light; R, reflected light. The angles of incidence and refraction are labelled with letters i_i , t_i (an angle of incidence or refraction conditionally), and t_t . R3 and T5 can reach the unstimulated eye when the incidence angle i_i of the original light beam is small. **(E)** Ratios of reflected and retransmitted light to the original light intensity and angles of refraction incidence calculated according to the Fresnel equation and Snell's law. The colours correspond to the colours and light beams in panel (D). T5 is about 14 times stronger than R3 when the incidence angle i_i is smaller than 30° . To show the overlapping curves, some of the curves are plotted with a wider stroke. **(F)** Light pathways in a big glass bulb with low water level. Left panel, due to short working distance of the objective and the shape of the objective tip, the maximal under water access angle (upper view field) of light beams equals to the objective access angle α' . Because of the low water level and the refraction of the light on the air-water surface, the visual access angle α from above (visual space in elevation in the upper view field) is smaller compared to high water level in panel (G); middle panel, a light beam from below the fish is reflected downwards. As a result, the visual stimulus reflection is accessible to the animal from above; right panel, one stimulus (a pentagon) is shown to the animal from below. Due to the reflection, the image of the objective is accessible to the animal from both below (direct image) and above (reflection). **(G)** Light pathways in a small glass bulb with high water level. Left panel, due to the high water level, the visual access α' angle from above, which equals to the objective access angle α' , is larger compared to low water level in panel (F); right panel, light from below the fish is reflected downwards and shown from above of the animal. However, the angle of incidence is too large and it is not available with our LED arena. **(H)** A diagram of parts of the RF mapping protocol and the response profile of one double-field receptive field neuron recorded under the condition shown on the right side of panel (F). Red dashed lines are the *normal* for the refraction or reflection. The magenta and green arcs show the visual access angles α and α' of the light for the animals. The orange arcs represent the objective access angle α' .

Limited whole view field

The half cylindrical arena covered about $165^\circ \times 80^\circ$ (azimuth x elevation), but still less than the monocular visual field of a single eye (Pita et al., 2015). The parts of the visual fields close to the upper or lower poles are not studied in our experiments. That also explains why the RF centres of many small-size RF pretectal neurons are located on the edge of the arena from our data. It is likely that those RF centres are actually located in the region even closer to either pole.

Because of that, a new spherical arena with a larger coverage was developed in our lab to overcome this caveat, though the region higher than 40° in elevation above the fish head is still blocked by the objective for calcium imaging experiments (Figure 12).

Apart from the reflection mentioned above, more complex reflection light pathways existed when a large-size glass bulb and the 25 x Nikon objective were used for the recordings (Figure 11F). The Nikon objective is not water-proof, and because of that, the glass bulb was not allowed to fill up with E3 water. Instead, the water surface was only about 1 cm above the fish head. Under this experimental condition, many apparent double RFs with two RF centres were found in the fish brain (Figure 11H). But these double RFs are most likely an artefact caused by our setup for the following two reasons. 1) In most cases, the two RF centres are vertically aligned in the upper and lower visual field respectively. 2) This type of RFs almost disappeared after using a small glass bulb filled up with E3 water and a water-proof Zeiss objective (Figure 11G).

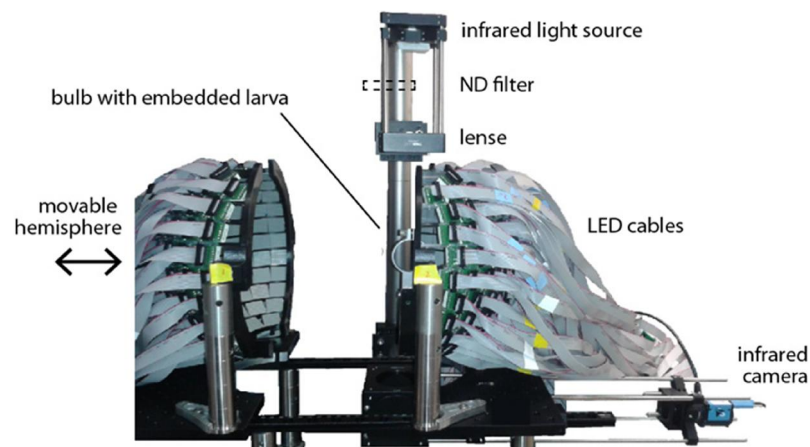


Figure 12. Image of the two hemispheres and the imaging setup. The two halves of the arenas cover almost the whole visual field of the zebrafish (Dehmelt et al., 2019). The arrows indicate the movable directions.

Drifting of the fish along z axis during calcium imaging recordings

During the *in vivo* calcium imaging, especially when the visual stimulus protocol lasted a long time (e.g., 40 minutes), image drift in the horizontal plane and along the z axis was noticed.

For shifting in the horizontal plane, the image time series were registered with TurboReg (EPFL) in imageJ. Regarding the image shift along the z axis, three methods were tried to eliminate the influences. 1) Shifting the objective controlled with a custom-written script in data acquisition software Mscan to counteract the image drifting during the recordings. However, the shifting direction and velocity are unpredictable and the imaged frames are not available to calculate the drifting length during the recording with our imaging software (new version software of Mscan allows for online access of acquired data). 2) Taking a z stack recording from 5 μm below to 5 μm above the target plane with an increment of 0.5 μm . During the recordings, on-line images were captured from the computer monitor and localized to the z stack above based on the optimal correlation with NI LabView. Then the objective was manually shifted to the initial z level. Due to the changes of the fluorescence during the recordings, the localization with NI LabView failed frequently. The method was discarded in the end. 3) Taking a z stack recording from 100 μm above the landmark to 60 μm below the landmark (posterior commissure). The images were visually localized to the z stack and then the objective was manually shifted to the initial z level. On average the objective shifting along the z axis is smaller than 5 μm during a 35 minutes' recording and the last method worked well in our case, though the experimenter has to check the shift visually frequently. Among the three methods above, the first one is potentially applicable, the second one was discarded and we only used the last one in the data acquisition.

Generally the z shift was faster at the beginning of the experiment, and then the velocity decreased dramatically. The z shift is larger when the animals were paralyzed with α -bungarotoxin. It is possible that the z shift was contributed from the gravity of the low melting agarose surrounded the fish or the paralysis of muscles. But the reason for the z shift is still unclear.

RFs were mapped only with horizontally moving gratings monocularly

In the RF mapping experiment, only horizontally moving stimuli were presented to the right eye with a half-cylindrical arena. Thus neurons with more complex, e.g. rotational, binocular, or vertical optic flow fields could not be detected in this study (Kubo et al., 2014; Wang et al., 2019). These types of complex RF structures exist in visual neurons of other species (Karmeier et al., 2003; Krapp et al., 2001) and future studies are needed to identify them in zebrafish. A new RF estimation method, which is based on contiguous motion noise stimuli and allows for rapid RF mapping of global motion sensitive neurons with calcium imaging method, has been reported (Zhang and Arrenberg, 2019).

The topographic map of the zebrafish optic tectum has been shown both anatomically and functionally before (Bergmann et al., 2018; Niell and Smith, 2005; Trowe et al., 1996). In this study, the topographic pattern was measure with higher resolution. Since the direction selective neurons with different preferred directions are intermingled in the tectum, vertical motion-sensitive neurons most likely show the same alignment as well, though the topographic pattern was only measured from the horizontal motion-sensitive neurons.

Limitation of the visual stimulus size in the RF mapping experiment

Our RF mapping protocol contained 57 different motion phases. Square wave gratings, 0.033 cycles per degree, covered a view field of $168^\circ \times 80^\circ$ (azimuth x elevation) monocularly. In each phase, a patch of moving gratings was presented to the animal, varying its size and location among the motion phases (Figure 13A, B). Since the smallest visual motion stimulus in the RF mapping experiment covered $30^\circ \times 13^\circ$ (azimuth x elevation), tectal neurons with even smaller RFs were unidentifiable and the precise location and size of the RFs are not available with our protocol. Theoretically, the accuracy could be higher when measured with smaller visual stimulus. But in our case, the large decay time constant of the calcium

indicator GCaMP5G, 1.5 s, made our experimental protocol quite long, lasting around 40 minutes per recording, which introduces other uncontrollable effects (e.g., animal shifting along the z axis during the recordings). In compromise, 6 x 6 patches were used as the smallest visual stimulus and 57 phases of moving gratings in 7 different sizes were included in our protocol.

Another caveat resulting from the protocol is the calculation of the RF size and location. Here, an assumption that the response of each neuron is linear across the RF is made and the response in each of the 57 phases was weighted according to the sizes of the visual stimuli. However, high temporal resolution recordings with patch clamp showed that the responses within regions of a RF are not linear (Zhang et al., 2011).

In addition, response curve of GCaMP5G shows strong non-linearity due to the cooperative calcium-binding sites of the calcium indicator. The Hill coefficients of GCaMP5 range from 2.5 to 4. Therefore, the inference of calcium transients from fluorescence data is highly affected. Only in the 'linear' regime of a calcium indicator, below its K_d value, is quantification with the commonly used calibration methods possible since the fluorescence intensity change $\Delta F/F$ of the indicator is roughly proportional to the cellular calcium concentration (Rose et al., 2014). In our study, owing to the non-linearity of the GCaMP5G, it is impossible to accurately infer the firing frequencies of a single neuron stimulated with different visual stimulus patterns and estimate the precise RF size and location.

Last, most of the medium-size RF neurons responded to the 2 x 2 patch visual stimulus which is assigned a weigh factor of 4. But we didn't present visual stimulus with the same size located in the centre of the monocular visual field. Consequently, the RF centre calculation of the medium-size RFs is biased toward the periphery regions of the visual field. The RF mapping could be improved with high temporal resolution recordings, such as voltage-sensitive dye Di-4-ANEPPDHQ or using fluorescent voltage reporter Archon1 (Follmann et al., 2018; Piatkevich et al., 2018), combining with homogeneously distributed smaller visual stimulus units.

Two-dimensional Gaussian fitting of receptive fields

Based on the responses of the neurons in the 6 x 6 phases (Figure 13A, B), the RFs of the neurons were tried to be fitted with a 2-D Gaussian model with Matlab. Using different seeds (beta values), we managed to fit most small-size RFs with this model (Figure 13E, F). Since large-size RF neurons show very weak or no activities to small-size visual stimulus, the fitting model is not applicable to this response type (Figure 13C, D). Apart from that, there are three major caveats in our case. 1) The original dataset for the fitting only contain 36 data points, which is rather small for the fitting of the 180° x 80° (azimuth x elevation) whole visual field. 2) When the strongest responsive patch is on the edge or in the corner of the 6 * 6 patches, the fitted RF centre is biased towards the centre of the whole visual field (Figure 13G, H). 3) It is difficult to figure out an applicable method to calculate the size of the RFs for all the response types. Consequently, the Gaussian fitting method was not used in our published data analysis.

In the first RF mapping dataset recorded from 10 animals, RFs with two spatially separated RF centres were also identified. This type of RFs was fitted with two 2-D Gaussian model and the corresponding cells were named as double receptive field neurons (Figure 11H). However, it turned out that this RF type resulted from the reflection of visual stimulus from the water-air interface (Figure 11F; see discussion in the reflection section).

Nevertheless, the Gaussian fitting method was finally substituted with a linear overlay method (see the method in the paper).

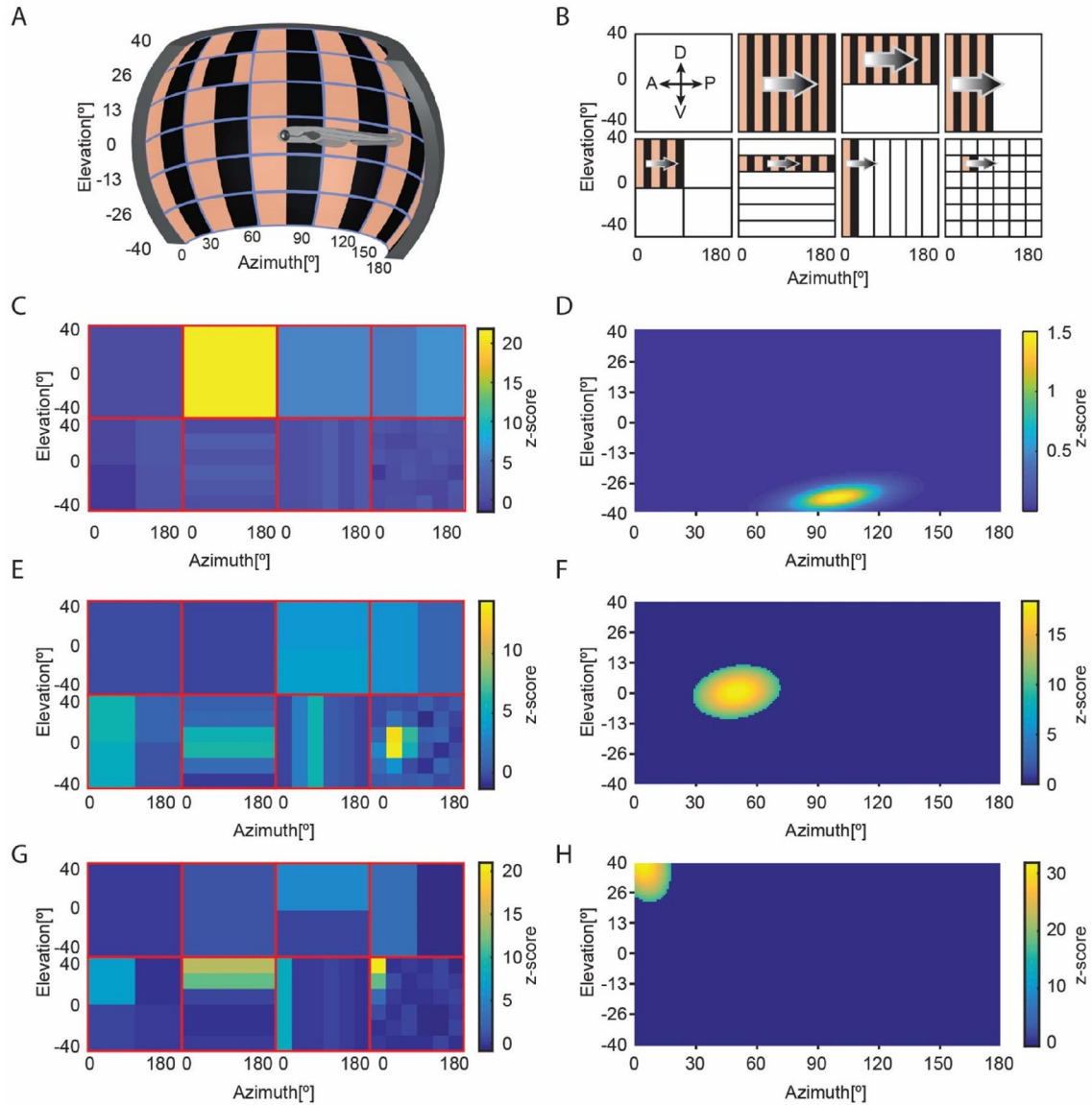


Figure 13. A simple 2D Gaussian model of RFs does not work for all neurons and was abandoned. (A) An illustration of the setup for RF mapping experiment. Vertical moving gratings with different sizes (1x1, 2x1, 1x2, 2x2, 6x1, 1x6 and 6x6 patches, in panel (B)) and locations were presented to the right eye of the fish by a half cylindrical LED light area while fish was mounted in the centre of the arena. This plot shows a frame from one motion phase corresponding to one of the 6x6 patches. For the illustration purpose, the view field covered by the cylindrical half arena is plotted here instead of the real half arena. (B) A diagram of the monocular RF mapping protocol in our study. In each motion phase (in total 57 phases), vertical moving gratings covering one of the patches (1x1, 2x1, 1x2, 2x2, 6x1, 1x6 and 6x6) were presented to the larva monocularly in three repetitions. 8 out of 10 fish were stimulated with temporalwards motion (indicated with arrows), the other 2 fish stimulated with nasalwards motion. The blank areas in this diagram were covered with stationary vertical gratings during the experiments. The first square in the first row represents the stationary visual stimulus during the pauses of the protocol. A, anterior; P, posterior, D, dorsal, V, ventral. (C) The z-score heat map of

the responses from a large-size RF pretectal neuron. The 8 squares, corresponding to panel (B), represent the medium responses of the neurons from three repetitions in the 57 motion phases (plus the average response of all the stationary phases). This neuron responded exclusively to the whole field motion (the 1x1 patch). (D) The 2-D Gaussian model fitted RF from the 6x6 patched of the neuron in panel (C). Since the data fitting was performed with the calcium signals in the 6x6 patched which the neuron didn't respond to, a small-size RF with RF centre in the lower visual field was fitted in the fitting result and this can't represent the real RF. (E) The z-score heat map of the responses from a small-size RF tectal neuron. The neurons responded strongest to either of the two 6x6 patches. The neural activity decreased when the size or the location of the visual stimulus changed. (F) The 2-D Gaussian model fitted RF from the neuron in panel (E). The fitted RF matches the response profile (locations and size) of the neuron. (G) The z-score heat map of the responses from a small-size RF tectal neuron. The neurons responded strongest to one of the 6x6 patches in the left upper corner. The neural activity decreased when the size or the location of the visual stimulus changed. (H) The 2-D Gaussian model fitted RF from the neuron in panel (G). The fitted RF, on the whole, matches the response profile (locations and size) of the neuron. But it is difficult to estimate the RF size since the potential RF outside of the visual field covered by our setup is unknown.

Indirect measurement of the inhibitory RFs

Inhibitory RFs are very common in zebrafish tectal neurons and they are reported to mainly overlap with the excitatory RFs from the same neurons (Zhang et al., 2011). Due to the limitation of the GCaMP5G calcium indicator, the inhibitory RFs cannot be measured directly. Instead, the inhibitory effects were only calculated via subtraction of the responses evoked with visual stimuli of different sizes.

A series of inverse-response Ca^{2+} indicators, which showed increased fluorescence responding to the reduced intracellular calcium concentration, have been developed and applied in fruit fly recently (Zhao et al., 2018). These new indicators may enable us to visualize the inhibitory RFs directly in zebrafish brain in the future.

Limitations of the binocular DS data

Pitch rotational selective neurons were also identified in the zebrafish tectum and pretectum. These neurons are likely specifically activated by the optic flow to maintain body balance when the animals turn their heads up or down. Nevertheless, we are still not sure whether these neurons are selectively tuned to pitch motion due to the lack of the knowledge of their RF sizes and locations. For instance, the neurons identified here may have small direction selective RFs and they were merely not activated by other types of whole field motion in our protocol. Further experiments testing with motion covering different visual field areas and in different directions are needed to confirm the pitch rotational selectivity.

In the main data analysis steps, only the responses in 25 stimulus phases were analysed. In these phases, responses were binarized with a certain threshold and thus each neuron was classified as either active or silent for a given stimulus phase. Therefore, 2^{25} binary response profiles were theoretically possible. This corresponds to a high-dimensional space, and actual neuronal responses only covered a fraction of the possible response types. To identify the visually evoked responses, certain arbitrary thresholds were applied to motion sensitive neurons. Though the final results are relatively stable when the threshold varies between 2.5 to 3.5 x standard deviation of the baseline, the response type classification method is still needed to optimize. Noticeably, some of the response types are extremely similar to each other except the difference of one stimulus phase out of 25.

Besides, binocular neurons selective to horizontal gratings motion presented to one eye and vertical motion to the other eye are also frequent, which is quite unexpected. These kinds of binocular motion combinations are not naturalistic. At least, these combinations cannot be generated via self-motion of the animals.

Correlation analysis was also applied for the binocular direction preference analysis experiment (data not shown), though the method was not adopted in the final analysis. The correlation analysis was adapted from a previous report (Kubo et al., 2014). Briefly, a series

of regressors were generated based on the amplitudes of the calcium events. Since only the calcium events during the grating motion phase and stronger than 3 x standard deviation of the baseline count, each regressor has maximally 49 (7 x 7) active phase in each repetition. Regression coefficients between the calcium trace and the regressors were calculated with Matlab. The optimal regressor was considered as the response type of the neuron. However, the main caveat of this method is that several best regressors frequently show quite similar regression coefficients for a single neuron. In addition, the response types calculated with this method often deviate dramatically from human judgement. Different methods were tried to improve the regression analysis, but finally the method was discarded. Instead, we used an arbitrary threshold, 3 x standard deviation, to detect each neurons' responsive phases to the motion. Then the response types of the neurons were defined based on these response phases above. This method is more robust and the result is consistent when the threshold varies in a small range. In addition, the result from this method is in agreement with human judgement.

Defining the brain region of pretectum

The adult zebrafish pretectum is comprised of several nuclei distributed from the superficial to the periventricular regions, receives numerous retinal and tectal afferents, and projects to the optic tectum as well (Fernald and Shelton, 1985; Kastnerhuber et al., 2010; Presson et al., 1985; Yanez et al., 2018). Though the visual function of the pretectum has been investigated in zebrafish previously (Kubo et al., 2014; Naumann et al., 2016; Wang et al., 2019), and various nuclei have been identified in the adult pretectum (Yanez et al., 2018), the anatomical structure of the larval pretectum is still not clear. Morphologically, the identity, extent, and overlap of larval pretectal neuron populations, which give rise to each of the known adult pretectal nuclei, is not easily discernible (Arrenberg and Driever, 2013; Kubo et al., 2014; Muto et al., 2017; Semmelhack et al., 2014).

In the fish line GCaMP5G used in this study, the boundaries between the pretectum and adjacent brain structures, especially the ventral and rostral boundaries, are mainly invisible. Pretectal dopaminergic neurons, which are evolutionarily conserved across most amniotes (Yamamoto and Vernier, 2011), indicate the location of the periventricular pretectal nucleus as landmark (Filippi et al., 2014). Unfortunately, no other fish lines that label specific pretectal regions in our imaging experiments were available.

Our preliminary data from another fish line, *Tg(elavl3:nls-GCaMP6s)mnp400* (Dal Maschio et al., 2017), in which the fluorescence signal is localized to the cellular nucleus, revealed several separated nuclei in the larval pretectal region (Figure 14). It is most likely that the anatomical and functional segregation of the pretectal nuclei have been established at this development stage, 5 dpf, in larval zebrafish. Functional pretectal clusters, like the AMC (Kubo et al., 2014), rostral small-size RF and caudal large-size RF neuron clusters can be localized to three different clusters in this new fish line though we have not confirmed the classification of the pretectal neurons in the *Tg(elavl3:nls-GCaMP6s)mnp400* fish line yet. Nevertheless, detailed anatomical annotation of the larval pretectum is needed to understand the functional and anatomical segregation of the pretectal neurons.

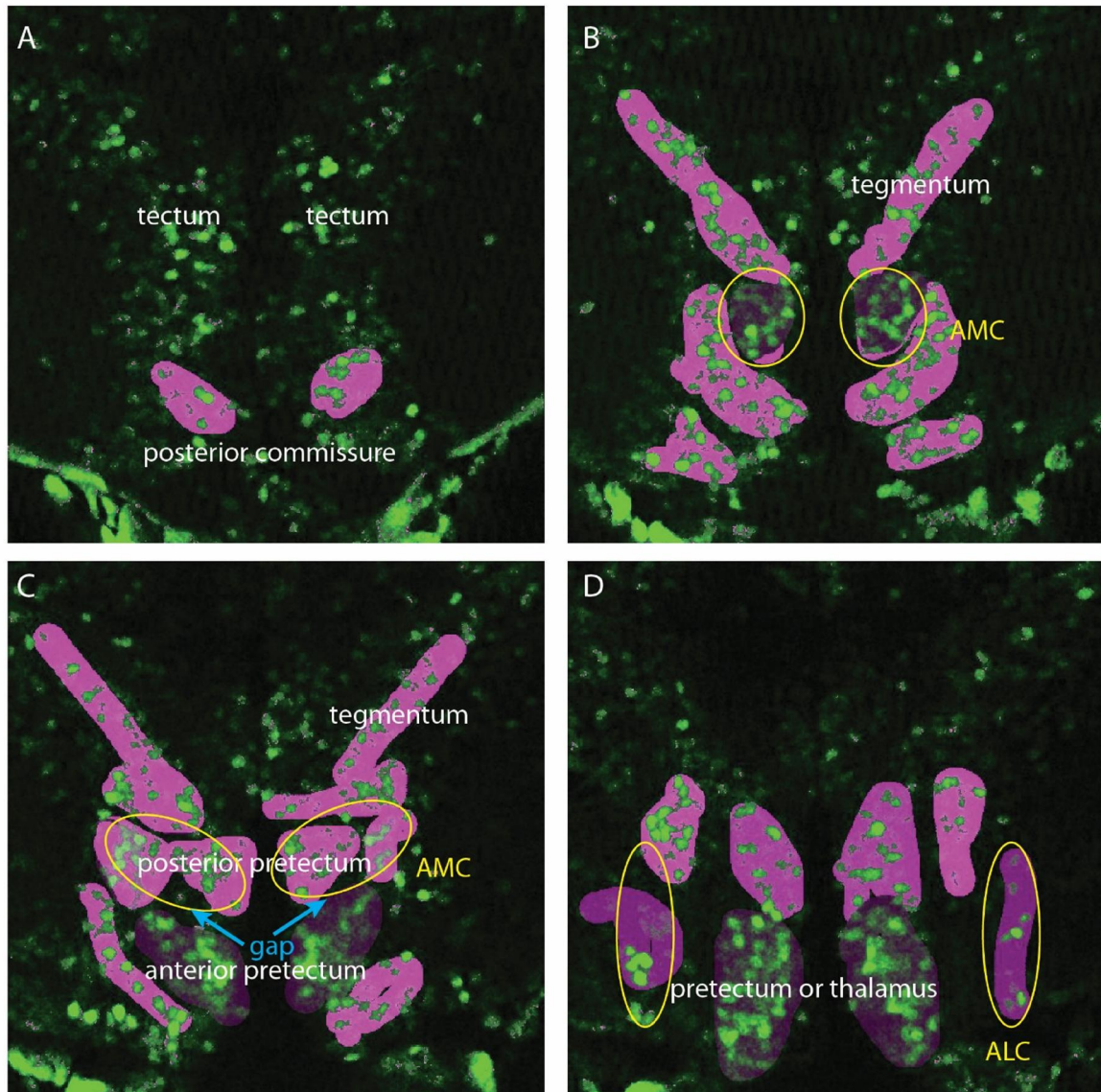


Figure 14. Manually defined larval zebrafish pretectal anatomic clusters (in magenta, the nuclei of the cells from *Tg(elavl3:nls-GCaMP6s)mnp400* are shown in green pseudo colour) with software Slicer 4.10.2. From (A) to (D), the locations of the image planes are aligned along the dorsal-ventral axis with an increment of 8.8 μm. (A) The landmark posterior commissure and tectal neurons. (B) The bar shape clusters in the posterior region are most likely in the tegmentum. The clusters highlighted in the yellow circles correspond to AMC. (C) An anatomical gap devoid of neurons is located between the anterior pretectum and posterior pretectum. (D) The bar shape clusters on both sides correspond to ALC. The other clusters are not clear. AMC, anterior medial cluster; ALC, anterior lateral cluster (Kubo et al., 2014).

Future directions

(1) Zebrafish tectal and pretectal neurons receive neural inputs from RGCs directly. However, the directional space of the tectum and pretectum is comprised of four PDs while RGCs only have three. The transformation of the PDs between the tectum/pretectum and RGCs is an interesting research topic. New genetically encoded calcium indicators (GECI) with different colours or sensitive to inhibitory inputs will be beneficial to solve this problem (Abbas et al., 2017; Marvin et al., 2019; Shen et al., 2018).

(2) The PDs of a single large-size RF neuron in different sub-regions within the RF are potentially different, matching the spatial pattern of optic flow during ego-motion. Although large-size RF pretectal neurons have been found in our study, the detailed PD construction of the RFs is still unknown. Faster calcium indicators or electrophysiological recordings are ideal to answer this question. Alternatively, a new rapid RF mapping method, which is based on contiguous motion noise stimuli and combined with calcium imaging method, can be applied (Zhang and Arrenberg, 2019).

(3) Only binocular motion along/around three axes was tested in this study. It is still unknown whether these axes are the preferred axes or not (Wylie et al., 1998).

(4) How the pretectal binocularity is accomplished remains peculiarly intriguing given that fish optic nerves cross the chiasm completely. We propose that these binocular neurons receive synaptic inputs from multiple monocular neurons and integrate the information. For example, a binocular forward motion selective neuron likely integrates excitatory inputs from one nasalward selective monocular neuron corresponding to one eye and inhibitory inputs from one temporalward selective monocular neuron corresponding to the other eye (Kubo et al., 2014; Manteuffel, 1987). If this hypothesis stands, an excitatory and an inhibitory receptive field are identifiable corresponding to either eye. Localizing these receptive fields for each binocular neuron is an interesting task. Furthermore, it would advance our understanding of

the mechanisms underlying binocular direction selectivity to label these binocular single neurons and investigate the functional properties encoded by their presynaptic neurons.

(5) The binocular neurons are thought to send outputs to the (pre-)motor neurons and instruct behaviour choice directly. Single cell labelling of these binocular neurons will enable us to trace the neural circuits and confirm the hypothesis with *in vivo* imaging.

List of papers/manuscripts

Wang, K.*, Hinz, J.*, Haikala, V., Reiff, D.F., and Arrenberg, A.B. (2019). Selective processing of all rotational and translational optic flow directions in the zebrafish pretectum and tectum. BMC Biol 17, 29.

Florian A. Dehmelt, Rebecca Meier, Julian Hinz, Takeshi Yoshimatsu, Clara A. Simacek, **Kun Wang**, Tom Baden, Aristides B. Arrenberg (2019). Spherical arena reveals optokinetic response tuning to stimulus location, size and frequency across entire visual field of larval zebrafish. (Biorxiv)

Wang, K., Hinz, J., Zhang, Y., Thiele, T.R., and Arrenberg, A.B. (2020). Parallel channels for motion feature extraction in the pretectum and tectum of larval zebrafish. Cell Rep 30(2):442-453.e6.

Kun Wang, Burkhard Arrenberg, Julian Hinz, and Aristides B Arrenberg. Design and visualization of experimental setups for vision research in small, aquatic animals (in preparation)

Statement of contributions

Manuscript 1: Selective processing of all rotational and translational optic flow directions in the zebrafish pretectum and tectum

Aristides B Arrenberg conceived the experiments and associated analysis protocols.

Kun Wang performed the experiments and analyzed the monocular direction selectivity.

KW and Julian Hinz analyzed the binocular direction selectivity.

Julian Hinz implemented the linear sum model analysis.

Florian Engert kindly offered their binocular experiment datasets which has been published before (Naumann et al., 2016).

Kun Wang and Aristides B Arrenberg analyzed the data provided by Florian Engert.

Väinö Haikala and Dierk F. Reiff helped to set up the LED arena experiments.

Kun Wang, Julian Hinz, and Aristides B Arrenberg wrote the manuscript.

All authors commented on the manuscript.

Manuscript 2: Parallel channels for motion feature extraction in the pretectum and tectum of larval zebrafish

Aristides B Arrenberg, Kun Wang, Julian Hinz and Tod R. Thiele conceived the experiments and associated analysis protocols.

Kun Wang built the optomotor response experimental setup and performed all the experiments.

Kun Wang, Julian Hinz and Zhang Yue analysed the data.

Kun Wang, Julian Hinz, and Aristides B Arrenberg wrote the manuscript, with inputs from Tod R. Thiele.

Christian Altbürger (from Driever's lab, University of Freiburg) established the Tg(th-E2A-QF2)m1512; Tg(QUAS:eGFP)c403; Tg(QUAS:mApple)c636 fish lines and recorded the anatomical z-stacks of a double-transgenic dopaminergic line.

Julianne Skinner contributed to the RF centre distribution analysis.

Martin Meyer (King's College London, UK) commented on a previous version of the manuscript.
Other contributors to the general work
Bastian Hablitzel wrote the original image registration Macro in ImageJ, MOM_Load and Midbrain_localizer in Matlab.
Christian Brysch updated the MOM_Load Matlab code before Kun Wang's further updates.
Thomas Nieß (glassblower shop, University of Tübingen) and Klaus Vollmer (fine mechanics workshop, University Clinic Tübingen) made the glass bulb, triangular stage and metal holder for the glass bulb.
Prudenter-Agas Arrenberg (Hamburg, Germany) generated 3-D illustrations of our setup.

Manuscript 1:		authors	Manuscript 1:		authors
Figure 1	Panel A-D, F-H	PAA	Figure S1	Panel D Other panels	KW PAA
Figure 2	Panel B	PAA	Figure S2	Panel D Other panels	KW PAA
Figure 3	Panel B	PAA	Figure S3	Panel A,C	PAA, KW
Figure 4	Panel A	PAA, KW	Figure S4	Panels	KW
			Figure S5	Panel A,C	PAA
All the other figure panels which are not mentioned above are finished by KW.					

Annotation of the contribution to the Figures in the papers and the manuscript.					
Paper 1:		authors	Paper 2:		authors
Figure 1	Panel A	ABA, PAA, KW	Figure 1	Panel A	ABA, PAA, KW

	Panel F	ABA		Panel D	JH, KW
Figure 2	Panel A Panel D, E Panel F, G, H	ABA, PAA, KW JH, KW ABA, KW	Figure 2	Panel A, B Panel D, E	JH, KW KW, ABA
Figure 3	Panel A Others	ABA, PAA KW, ABA	Figure 3	Panel C Panel D, E	JH, KW KW, ABA
Figure 4	Panels A, B	ABA, KW	Figure 4	Panel A Panel C, D, F, G and H	ABA, PAA, KW, JH JH, KW
Figure S1	Panel F, G, H	JH, KW	Figure 5		JH, KW, ABA
Figure S2		JH	Figure S1	Panel F	ABA, PAA
Figure S3		KW	Figure S2		JH, KW
Figure S4	Panel B, C, D	JH, KW	Figure S3		KW
Figure S5	Panel A Others	JH JH, KW	Figure S4		KW
Figure S6		KW	Figure S5		KW
Figure S7	Panel A, B, C	JH, KW	Figure S6		KW
Figure S8		JH, KW			
All the other figure panels which are not mentioned above are finished by KW.					

Acknowledgements

First of all, I would like to express my gratitude to my supervisor Junior-Prof. Dr. Aristides B Arrenberg for his suggestions, all the discussions and help during my PhD study. Especially, I thank him offering me the research position to pursue my PhD, which, in addition to my career, influences my whole life on multiple aspects. I treasure this opportunity as a new start point in life.

I would like to thank my advisory board members, Prof. Dr. Hanspeter A. Mallot and Dr. rer. nat. Timm Schubert for their advices and discussions. Following their professional suggestions, I refer to more literatures, courses and have a deeper and broader knowledge of optic flow research field.

I acknowledge the contribution of Julian Hinz for him help and discussions with the data analysis. He analysed data with me for almost three years and contributed a lot in writing the manuscripts. I can never forget the discussions and days when we worked together even on weekends and holidays.

I would like to express my appreciation to Dr. Väinö Haikala and Prof. Dr. Dierk F. Reiff for their kind help with the cylindrical LED arena visual stimulus presenting system. Dr. Väinö Haikala offered me many detailed suggestions, even including how to solder polarized capacitors.

Prof. Dr. Wolfgang Driever and Christian Altbürger kindly offered us new fish lines and I started my experiments in Driever's lab when our new lab in Tübingen was still under construction. My PhD project would have been delayed without Prof. Dr. Wolfgang Driever offering me working space. I am appreciating for their help.

I am grateful to my best friend and colleague Christian Brysch for his help both in scientific research and my new life in Germany. He helped me to start the basic data analysis with Matlab and imageJ and provides advices as well as discussions through all my PhD study.

He translates from basic food menu to official documents for me and helps me to accustom myself to new cultures.

My sincere thanks also go to Florian Dehmelt and Claire Leyden for establishing the new lab in Tübingen, Zhang Yue and Dr. Sebastian Reinig for the discussions on the data analysis, Tim Hladnik, Nina Omejc for their help in writing the application for animal experiment protocols.

Great thanks to Sabine Götter, Rebbeca Meier, Sabrina Fuchs, Timo Brüggemann, Maximilian Wandl for taking care of the fish, Adam von Daranyi and Susanne Werner-Hansen from the CIN IT.

I also show my appreciation to Thomas Nieß (the glassblower shop, University of Tübingen) and Klaus Vollmer (fine mechanics workshop, University Clinic Tübingen) for processing glass and metal devices for us.

I appreciate the financial support from the Forschungsgemeinschaft (DFG) grants and the Human Frontier Science Program (HFSP) Young Investigator Grant for my PhD project.

Furthermore, I would like to express my appreciation to my friends Martin Wilkens, Philip Obergfell, Fabian Lang, and Kyrlyo Schenstnyi.

Last, I would like to express my gratitude to my sister Xue Wang and my aunt Guiqin Pei for taking care of my parents. I am able to concentrate myself to my PhD study away from China.

Reference

- Abbas, F., Triplett, M.A., Goodhill, G.J., and Meyer, M.P. (2017). A Three-Layer Network Model of Direction Selective Circuits in the Optic Tectum. *Front Neural Circuits* 11, 88.
- Ahrens, M.B., Huang, K.H., Narayan, S., Mensh, B.D., and Engert, F. (2013a). Two-photon calcium imaging during fictive navigation in virtual environments. *Front Neural Circuits* 7, 104.
- Ahrens, M.B., Orger, M.B., Robson, D.N., Li, J.M., and Keller, P.J. (2013b). Whole-brain functional imaging at cellular resolution using light-sheet microscopy. *Nat Methods* 10, 413-420.
- Arnold, G.P. (1974). Rheotropism in fishes. *Biol Rev Camb Philos Soc* 49, 515-576.
- Arrenberg, A.B., and Driever, W. (2013). Integrating anatomy and function for zebrafish circuit analysis. *Front Neural Circuits* 7, 74.
- Baier, H., Klostermann, S., Trowe, T., Karlstrom, R.O., Nusslein-Volhard, C., and Bonhoeffer, F. (1996). Genetic dissection of the retinotectal projection. *Development* 123, 415-425.
- Baird, E., Kreiss, E., Wcislo, W., Warrant, E., and Dacke, M. (2011). Nocturnal insects use optic flow for flight control. *Biol Lett* 7, 499-501.
- Barclay, J.W., Morgan, A., and Burgoyne, R.D. (2005). Calcium-dependent regulation of exocytosis. *Cell calcium* 38, 343-353.
- Barlow, H.B., and Levick, W.R. (1965). The mechanism of directionally selective units in rabbit's retina. *J Physiol* 178, 477-504.
- Bergmann, K., Meza Santoscoy, P., Lygdas, K., Nikolaeva, Y., MacDonald, R.B., Cunliffe, V.T., and Nikolaev, A. (2018). Imaging Neuronal Activity in the Optic Tectum of Late Stage Larval Zebrafish. *J Dev Biol* 6.

- Besharse, J., and A. Brandon, R. (1973). Optomotor response and eye structure of the troglobitic salamander *gyrinophilus palleucus*, Vol 89.
- Bianco, I.H., Kampff, A.R., and Engert, F. (2011). Prey capture behavior evoked by simple visual stimuli in larval zebrafish. *Front Syst Neurosci* 5, 101.
- Borst, A., and Euler, T. (2011). Seeing things in motion: models, circuits, and mechanisms. *Neuron* 71, 974-994.
- Brockhoff, S.E. (2006). Measuring the optokinetic response of zebrafish larvae. *Nat Protoc* 1, 2448-2451.
- Burgess, H.A., Schoch, H., and Granato, M. (2010). Distinct retinal pathways drive spatial orientation behaviors in zebrafish navigation. *Curr Biol* 20, 381-386.
- Burrill, J.D., and Easter, S.S., Jr. (1994). Development of the retinofugal projections in the embryonic and larval zebrafish (*Brachydanio rerio*). *J Comp Neurol* 346, 583-600.
- Cabrera, S., and Theobald, J.C. (2013). Flying fruit flies correct for visual sideslip depending on relative speed of forward optic flow. *Front Behav Neurosci* 7, 76.
- Clement, G., and Magnin, M. (1984). Effects of accessory optic system lesions on vestibulo-ocular and optokinetic reflexes in the cat. *Exp Brain Res* 55, 49-59.
- Dal Maschio, M., Donovan, J.C., Helmbrecht, T.O., and Baier, H. (2017). Linking Neurons to Network Function and Behavior by Two-Photon Holographic Optogenetics and Volumetric Imaging. *Neuron* 94, 774-789 e775.
- Dehmelt, F.A., Meier, R., Hinz, J., Yoshimatsu, T., Simacek, C.A., Wang, K., Baden, T., and Arrenberg, A.B. (2019). Spherical arena reveals optokinetic response tuning to stimulus location, size and frequency across entire visual field of larval zebrafish. *bioRxiv*.

- Dehmelt, F.A., von Daranyi, A., Leyden, C., and Arrenberg, A.B. (2018). Evoking and tracking zebrafish eye movement in multiple larvae with ZebEyeTrack. *Nat Protoc* 13, 1539-1568.
- Dunn, T.W., Gebhardt, C., Naumann, E.A., Riegler, C., Ahrens, M.B., Engert, F., and Del Bene, F. (2016). Neural Circuits Underlying Visually Evoked Escapes in Larval Zebrafish. *Neuron* 89, 613-628.
- Eckmeier, D., and Bischof, H.J. (2008). The optokinetic response in wild type and white zebra finches. *J Comp Physiol A Neuroethol Sens Neural Behav Physiol* 194, 871-878.
- Engeszer, R.E., Patterson, L.B., Rao, A.A., and Parichy, D.M. (2007). Zebrafish in the wild: a review of natural history and new notes from the field. *Zebrafish* 4, 21-40.
- Fernald, R.D., and Shelton, L.C. (1985). The organization of the diencephalon and the pretectum in the cichlid fish, *Haplochromis burtoni*. *J Comp Neurol* 238, 202-217.
- Field, D.J., and Tolhurst, D.J. (1986). The structure and symmetry of simple-cell receptive-field profiles in the cat's visual cortex. *Proceedings of the Royal Society of London Series B, Biological sciences* 228, 379-400.
- Filippi, A., Mueller, T., and Driever, W. (2014). vglut2 and gad expression reveal distinct patterns of dual GABAergic versus glutamatergic cotransmitter phenotypes of dopaminergic and noradrenergic neurons in the zebrafish brain. *J Comp Neurol* 522, 2019-2037.
- Fleisch, V.C., and Neuhauss, S.C. (2006). Visual behavior in zebrafish. *Zebrafish* 3, 191-201.
- Follmann, R., Goldsmith, C.J., and Stein, W. (2018). Multimodal sensory information is represented by a combinatorial code in a sensorimotor system. *PLOS Biology* 16, e2004527.
- Fredericks, C.A., Giolli, R.A., Blanks, R.H., and Sadun, A.A. (1988). The human accessory optic system. *Brain Res* 454, 116-122.

Fuller, S.B., Straw, A.D., Peek, M.Y., Murray, R.M., and Dickinson, M.H. (2014). Flying *Drosophila* stabilize their vision-based velocity controller by sensing wind with their antennae. *Proc Natl Acad Sci U S A* *111*, E1182-1191.

Gahtan, E., Tanger, P., and Baier, H. (2005). Visual prey capture in larval zebrafish is controlled by identified reticulospinal neurons downstream of the tectum. *J Neurosci* *25*, 9294-9303.

Gibson, J.J. (1950). *The Perception of the Visual World*. Houghton Mifflin.

Giolli, R.A., Blanks, R.H., and Lui, F. (2006). The accessory optic system: basic organization with an update on connectivity, neurochemistry, and function. *Prog Brain Res* *151*, 407-440.

Grama, A., and Engert, F. (2012). Direction selectivity in the larval zebrafish tectum is mediated by asymmetric inhibition. *Front Neural Circuits* *6*, 59.

Grienberger, C., and Konnerth, A. (2012). Imaging calcium in neurons. *Neuron* *73*, 862-885.

Hafed, Z.M., and Chen, C.Y. (2016). Sharper, Stronger, Faster Upper Visual Field Representation in Primate Superior Colliculus. *Curr Biol* *26*, 1647-1658.

Haikala, V., Joesch, M., Borst, A., and Mauss, A.S. (2013). Optogenetic control of fly optomotor responses. *J Neurosci* *33*, 13927-13934.

Hamilton, D.B., Albrecht, D.G., and Geisler, W.S. (1989). Visual cortical receptive fields in monkey and cat: spatial and temporal phase transfer function. *Vision Res* *29*, 1285-1308.

Hirsch, J.A. (2003). Synaptic physiology and receptive field structure in the early visual pathway of the cat. *Cereb Cortex* *13*, 63-69.

Hoffmann, K.P., and Fischer, W.H. (2001). Directional effect of inactivation of the nucleus of the optic tract on optokinetic nystagmus in the cat. *Vision Res* *41*, 3389-3398.

Huang, Y.Y., and Neuhauss, S.C. (2008). The optokinetic response in zebrafish and its applications. *Front Biosci* *13*, 1899-1916.

- Hubel, D.H., and Wiesel, T.N. (1968). Receptive fields and functional architecture of monkey striate cortex. *J Physiol* 195, 215-243.
- Huber-Reggi, S.P., Mueller, K.P., and Neuhauss, S.C. (2013). Analysis of optokinetic response in zebrafish by computer-based eye tracking. *Methods Mol Biol* 935, 139-160.
- Hunter, P.R., Lowe, A.S., Thompson, I.D., and Meyer, M.P. (2013). Emergent properties of the optic tectum revealed by population analysis of direction and orientation selectivity. *J Neurosci* 33, 13940-13945.
- Irion, U., Krauss, J., and Nusslein-Volhard, C. (2014). Precise and efficient genome editing in zebrafish using the CRISPR/Cas9 system. *Development* 141, 4827-4830.
- Jiang, H., and Stephens, N.L. (1994). Calcium and smooth muscle contraction. *Molecular and cellular biochemistry* 135, 1-9.
- K. Hausen, and Wehrhahn, C. (1983). Microsurgical lesion of horizontal cells changes optomotor yaw responses in the blowfly *Calliphora erythrocephala*. *Proceedings of the Royal Society of London* 219, 211-216
- Karameier, K., Krapp, H.G., and Egelhaaf, M. (2003). Robustness of the tuning of fly visual interneurons to rotatory optic flow. *J Neurophysiol* 90, 1626-1634.
- Kastnerhuber, E., Kratochwil, C.F., Ryu, S., Schweitzer, J., and Driever, W. (2010). Genetic dissection of dopaminergic and noradrenergic contributions to catecholaminergic tracts in early larval zebrafish. *J Comp Neurol* 518, 439-458.
- Klar, M., and Hoffmann, K.P. (2002). Visual direction-selective neurons in the pretectum of the rainbow trout. *Brain Res Bull* 57, 431-433.
- Knapp, C.M., Proudlock, F.A., and Gottlob, I. (2013). OKN asymmetry in human subjects: a literature review. *Strabismus* 21, 37-49.
- Koenderink, J.J., and van Doorn, A.J. (1987). Facts on optic flow. *Biol Cybern* 56, 247-254.

- Krapp, H.G., Hengstenberg, B., and Hengstenberg, R. (1998). Dendritic structure and receptive-field organization of optic flow processing interneurons in the fly. *J Neurophysiol* 79, 1902-1917.
- Krapp, H.G., Hengstenberg, R., and Egelhaaf, M. (2001). Binocular contributions to optic flow processing in the fly visual system. *J Neurophysiol* 85, 724-734.
- Krauss, A., and Neumeier, C. (2003). Wavelength dependence of the optomotor response in zebrafish (*Danio rerio*). *Vision Res* 43, 1273-1282.
- Kretschmer, F., Tariq, M., Chatila, W., Wu, B., and Badea, T.C. (2017). Comparison of optomotor and optokinetic reflexes in mice. *J Neurophysiol* 118, 300-316.
- Kubo, F., Hablitzel, B., Dal Maschio, M., Driever, W., Baier, H., and Arrenberg, A.B. (2014). Functional architecture of an optic flow-responsive area that drives horizontal eye movements in zebrafish. *Neuron* 81, 1344-1359.
- Kyoung, M., Zhang, Y., Diao, J., Chu, S., and Brunger, A.T. (2013). Studying calcium-triggered vesicle fusion in a single vesicle-vesicle content and lipid-mixing system. *Nat Protoc* 8, 1-16.
- Lappe, M., Pökel, M., and Hoffmann, K.P. (1998). Optokinetic eye movements elicited by radial optic flow in the macaque monkey. *J Neurophysiol* 79, 1461-1480.
- Lazar, G. (1972). Role of the accessory optic system in the optokinetic nystagmus of the frog. *Brain Behav Evol* 5, 443-460.
- Lister, J.A., Robertson, C.P., Lepage, T., Johnson, S.L., and Raible, D.W. (1999). *nacre* encodes a zebrafish microphthalmia-related protein that regulates neural-crest-derived pigment cell fate. *Development* 126, 3757-3767.

- Lowe, A.S., Nikolaou, N., Hunter, P.R., Thompson, I.D., and Meyer, M.P. (2013). A systems-based dissection of retinal inputs to the zebrafish tectum reveals different rules for different functional classes during development. *J Neurosci* 33, 13946-13956.
- M. Heisenberg, R. Wonneberger, and Wolf, R. (1978). Optomotor-blind H31 - a *Drosophila* mutant of the lobula plate giant neurons. *Journal of comparative physiology* 124, 287–296.
- Ma, A.C., Chen, Y., Blackburn, P.R., and Ekker, S.C. (2016). TALEN-Mediated Mutagenesis and Genome Editing. *Methods Mol Biol* 1451, 17-30.
- Maaswinkel, H., and Li, L. (2003). Spatio-temporal frequency characteristics of the optomotor response in zebrafish. *Vision Res* 43, 21-30.
- Manteuffel, G. (1984). Electrophysiology and anatomy of direction-specific pretectal units in *Salamandra salamandra*. *Exp Brain Res* 54, 415-425.
- Manteuffel, G. (1987). Binocular afferents to the salamander pretectum mediate rotation sensitivity of cells selective for visual background motions. *Brain Res* 422, 381-383.
- Marvin, J.S., Shimoda, Y., Magloire, V., Leite, M., Kawashima, T., Jensen, T.P., Kolb, I., Knott, E.L., Novak, O., Podgorski, K., *et al.* (2019). A genetically encoded fluorescent sensor for in vivo imaging of GABA. *Nat Methods* 16, 763-770.
- Masseck, O.A., Forster, S., and Hoffmann, K.P. (2010). Sensitivity of the goldfish motion detection system revealed by incoherent random dot stimuli: comparison of behavioural and neuronal data. *PLoS One* 5, e9461.
- Masseck, O.A., and Hoffmann, K.P. (2008). Responses to moving visual stimuli in pretectal neurons of the small-spotted dogfish (*Scyliorhinus canicula*). *J Neurophysiol* 99, 200-207.
- Masseck, O.A., and Hoffmann, K.P. (2009a). Comparative neurobiology of the optokinetic reflex. *Ann N Y Acad Sci* 1164, 430-439.

Masseck, O.A., and Hoffmann, K.P. (2009b). Question of reference frames: visual direction-selective neurons in the accessory optic system of goldfish. *J Neurophysiol* 102, 2781-2789.

Mateeff, S., Yakimoff, N., Hohnsbein, J., Ehrenstein, W.H., Bohdanecky, Z., and Radil, T. (1991). Selective directional sensitivity in visual motion perception. *Vision Res* 31, 131-138.

Matsuo, V., and Cohen, B. (1984). Vertical optokinetic nystagmus and vestibular nystagmus in the monkey: up-down asymmetry and effects of gravity. *Exp Brain Res* 53, 197-216.

McClenahan, P., Troup, M., and Scott, E.K. (2012). Fin-tail coordination during escape and predatory behavior in larval zebrafish. *PLoS One* 7, e32295.

McKenna, O.C., and Wallman, J. (1985). Accessory optic system and pretectum of birds: comparisons with those of other vertebrates. *Brain Behav Evol* 26, 91-116.

Miles, F.A., and Busetini, C. (1992). Ocular compensation for self-motion. Visual mechanisms. *Ann N Y Acad Sci* 656, 220-232.

Mueller, K.P., and Neuhauss, S.C. (2010). Quantitative measurements of the optokinetic response in adult fish. *J Neurosci Methods* 186, 29-34.

Muto, A., and Kawakami, K. (2011). Imaging functional neural circuits in zebrafish with a new GCaMP and the Gal4FF-UAS system. *Commun Integr Biol* 4, 566-568.

Muto, A., and Kawakami, K. (2013). Prey capture in zebrafish larvae serves as a model to study cognitive functions. *Front Neural Circuits* 7, 110.

Muto, A., Lal, P., Ailani, D., Abe, G., Itoh, M., and Kawakami, K. (2017). Activation of the hypothalamic feeding centre upon visual prey detection. *Nat Commun* 8, 15029.

Muto, A., Ohkura, M., Kotani, T., Higashijima, S., Nakai, J., and Kawakami, K. (2011). Genetic visualization with an improved GCaMP calcium indicator reveals spatiotemporal activation of the spinal motor neurons in zebrafish. *Proc Natl Acad Sci U S A* 108, 5425-5430.

- Muto, A., Orger, M.B., Wehman, A.M., Smear, M.C., Kay, J.N., Page-McCaw, P.S., Gahtan, E., Xiao, T., Nevin, L.M., Gosse, N.J., *et al.* (2005). Forward genetic analysis of visual behavior in zebrafish. *PLoS Genet* *1*, e66.
- Najafian, M., Alerasool, N., and Moshtaghian, J. (2014). The effect of motion aftereffect on optomotor response in larva and adult zebrafish. *Neurosci Lett* *559*, 179-183.
- Nakai, J., Ohkura, M., and Imoto, K. (2001). A high signal-to-noise Ca(2+) probe composed of a single green fluorescent protein. *Nat Biotechnol* *19*, 137-141.
- Naumann, E.A., Fitzgerald, J.E., Dunn, T.W., Rihel, J., Sompolinsky, H., and Engert, F. (2016). From Whole-Brain Data to Functional Circuit Models: The Zebrafish Optomotor Response. *Cell* *167*, 947-960 e920.
- Niell, C.M., and Smith, S.J. (2005). Functional imaging reveals rapid development of visual response properties in the zebrafish tectum. *Neuron* *45*, 941-951.
- Orger, M.B., and Baier, H. (2005). Channeling of red and green cone inputs to the zebrafish optomotor response. *Vis Neurosci* *22*, 275-281.
- Oyster, C.W., and Barlow, H.B. (1967). Direction-selective units in rabbit retina: distribution of preferred directions. *Science* *155*, 841-842.
- Oyster, C.W., Simpson, J.I., Takahashi, E.S., and Soodak, R.E. (1980). Retinal ganglion cells projecting to the rabbit accessory optic system. *J Comp Neurol* *190*, 49-61.
- Paredes, R.M., Etzler, J.C., Watts, L.T., Zheng, W., and Lechleiter, J.D. (2008). Chemical calcium indicators. *Methods* *46*, 143-151.
- Pasternak, T. (1986). The role of cortical directional selectivity in detection of motion and flicker. *Vision Res* *26*, 1187-1194.

- Pflugfelder, G.O., and Heisenberg, M. (1995). Optomotor-blind of *Drosophila melanogaster*: a neurogenetic approach to optic lobe development and optomotor behaviour. *Comparative biochemistry and physiology Part A, Physiology* 110, 185-202.
- Piatkevich, K.D., Jung, E.E., Straub, C., Linghu, C., Park, D., Suk, H.J., Hochbaum, D.R., Goodwin, D., Pnevmatikakis, E., Pak, N., *et al.* (2018). A robotic multidimensional directed evolution approach applied to fluorescent voltage reporters. *Nature chemical biology* 14, 352-360.
- Pita, D., Moore, B.A., Tyrrell, L.P., and Fernandez-Juricic, E. (2015). Vision in two cyprinid fish: implications for collective behavior. *PeerJ* 3, e1113.
- Presson, J., Fernald, R.D., and Max, M. (1985). The organization of retinal projections to the diencephalon and pretectum in the cichlid fish, *Haplochromis burtoni*. *J Comp Neurol* 235, 360-374.
- Preuss, S.J., Trivedi, C.A., vom Berg-Maurer, C.M., Ryu, S., and Bollmann, J.H. (2014). Classification of object size in retinotectal microcircuits. *Curr Biol* 24, 2376-2385.
- Raut, H.K., Ganesh, V.A., Nair, A.S., and Ramakrishna, S. (2011). Anti-reflective coatings: A critical, in-depth review. *Energy & Environmental Science* 4, 3779.
- Ringach, D.L. (2004). Mapping receptive fields in primary visual cortex. *J Physiol* 558, 717-728.
- Ringach, D.L., Hawken, M.J., and Shapley, R. (2002). Receptive field structure of neurons in monkey primary visual cortex revealed by stimulation with natural image sequences. *J Vis* 2, 12-24.
- Rinner, O., Rick, J.M., and Neuhauss, S.C. (2005). Contrast sensitivity, spatial and temporal tuning of the larval zebrafish optokinetic response. *Invest Ophthalmol Vis Sci* 46, 137-142.

Robles, E., Laurell, E., and Baier, H. (2014). The retinal projectome reveals brain-area-specific visual representations generated by ganglion cell diversity. *Curr Biol* 24, 2085-2096.

Romano, S.A., Pietri, T., Perez-Schuster, V., Jouary, A., Haudrechy, M., and Sumbre, G. (2015). Spontaneous neuronal network dynamics reveal circuit's functional adaptations for behavior. *Neuron* 85, 1070-1085.

Rose, T., Goltstein, P.M., Portugues, R., and Griesbeck, O. (2014). Putting a finishing touch on GECIs. *Frontiers in molecular neuroscience* 7, 88.

Rosen, L.B., Ginty, D.D., Weber, M.J., and Greenberg, M.E. (1994). Membrane depolarization and calcium influx stimulate MEK and MAP kinase via activation of Ras. *Neuron* 12, 1207-1221.

Sajovic, P., and Levinthal, C. (1982). Visual cells of zebrafish optic tectum: mapping with small spots. *Neuroscience* 7, 2407-2426.

Sajovic, P., and Levinthal, C. (1983). Inhibitory mechanism in zebrafish optic tectum: visual response properties of tectal cells altered by picrotoxin and bicuculline. *Brain Res* 271, 227-240.

Schaerer, S., and Neumeier, C. (1996). Motion detection in goldfish investigated with the optomotor response is "color blind". *Vision Res* 36, 4025-4034.

Schnell, B., Joesch, M., Forstner, F., Raghu, S.V., Otsuna, H., Ito, K., Borst, A., and Reiff, D.F. (2010). Processing of horizontal optic flow in three visual interneurons of the *Drosophila* brain. *J Neurophysiol* 103, 1646-1657.

Schoonheim, P.J., Arrenberg, A.B., Del Bene, F., and Baier, H. (2010). Optogenetic localization and genetic perturbation of saccade-generating neurons in zebrafish. *J Neurosci* 30, 7111-7120.

- Scott, E.K., and Baier, H. (2009). The cellular architecture of the larval zebrafish tectum, as revealed by gal4 enhancer trap lines. *Front Neural Circuits* 3, 13.
- Semmelhack, J.L., Donovan, J.C., Thiele, T.R., Kuehn, E., Laurell, E., and Baier, H. (2014). A dedicated visual pathway for prey detection in larval zebrafish. *Elife* 3.
- Serres, J.R., and Ruffier, F. (2017). Optic flow-based collision-free strategies: From insects to robots. *Arthropod structure & development* 46, 703-717.
- Severi, K.E., Portugues, R., Marques, J.C., O'Malley, D.M., Orger, M.B., and Engert, F. (2014). Neural control and modulation of swimming speed in the larval zebrafish. *Neuron* 83, 692-707.
- Shen, Y., Dana, H., Abdelfattah, A.S., Patel, R., Shea, J., Molina, R.S., Rawal, B., Rancic, V., Chang, Y.F., Wu, L., *et al.* (2018). A genetically encoded Ca(2+) indicator based on circularly permuted sea anemone red fluorescent protein eqFP578. *BMC Biol* 16, 9.
- Simpson, J.I. (1984). The accessory optic system. *Annu Rev Neurosci* 7, 13-41.
- Simpson, J.I., Leonard, C.S., and Soodak, R.E. (1988a). The accessory optic system of rabbit. II. Spatial organization of direction selectivity. *J Neurophysiol* 60, 2055-2072.
- Simpson, J.I., Leonard, C.S., and Soodak, R.E. (1988b). The accessory optic system. Analyzer of self-motion. *Ann N Y Acad Sci* 545, 170-179.
- Spillmann, L. (2014). Receptive fields of visual neurons: the early years. *Perception* 43, 1145-1176.
- Springer AD, Easter SS Jr, and BW, A. (1977). The role of the optic tectum in various visually mediated behaviors of goldfish. *Brain Res* 128(3), 393-404.
- Stosiek, C., Garaschuk, O., Holthoff, K., and Konnerth, A. (2003). In vivo two-photon calcium imaging of neuronal networks. *Proc Natl Acad Sci U S A* 100, 7319-7324.

- Tauber, E.S., and Atkin, A. (1968). Optomotor responses to monocular stimulation: relation to visual system organization. *Science* 160, 1365-1367.
- Tauber, E.S., and Koffler, S. (1966). Optomotor response in human infants to apparent motion: evidence of innateness. *Science* 152, 382-383.
- Theobald, J.C., Ringach, D.L., and Frye, M.A. (2010). Dynamics of optomotor responses in *Drosophila* to perturbations in optic flow. *J Exp Biol* 213, 1366-1375.
- Thiele, T.R., Donovan, J.C., and Baier, H. (2014). Descending control of swim posture by a midbrain nucleus in zebrafish. *Neuron* 83, 679-691.
- Tian, L., Hires, S.A., and Looger, L.L. (2012). Imaging neuronal activity with genetically encoded calcium indicators. *Cold Spring Harb Protoc* 2012, 647-656.
- Tischbirek, C., Birkner, A., Jia, H., Sakmann, B., and Konnerth, A. (2015). Deep two-photon brain imaging with a red-shifted fluorometric Ca²⁺ indicator. *Proc Natl Acad Sci U S A* 112, 11377-11382.
- Trowe, T., Klostermann, S., Baier, H., Granato, M., Crawford, A.D., Grunewald, B., Hoffmann, H., Karlstrom, R.O., Meyer, S.U., Muller, B., *et al.* (1996). Mutations disrupting the ordering and topographic mapping of axons in the retinotectal projection of the zebrafish, *Danio rerio*. *Development* 123, 439-450.
- Wang, K., Hinz, J., Haikala, V., Reiff, D.F., and Arrenberg, A.B. (2019). Selective processing of all rotational and translational optic flow directions in the zebrafish pretectum and tectum. *BMC Biol* 17, 29.
- Wylie, D.R. (2000). Binocular neurons in the nucleus lentiformis mesencephali in pigeons: responses to translational and rotational optic flowfields. *Neurosci Lett* 291, 9-12.
- Wylie, D.R., Bischof, W.F., and Frost, B.J. (1998). Common reference frame for neural coding of translational and rotational optic flow. *Nature* 392, 278-282.

Wylie, D.R., and Frost, B.J. (1996). The pigeon optokinetic system: visual input in extraocular muscle coordinates. *Vis Neurosci* 13, 945-953.

Xiao, Q., and Frost, B.J. (2009). Looming responses of telencephalic neurons in the pigeon are modulated by optic flow. *Brain Res* 1305, 40-46.

Xiao, T., Roeser, T., Staub, W., and Baier, H. (2005). A GFP-based genetic screen reveals mutations that disrupt the architecture of the zebrafish retinotectal projection. *Development* 132, 2955-2967.

Yamamoto, K., and Vernier, P. (2011). The evolution of dopamine systems in chordates. *Front Neuroanat* 5, 21.

Yanez, J., Suarez, T., Quelle, A., Folgueira, M., and Anadon, R. (2018). Neural connections of the pretectum in zebrafish (*Danio rerio*). *J Comp Neurol*.

Zhang, M., Liu, Y., Wang, S.Z., Zhong, W., Liu, B.H., and Tao, H.W. (2011). Functional elimination of excitatory feedforward inputs underlies developmental refinement of visual receptive fields in zebrafish. *J Neurosci* 31, 5460-5469.

Zhang, Y., and Arrenberg, A.B. (2019). High throughput, rapid receptive field estimation for global motion sensitive neurons using a contiguous motion noise stimulus. *J Neurosci Methods* 326, 108366.

Zhao, Y., Bushey, D., Zhao, Y., Schreier, E.R., Harrison, D.J., Wong, A.M., and Campbell, R.E. (2018). Inverse-response Ca(2+) indicators for optogenetic visualization of neuronal inhibition. *Sci Rep* 8, 11758.

Zimmermann, M.J.Y., Nevala, N.E., Yoshimatsu, T., Osorio, D., Nilsson, D.E., Berens, P., and Baden, T. (2018). Zebrafish Differentially Process Color across Visual Space to Match Natural Scenes. *Curr Biol* 28, 2018-2032 e2015.

Appendix:

Abbreviation:

AF 9	Arborisation field 9
ALC	Anterior lateral cluster
AMC	Anterior medial cluster
AOS	Accessory optic system
AVC	Anterior ventral cluster
DA	Dopaminergic
dpf	Day post fertilization
DS	Direction selective
DTN	Dorsal terminal nucleus
GECI	Genetically encoded calcium indicators
INL	Inner nuclear layer
IPL	Inner plexiform layer
LM	Pretectal nucleus lentiformis mesencephalic
LTN	Lateral terminal nucleus
MTN	Medial terminal nucleus
nBOR	Tegmental nucleus of the basal optic root
NOT	Pretectal nucleus of the optic tract
NT	Nasotemporal
OFF-RGCs	OFF-retinal ganglion cells
OKR	Optokinetic response
OMR	Optomotor response
ON-RGCs	ON-retinal ganglion cells
OPL	Outer plexiform layer
OT	Optic tectum
PA	Preferred axis
PD	Preferred direction
PT	Pretectum
RF	Receptive field
SAC	Starburst amacrine cell
SC	Superior colliculus
SPV	Stratum periventriculare
TN	Temporalnasal

Appended mathematical equations:

<p>Two-dimensional Gaussian function</p>	$a = \frac{(\cos^2 \theta)}{2(\sigma_x)^2} + \frac{(\sin^2 \theta)}{2(\sigma_y)^2}$ $b = -\frac{(\sin 2\theta)}{4(\sigma_x)^2} + \frac{(\sin 2\theta)}{4(\sigma_y)^2}$ $c = \frac{(\sin^2 \theta)}{2(\sigma_x)^2} + \frac{(\cos^2 \theta)}{2(\sigma_y)^2}$ $f(x, y) = -A \exp(a(x - x_0)^2 + 2b(x - x_0)(y - y_0) + c(y - y_0)^2)$
<p>One-peak Von Mises distribution for direction selective neuron</p> <p>Two-peak Von Mises distribution for orientation selective neuron</p>	$f(x \mu, \kappa) = a \frac{e^{(\kappa \cos(x - \mu))}}{(2\pi I_0(\kappa))} + b$ $f(x \mu, \kappa_1, \kappa_2) = a \frac{e^{(\kappa_1 \cos(x - \mu))}}{(2\pi I_0(\kappa_1))} + b \frac{e^{(\kappa_2 \cos(x - \mu - \pi))}}{(2\pi I_0(\kappa_2))} + c$
<p>Snell's law</p>	$\frac{(\sin \theta_2)}{(\sin \theta_1)} = \frac{n_1}{n_2}$
<p>Fresnel equations</p> <p>Transmitted light</p>	$t_s = \frac{(2n_1 \cos \theta_i)}{(n_1 \cos \theta_i + n_2 \cos \theta_t)}$ $T = \left \frac{(n_2 \cos \theta_t)}{(n_1 \cos \theta_i)} t \right ^2$
<p>Fresnel equations</p> <p>Reflected light</p>	$r_s = \frac{(n_1 \cos \theta_i - n_2 \cos \theta_t)}{(n_1 \cos \theta_i + n_2 \cos \theta_t)}$ $R = r ^2$

Appended papers/manuscripts:

**Design and visualization of experimental setups for vision research in
small, aquatic animals**

Kun Wang^{1,2}, Burkhard Arrenberg, Julian Hinz^{1,2,3}, and Aristides B Arrenberg^{1*}

¹ Werner Reichardt Centre for Integrative Neuroscience, Institute for Neurobiology, University of Tübingen, D-72108 Tübingen, Germany

² Graduate Training Centre for Neuroscience, University of Tübingen, D-72076 Tübingen, Germany

³ Current address: Friedrich Miescher Institute for Biomedical Research, 4058 Basel, Switzerland

* Correspondence should be addressed to A.B.A (aristides.arrenberg@uni-tuebingen.de)

Abstract

Vision research with laboratory animals requires high quality visual stimuli in the 3D visual space of the animal eyes. Due to the large binocular visual fields and the aquatic lifestyle, however, stimulus quality control is oftentimes challenging in the case of small-size fish. Here, we design a spherical glass bulb, coupled with a mechanical metal holder which allows for translational and rotational position adjustment in 3D Cartesian space, as a fish tank for visual experiments. Stimulus distortions resulting from light refraction, reflection and dispersion are effectively minimized in the glass bulb simulated with Blender. Neural direction selectivity and receptive field mapping analysis of zebrafish tectal neurons using calcium imaging method also confirm the optical advantages of the glass bulb, though minor optical disturbances still exist. Potential solutions and further suggestions for improvement are discussed.

Keywords

light reflection, refraction, dispersion, meniscus, receptive fields, optic tectum, zebrafish, glass bulb

Introduction

In visual neuroscience research with model organisms, an important standard protocol is that visual stimuli are presented to the animals, and behaviours and/or neuronal activities are recorded simultaneously while the animals are immobilized (Portugues et al., 2014, Ahrens et al., 2012, Ahmadiou et al., 2018, Boulanger-Weill et al., 2017, Bianco and Engert, 2015). The visual system extracts visual features from stimulus patterns, and neurons underlying the visual information encoding are sensitive and oftentimes selective to contrast, direction, spatial frequency, sizes, locations and shapes of the visual stimulus (Niell and Smith, 2005, Wang et al., 2020, Rust et al., 2005, Preuss et al., 2014, Abbas et al., 2017, Bianco and Engert, 2015). Therefore, presenting high quality visual stimulus patterns to the animal eyes is crucial for the investigation of the visual functions and neural encoding (Dunn and Fitzgerald, 2019).

A conventional platform, equipped with a standard-size monitor or a small LCD screen, is suitable for neural direction selectivity and receptive field (RF) mapping analysis of non-mammalian vertebrate optic tectum (Niell and Smith, 2005, Sajovic and Levinthal, 1982) since the RFs of tectal neurons are generally small (Sajovic and Levinthal, 1982, Bergmann et al., 2018, Zhang et al., 2011) and visual stimulus parameters, such as contrast and spatial frequency, are easy to control with programmable hardware and software (Rinner et al., 2005, Reiser and Dickinson, 2008).

Due to the size selectivity of large-size visual RF neurons, in contrast, the stimulus delivery system needs to cover a large or even the whole visual field of the animal eyes and the platform supporting experiment animals should allow for a large accessible view field for animals (Masseck and Hoffmann, 2009, Simpson et al., 1988, Wylie et al., 1998).

Furthermore, research using aquatic model animals (e.g. fish) gives rise to additional problems since a water environment is required during the experiments (Masseck and Hoffmann, 2009, Damjanovic et al., 2009). Visual stimuli to the animal eyes, presented from

air to water, are blurred and distorted via the air-container-water interface, resulting from geometrical optics (Dunn and Fitzgerald, 2019, Schuster et al., 2004). Thus, the motion consistency and entirety are disrupted. Alternatively, the stimulus delivery system and the camera can be set underwater, surrounding the experimental animal. However, the waterproof protection for the electronic setup is usually highly costly.

Here, we make use of Snell's law that disruptive optical effects are quite low when light beams pass through an optical interface orthogonally, and design a new spherical glass bulb container, coupled with an angle and location adjustable holder to optimize large visual field experiments with small-size fish. Moreover, we prove the optical advantages of the new glass bulb with optical simulation and functional neural activity recordings.

Results

Design and optical advantages of the new glass bulb container

The new glass bulb container is 8 centimetres (cm) in diameter, with an opening of 2 cm (in diameter) on the top, which allows for *in vivo* imaging experiment with an objective from above (Figure 1D, Supplementary Figure S1C). During the experiment, the animal was immobilized on the tip of a triangular stage located in the centre of the spherical glass bulb (Supplementary Figure S1D). In comparison to the common containers, such as Petri dish lids (e.g. 35 mm in diameter) and a cylindrical container (Figure 1B, C and Supplementary Figure S1A, B), the spherical glass bulb allows for larger homogeneous accessible visual space (Figure 1F-H). In addition, using a metal holder (Figure 1D, Supplementary Figure S1C), the animal's position is adjustable along and around the three axes of the Cartesian space.

Ideally, from the perspective of the animals, visual stimulus is presented homogeneously from outside into the location of the animal (Figure 1A). But due to the optical material interfaces between the fish eyes and the visual stimulus system, geometrical optics (Figure 1E) likely deteriorates of the optical quality of the experiment. Here, three containers (Figure 1B-D) are compared regarding geometrical optics and the coverage range of the visual stimulus via Blender simulation.

Light transmission

Light absorption remains under 2% due to the small sizes of the containers and, therefore, is negligible for our analysis. A high transparency of the water container is necessary for the precise visibility of the stimulus to the fish. Edges or thickenings of a container (e.g., at the vent edges and the outer reinforcement ring of the petri dish lid or the glued faces of the acrylic cylinder tank, Figure 1B, Supplementary Figure S1A) increase opacity and should be avoided in the design of containers.

Light refraction and reflection (including total internal reflection (TIR))

In these three containers, the stimulus patterns are only slightly disturbed by the general light refraction and reflection (TIR not included here) due to the geometry of the tank together with the material properties (Figure 1F-H). Only in the glass bulb, the reflected light from one side of the animal to the other side is visually detectable. But the reflected light is much weaker compared to the original visual stimulus (Figures 1H and 3B). In comparison, the TIR in the small Petri dish and the cylindrical container disrupts the consistency of the visual stimulus when light beams come from below with certain incidence angles (Figure 1F, G). Because of the TIR, light beams bounce many times in the Petri dish material (also in the cylindrical container, but fewer times than in the Petri dish, Supplementary Figure S2). Each beam splits into several rays at different locations, blurring the stimulus from the perspective of the fish (Figure 1F, G). For the small Petri dish, the visual stimulus is superimposed by multiple TIR from -41.4° to 41.4° in elevation (Figure 1F), which can severely disrupt the perception of vertical motion presented to the animals (Figure 4A). In the cylindrical container, the TIR mainly influences the visual stimulus in the range from 25° to 41.4° in elevation and the stimulus pattern in this visual field is reflected from below the equator of the view field without blurring. In addition, the view field of -40° to -50° in elevation is also disrupted by refraction and reflection (including TIR, Figure 1G). However, the glass bulb is not influenced by the TIR in our experimental condition (Figure 1H).

Dispersion of light

Light dispersion is restricted to non-orthogonal light beam passages through the water surface (Figure 1E). Therefore, it does not occur in the glass bulb since theoretically only orthogonal light beams reach the visual field of the stimulated animal eye via the bulb. For the Petri dish and cylindrical container, light disperses on the non-spherical polystyrene surfaces (Supplementary Figure 1E). Blur and rainbow edges by chromatic aberration are visible to the fish. Light dispersion is, however, very weak because of the narrow wavelength

band of coloured LED lights and does not dominate distortions and blurring in the Petri dish (Supplementary Figure S1G, H).

Meniscus

The meniscus on the surface of the water close to the edge of containers is modelled as well (Figure 1E and Supplementary Figure S1I). For the glass bulb, the meniscus only interrupts the upper view near 50° in elevation (Figure 1H and Supplementary Figure 1F). Particularly, the interruption does not exist in a glass bulb filled up with water when the opening rim is radially truncated (Supplementary Figure S1F). Nevertheless, due to the relatively small accessible elevation angles (40°) in the upper region restricted by the tip of the objective (Supplementary Figure S1J), the visual field of the fish in our glass bulb is not influenced by water meniscus. In the Petri dish and cylindrical container, the refraction and reflection are far more influential than the meniscus (Figure 1F, G).

Covering

The zebrafish has a large view field about 163° and the field of view is even broader with eye movements (Zimmermann et al., 2018). For each container in this study, its holder blocks parts of the stimulus (Figures 1F-H). Accordingly, a slim silhouette (contour/outline) of the holder is recommended. A large horizontal sector view of 180° to the rear of the fish from 0° to -90° in elevation is blocked by the holder of the Petri dish lid (Figure 1B, F). Due the camera and bracket mounted at the bottom of the cylindrical container, view field downwards from -60° is blocked as well (Figure 1B, G). The largest view field is access to the animals in the case of the glass bulb. Only a small region at the rear of the fish is missing, resulting from the metal holder well (Figure 1D, H).

In summary, the new glass bulb designed in this study offers a much larger coverage of the visual field and a better optical environment (no TIR, light dispersion or meniscus) to present visual stimuli to small aquatic animals than the other two containers (Figure 1F-H).

Water level influences geometrical optics of the glass bulb

TIR occurs in the glass bulb and influences the visual perception of the fish when the water level is low (Figure 2A). As a result, one part of the visual stimulus below the equator is reflected and shown upside down from above in the upper visual field of the animal, and the consistency of the visual stimuli near the equator along the elevation is disrupted (Figure 2B). In our first RF mapping experiment design, the glass bulb allows the filling up with water until 1 cm above the glass bulb centre due to its large size and the limited waterproof range of the objective tip (within 2 cm above from its tip).

Visual RFs of larval zebrafish tectal neurons were mapped with horizontally moving gratings with different sizes and locations (Figure 2C and Supplementary Figure S3C, D, see Method). Double-field RFs with two RF centres are frequently encountered under this low water level condition (Figure 2C, D). The two RF centres are vertically aligned for the majority of these RFs (Figure 2E). Therefore, this new RF type is most likely an artefact from the TIR of the light (Figure 2A, B).

Larval zebrafish tectal small-size RF centres cover nearly the whole monocular visual field and are biased to the upper nasal visual field (Supplementary Figure S3F, G) (Wang et al., 2020). In this hotspot region, however, only very few small-size tectal RFs centres are identified when the glass bulb is not filled up (Supplementary Figure S3E).

Reflection of the visual stimulus via the glass bulb

Theoretically, light beams of the visual stimulus are shed perpendicularly through the glass surface to the fish eye in the centre of the glass bulb and absorbed by the photoreceptor cells. Therefore, light reflection does not occur on the side of the un-stimulated fish eye (light beam a, Figure 3A). However, owing to light refraction, reflection and the large size of the fish eye, the reflected light can reach the un-stimulated eye when the incidence angle of the non-perpendicular light beams is small (light beam b, Figure 3A). Reflected visual stimulus

pattern is even visible on the contralateral side of the visual stimulus (Figure 3B), though the reflected light intensity is only about 4% of the original light (Figure 3C, D).

Here, the influences of the reflection to the unstimulated eye are tested with tectal RF mapping. In the control group, the unstimulated eye (left eye) was blocked by a black foil. The active tectal neurons are mainly on the contralateral side and the RF centres show topographical distribution along the anterior-posterior and dorso-ventral axes (Figure 3E, F and Supplementary Figure S4). In comparison, many tectal neurons, which show a reverse topographic map, are identified on the ipsilateral side when both eyes are exposed (Figure 3E, F and Supplementary Figure S4).

Total internal reflection and light refraction in the Petri dish lid resulted uncomplete detection of preferred directions in zebrafish tectal neurons

The inconsistency and disruption of the visual stimulus patterns in the Petri dish lid are mainly caused by TIR. As a result, the vertical motion of simple grating bars is seen as motion in opposite vertical directions on different elevation levels though horizontal motion is only slightly affected (Figure 4A).

Direction selectivity analysis of larval zebrafish tectal neurons was performed by presenting motion in eight different directions using a Petri dish lid (in this study) or a glass bulb as the container for the animal (Wang et al., 2019). Four preferred directions, which are represented by nearly the same amount of neurons, are shown from results recorded with the glass bulb. The four PDs are nearly perpendicular to each other, though the angle between the downward and temporalnasal PDs is smaller than 90° (Wang et al., 2019). As expected from the optical analysis (Figure 4A), almost no neurons represented the vertical PDs and only two horizontal PDs are detected. The two PDs point a little upward compared to the corresponding horizontal PDs recorded with the glass bulb. The nasaltemporal direction

(292°, 109 cells) is represented by many more neurons than the opposite temporalnasal direction (80°, 44 cells) (Figure 4B).

Discussion

Zebrafish are an important animal model for neuroscience and are widely used in vision guided behavioural and functional research (Wang et al., 2020, Bianco and Engert, 2015, Romano et al., 2015, Portugues et al., 2014). Here, we design a new glass bulb fish container providing improved optical properties for presenting the visual stimulus.

The glass bulb offers a better optical presentation of the visual stimulus than the other two containers

Petri dish lid

Visual stimuli seen in the Petri dish lid is severely disrupted across about 80° in elevation near the equator by the TIR (Figure 1F). The bounced light beams (Supplementary Figure S2) result in 1) Stimuli from different spatial locations projecting to the same region within the fish eye leads to stimuli overlapping and blurring. 2) Stimuli from adjacent spatial locations projecting to angular regions far away apart in the eye fish (e.g., 30°), leads to distortion of stimuli from the perspective of the animal. 3) Vertical motion in one direction is seen as motion in opposite vertical directions in different elevations (Figure 4A), which confuses the animals. Therefore, the Petri dish lid is not recommended for being used as a container for aquatic animal visual research, especially for experiments with presentation of the vertical motion or small-size stimuli in specific locations (RF mapping).

Cylindrical container

The cylindrical container offers a better optical environment than the Petri dish lid, though a relatively large view field is still disrupted by light refraction and reflection (Figure 1G). Overall, the cylindrical container should be designed to be as large as possible in the vertical direction (high on the top and deep at the bottom) to minimize the disturbance by its holder, water meniscus, light refraction and light reflection, in which case a highly waterproof objective is needed.

Glass bulb

From the perspective of the fish in the container, the distortion and blur of the visual stimulus are dramatically minimized in the glass bulb, though several potential problems still exist. 1) The visual stimulus is distorted, especially near the two poles, when the animal is not in the centre of the glass bulb (Supplementary Figure 5SA). 2) As the RF mapping experiment shows, the weak reflection of the visual stimuli is strong enough to activate ipsilateral tectal neurons. Optical coating is, however, not recommended in this case because of its negative optical effects, such as colour distortions and Newton rings. Blocking of the unstimulated eye is strongly recommended in monocular experiments with this glass bulb. 3) It is difficult to make the glass bulb ideally spherical and homogeneous. Thus, some potential geometrical optical problems may occur in reality.

Glass reflected light intensity is about 4% of the incoming light

The ratio of the reflected light to the incoming light increases, reaches the maximal value of 24.8% (angle of incidence, 83°) and reduces to 0 when the incidence angle increases from 0° to 90° (Figure 3C, D). However, the reflected light beam is far away from the glass bulb centre where the fish eyes are located when the ratio is high (e.g. light beam c in Supplementary Figure S5B). Only very small incidence angles allow for visible reflection to the unstimulated eye (e.g. light beam a in Supplementary Figure S5B). From 0° to 30° , the reflection rate of the original light is about 4% (Figure 3D). Regarding the light reflection from

the glass bulb, using frosted glass material is likely the best solution to reduce the reflection for our experiment, though the visual stimuli might be diffused (Raut et al., 2011).

Influences of geometrical optics on RF mapping and direction selectivity analysis

Many double-field RF neurons were found in larval zebrafish tectum when the water level in the glass bulb was low and these special RFs most likely resulted from the TIR of the visual stimulus. In this case, the RFs of these neurons are located in the upper visual field and relatively close to the equator. Therefore, the neurons responded to small-size motion located above the equator and the reflection of the small-size motion presented from below the equator of the view field, resulting in the artefacts of double-field RFs (Figure 2). But not all the small-size RF tectal neurons with RF centres above the equator responded to the reflection (Supplementary Figure S3E). The low intensity and low contrast of the stimulus reflection, resulting from the LED light emission angle and light refraction, likely contribute to the silence of these neurons to the reflection.

Similarly, much fewer ipsilateral small-size RF tectal neurons were identified than the contralateral counterpart. Furthermore, the small number also likely resulted from the opposite moving direction of the stimulus reflection in this case (Figure 3E, F and Supplementary Figure S4).

Only two out of the four PDs, which has been reported previously (Wang et al., 2019), were found from the zebrafish tectal space when a Petri dish lid was used for the experiment (Figure 4B). The incomplete detection of the PDs most likely resulted from the disruption of the vertical motion by the light refraction and TIR (Figure 4A). The horizontal PDs, different from those measured with the glass bulb, tend to the upward direction (Figure 4B), which cannot be contributed from the pitch angle during the embedding of the animals.

A limited accessible angle of upper visual field and potential stimulus reflection from the objective

For all three containers, the shape of the objective tip restricted the accessible angle of the upper view field (Supplementary Figure S1J). For example, the Zeiss W N-Acroplan (2.6 mm working distance, accessibility 41.6 °) offers accessibility that is 3° larger than that of Zeiss W-Apochromat (1.9 mm working distance, 38.39 ° accessibility). Thus, an objective with a long working distance and a large tip angle provides a larger upper view field for the animals.

Meanwhile, the material around and at the objective lens reflects the visual stimuli as well, though it is unlikely for the animals to see the reflection directly owing to the angle of the objective tip.

Caveats of the 3D modelling

Because of the limitation of our 3D modelling methods, possible physical optics effects, such as light interference between superposed waves and light polarization, on the experiment were not tested in detail. Nevertheless, these effects are usually very weak and not relevant for the experiments studied here.

Method

3D visualization techniques

All the 3D visualizations were performed with 3D computer graphics software Blender and LuxCoreRender. The rendered images are either shown in photorealistic representations to test the optical quality (e.g., Figure 1B-D) or symbolic representations for illustration (e.g., Supplementary Figure S1I). The perspective of rendered images (either from the researchers or the experimental animals), camera settings of the rendering and rendering composition are indicated in corresponding figure legends. In this study, geometrical optical effects resulted from light transmission (including turbidity, absorption, filtering (UV-light)), reflection (including TIR), refraction, dispersion and covering, were simulated and visualized.

Three different fish containers

Three types of fish containers are simulated based on the real containers used for zebrafish visual research.

- Petri dish lid (e.g. 35 mm diameter, Figure 1B): The fish is embedded at the bottom of the lid, while the lid is located on a platform.
- Cylindrical container (Figure 1C): The animal is placed on a small, custom-made stage in the middle of the cylinder. A camera is available from below to monitor fish behaviours.
- Glass bulb (Figure 1D): The animal is mounted on a small triangular stage and the whole glass bulb is held by a stand at the rear.

Inputs

The main inputs, indices of refraction (IOR) for different containers, are listed in the table below for the photorealistic modelling.

containers	Petri dish lid	Cylindrical container	Glass bulb
material	Polystyrene	Acrylic glass	Glass Schott Boro
IOR	1.57	1.49	1.473

Stimulus

For optical testing, a coloured checkerboard pattern, consisted of 36 columns and 18 rows, was used to differentiate the main directions (up/down and right/left, marked by a letter 'L' to identify mirroring).

Renderer

The images were usually rendered using the Cycles renderer. Only in special tasks, such as the visualization the light beam path and the analysis of dispersion, images were rendered with LuxCoreRender using bidirectional path tracing, appropriate volume scattering and camera clipping.

Physical background

Snell's Law	$n_i \sin \varepsilon_i = n_t \sin \varepsilon_t$	the angle of incidence (ε_i) and the angle of refraction/transmission (ε_t) with given indices of refraction n_i and n_t for two media.
Fresnel Equations	$R_s = \frac{ n_i \cos \varepsilon_i - n_t \cos \varepsilon_t ^2}{ n_i \cos \varepsilon_i + n_t \cos \varepsilon_t ^2}$	R_s , the reflectance for s-polarized light
Fresnel Equations	$R_p = \frac{ n_i \cos \varepsilon_t - n_t \cos \varepsilon_i ^2}{ n_i \cos \varepsilon_t + n_t \cos \varepsilon_i ^2}$	R_p , the reflectance for p-polarized light
	$R_{\text{eff}} = \frac{1}{2}(R_s + R_p)$	R_{eff} , the total reflectance of unpolarised light
	$T = 1 - R$	T, the fraction of the transmitted power; R, the fraction of the reflected power;

Animal care and transgenic lines

All animal procedures conformed to the institutional guidelines of the Universities of Tübingen and the local government (Regierungspräsidium Tübingen). The transgenic zebrafish line *Tg(HuC:GCaMP5G)a4598Tg* was used in this study. Transgenic line was kept in either a TL or TLN (nacre) background. Zebrafish larvae were raised in E3 medium until day 5 or 6 post-fertilization (dpf).

Experiment protocols and data analysis

The monocular direction selectivity experiment protocol was the same as before (Wang et al., 2019) except that the small petri dish was used instead of the glass bulb. The monocular RF mapping protocol was described before (Wang et al., 2020). In this study, a larger glass bulb with a diameter of 10 cm was used, in which case the water level was only 1 cm above the glass bulb centre. Data analysis was performed with Matlab script (MOM_Load, Midbrain_Localizer and Cell_Viewer) available online (https://gin.g-node.org/Arrenberg_Lab) (Wang et al., 2019, Wang et al., 2020, Kubo et al., 2014, Miri et al., 2011).

Quantification and statistical analysis

The statistical information calculated with Matlab R2014b built-in functions is provided in each of the sections above. For statements of significance an alpha level of 0.05 was used unless stated otherwise.

The analysed number of zebrafish and brains is indicated in the main text and figure legends. Error bars correspond to SEM unless stated otherwise.

Acknowledgments

We thank Väinö Haikala and Dierk F. Reiff for help with the visual stimulus arena. We furthermore thank Thomas Nieß (glassblower shop, University of Tübingen) and Klaus Vollmer (fine mechanics workshop, University Clinic Tübingen) for technical support. This work was funded by the Deutsche Forschungsgemeinschaft (DFG) grants EXC307 (CIN – Werner Reichardt Centre for Integrative Neuroscience) and INST 37/967-1 FUGG, and a Human Frontier Science Program (HFSP) Young Investigator Grant RGY0079.

Author contributions

KW performed the experiments on tectal somatic responses. BA simulated the three containers and the corresponding optical light beams and stimulus patterns in the containers. KW and JH analysed the data. ABA, BA, KW, and JH conceived the experiments and associated analysis protocols. KW, BA, and ABA wrote the manuscript.

Declaration of Interests

The authors declare no competing interests.

Data and code availability

All raw and processed data and software used to generate the figures will be made available upon request.

Reference

- ABBAS, F., TRIPLETT, M. A., GOODHILL, G. J. & MEYER, M. P. 2017. A Three-Layer Network Model of Direction Selective Circuits in the Optic Tectum. *Front Neural Circuits*, 11, 88.
- AHMADLOU, M., ZWEIFEL, L. S. & HEIMEL, J. A. 2018. Functional modulation of primary visual cortex by the superior colliculus in the mouse. *Nat Commun*, 9, 3895.
- AHRENS, M. B., LI, J. M., ORGER, M. B., ROBSON, D. N., SCHIER, A. F., ENGERT, F. & PORTUGUES, R. 2012. Brain-wide neuronal dynamics during motor adaptation in zebrafish. *Nature*, 485, 471-7.
- BERGMANN, K., MEZA SANTOSCOY, P., LYGDAS, K., NIKOLAEVA, Y., MACDONALD, R. B., CUNLIFFE, V. T. & NIKOLAEV, A. 2018. Imaging Neuronal Activity in the Optic Tectum of Late Stage Larval Zebrafish. *J Dev Biol*, 6.
- BIANCO, I. H. & ENGERT, F. 2015. Visuomotor transformations underlying hunting behavior in zebrafish. *Curr Biol*, 25, 831-46.
- BOULANGER-WEILL, J., CANDAT, V., JOUARY, A., ROMANO, S. A., PEREZ-SCHUSTER, V. & SUMBRE, G. 2017. Functional Interactions between Newborn and Mature Neurons Leading to Integration into Established Neuronal Circuits. *Curr Biol*, 27, 1707-1720 e5.
- DAMJANOVIC, I., MAXIMOVA, E. & MAXIMOV, V. 2009. Receptive field sizes of direction-selective units in the fish tectum. *J Integr Neurosci*, 8, 77-93.
- DUNN, T. W. & FITZGERALD, J. E. 2019. Correcting for physical distortions in visual stimuli improves reproducibility in zebrafish neuroscience. *bioRxiv*.

- KUBO, F., HABLITZEL, B., DAL MASCHIO, M., DRIEVER, W., BAIER, H. & ARRENBURG, A. B. 2014. Functional architecture of an optic flow-responsive area that drives horizontal eye movements in zebrafish. *Neuron*, 81, 1344-59.
- MASSECK, O. A. & HOFFMANN, K. P. 2009. Question of reference frames: visual direction-selective neurons in the accessory optic system of goldfish. *J Neurophysiol*, 102, 2781-9.
- MIRI, A., DAIE, K., BURDINE, R. D., AKSAY, E. & TANK, D. W. 2011. Regression-based identification of behavior-encoding neurons during large-scale optical imaging of neural activity at cellular resolution. *J Neurophysiol*, 105, 964-80.
- NIELL, C. M. & SMITH, S. J. 2005. Functional imaging reveals rapid development of visual response properties in the zebrafish tectum. *Neuron*, 45, 941-51.
- PORTUGUES, R., FEIERSTEIN, C. E., ENGERT, F. & ORGER, M. B. 2014. Whole-brain activity maps reveal stereotyped, distributed networks for visuomotor behavior. *Neuron*, 81, 1328-1343.
- PREUSS, S. J., TRIVEDI, C. A., VOM BERG-MAURER, C. M., RYU, S. & BOLLMANN, J. H. 2014. Classification of object size in retinotectal microcircuits. *Curr Biol*, 24, 2376-85.
- RAUT, H. K., GANESH, V. A., NAIR, A. S. & RAMAKRISHNA, S. 2011. Anti-reflective coatings: A critical, in-depth review. *Energy & Environmental Science*, 4, 3779.
- REISER, M. B. & DICKINSON, M. H. 2008. A modular display system for insect behavioral neuroscience. *J Neurosci Methods*, 167, 127-39.
- RINNER, O., RICK, J. M. & NEUHAUSS, S. C. 2005. Contrast sensitivity, spatial and temporal tuning of the larval zebrafish optokinetic response. *Invest Ophthalmol Vis Sci*, 46, 137-42.

- ROMANO, S. A., PIETRI, T., PEREZ-SCHUSTER, V., JOUARY, A., HAUDRECHY, M. & SUMBRE, G. 2015. Spontaneous neuronal network dynamics reveal circuit's functional adaptations for behavior. *Neuron*, 85, 1070-85.
- RUST, N. C., SCHWARTZ, O., MOVSHON, J. A. & SIMONCELLI, E. P. 2005. Spatiotemporal elements of macaque v1 receptive fields. *Neuron*, 46, 945-56.
- SAJOVIC, P. & LEVINTHAL, C. 1982. Visual cells of zebrafish optic tectum: mapping with small spots. *Neuroscience*, 7, 2407-26.
- SCHUSTER, S., ROSSEL, S., SCHMIDTMANN, A., JAGER, I. & PORALLA, J. 2004. Archer fish learn to compensate for complex optical distortions to determine the absolute size of their aerial prey. *Curr Biol*, 14, 1565-8.
- SIMPSON, J. I., LEONARD, C. S. & SOODAK, R. E. 1988. The accessory optic system of rabbit. II. Spatial organization of direction selectivity. *J Neurophysiol*, 60, 2055-72.
- WANG, K., HINZ, J., HAIKALA, V., REIFF, D. F. & ARRENBURG, A. B. 2019. Selective processing of all rotational and translational optic flow directions in the zebrafish pretectum and tectum. *BMC Biol*, 17, 29.
- WANG, K., HINZ, J., ZHANG, Y., THIELE, T. R. & ARRENBURG, A. B. 2020. Parallel Channels for Motion Feature Extraction in the Pretectum and Tectum of Larval Zebrafish. *Cell Rep*, 30, 442-453 e6.
- WYLIE, D. R., BISCHOF, W. F. & FROST, B. J. 1998. Common reference frame for neural coding of translational and rotational optic flow. *Nature*, 392, 278-82.
- ZHANG, M., LIU, Y., WANG, S. Z., ZHONG, W., LIU, B. H. & TAO, H. W. 2011. Functional elimination of excitatory feedforward inputs underlies developmental refinement of visual receptive fields in zebrafish. *J Neurosci*, 31, 5460-9.

ZIMMERMANN, M. J. Y., NEVALA, N. E., YOSHIMATSU, T., OSORIO, D., NILSSON, D. E.,
BERENS, P. & BADEN, T. 2018. Zebrafish Differentially Process Color across Visual
Space to Match Natural Scenes. *Curr Biol*, 28, 2018-2032 e5.

Figures and legends

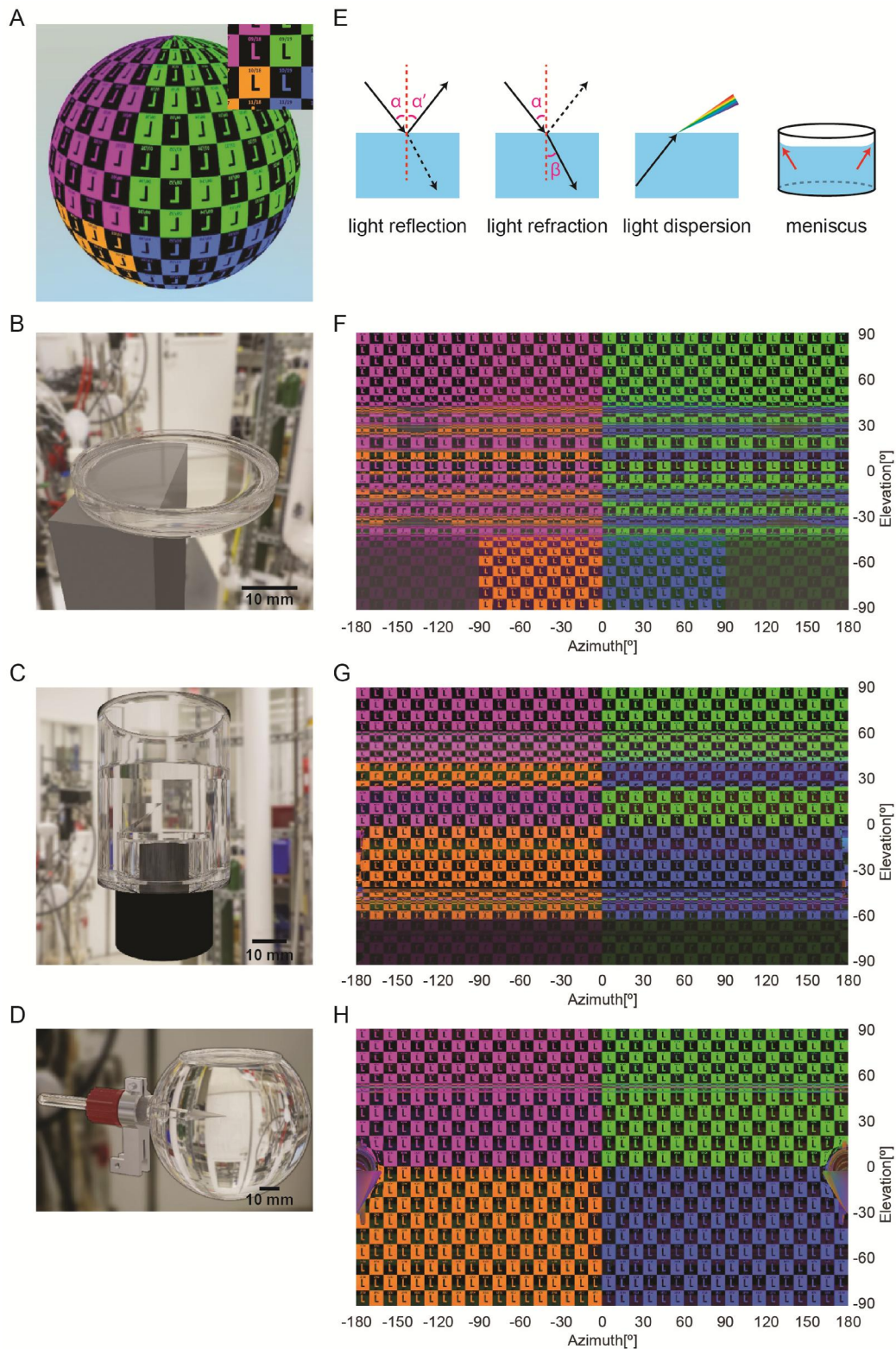


Figure 1. Photorealistic illustration (3D rendering) of three containers coupled with stages and simulated visual patterns seen from the perspective of the fish in the

centre of corresponding containers. (A) The sphere in the centre shows outside view of checkerboard stimulus under ideal optical condition. Letter ‘L’s with coloured backgrounds distributed in four quarters and aligned in 18 rows and 36 columns, indicate directions (left, right, up and down) and locations. Right up corner, a patch of the checkerboard stimulus (0° in elevation; 0° in azimuth) seen from the inner centre of the container. **(B)** Simulation of a commercially available Petri dish lid (35 mm in diameter) on a metal stage. **(C)** Simulation of a plastic cylindrical container made by a fine mechanics workshop (40 mm in diameter) on a camera lens holder. **(D)** Simulation of a custom-made glass bulb (80 mm in diameter) attached to a holder. **(E)** A diagram of light reflection, refraction, dispersion and water meniscus. Black arrows represent light beams and vertical dashed lines indicate normal planes. Angles α , α' , and β indicate angles of incidence, reflection and refraction. Red arrows indicate meniscus on the interface of a container and water on the water surface. **(F)** A two-dimension plot of the stimulus pattern in (A) seen from the centre of the Petri dish lid. **(G)** A two-dimension plot of the stimulus pattern in (A) seen from the centre of the cylindrical container. **(H)** A two-dimension plot of the stimulus pattern in (A) seen from the centre of the glass bulb stage. In panels (F) to (H), the azimuth and elevation angles are labelled below and on the right side.

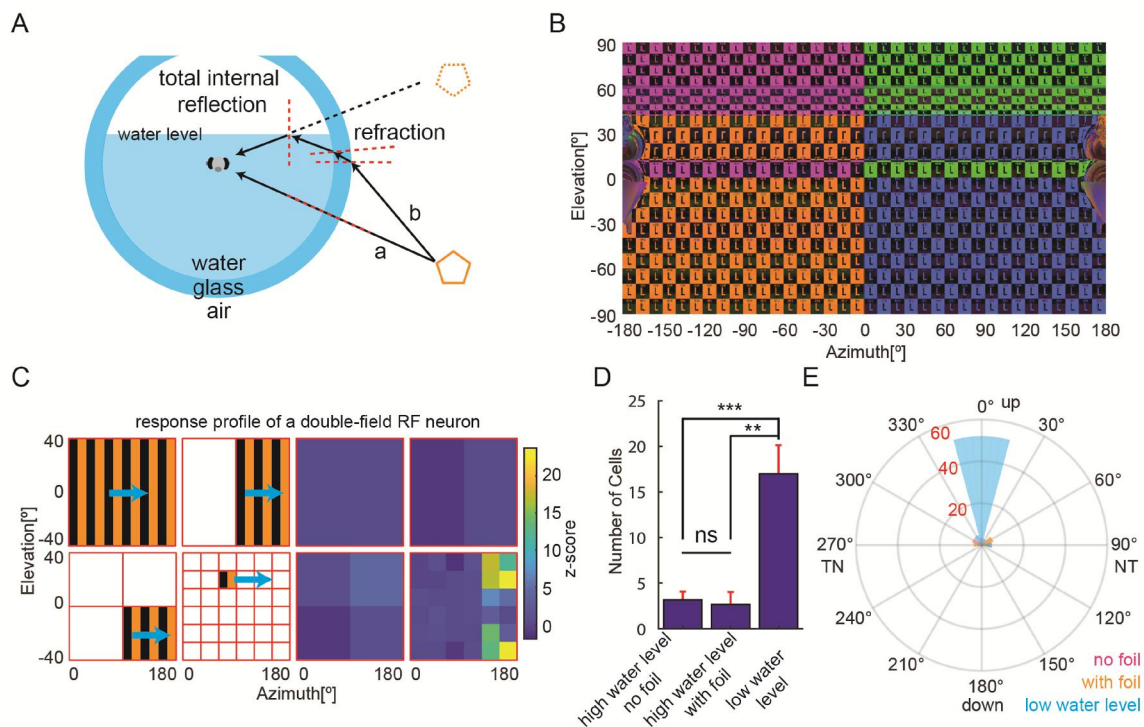


Figure 2. Low water level in the glass bulb results in artificial double-field RFs due to the total internal reflection. (A) An illustration of the TIR generated from low water level. The orange pentagon represents one object below the centre of the glass bulb. Light beam a

is perpendicular to the air-glass-water interface and reaches the right eye of the fish directly. On the contrary, light beam b, which originates from the same light source as light beam a, is refracted twice on the air-glass-water interface and then is totally reflected back to the right eye of the fish from above via the water-air interface. Black arrows, light beams; dashed red lines, normal planes; dashed orange pentagon, reflection of the orange pentagon. **(B)** A two-dimension plot of the ideal stimulus pattern seen from the centre of the glass bulb stage with low water level (only 7 mm above the fish back). Part of the visual stimulus below the equator is reflected to the upper visual field via TIR (the reversed blue and orange letter 'L's). **(C)** The response profile of a double-field RF. Left side, a simple diagram of the monocular RF mapping protocol (Supplementary Figure S3 shows the whole protocol). Vertical moving gratings of different sizes and locations were presented to the right eye of the animal. The cyan arrows indicate the moving direction. Right side, the z-score of the calcium signal of a double-field RF neuron in each motion phase corresponding to the phases shown on the left. The neuron responded exclusively in several motion phases corresponding to the 6x6 small-size patches. Two separate responsive centres are located in the upper temporal and lower temporal view fields, respectively. **(D)** The average numbers of double-field RF neurons in each fish measured under different experimental conditions. ***, $p < 0.001$; **, $p < 0.01$; ns, no significant differences; $n = 6$ (3 composite fish brain, high water level no foil), 6 (3 composite fish brain, high water level with foil) and 4 (2 composite fish brain, low water level) recordings. **(E)** The polar distribution of the degree angle of the line across the two RF centres from each double-field RF. TN, temporalnasal direction; NT, nasaltemporal direction. The neurons numbers are labelled with red numbers. The recording numbers are same as in panel (D).

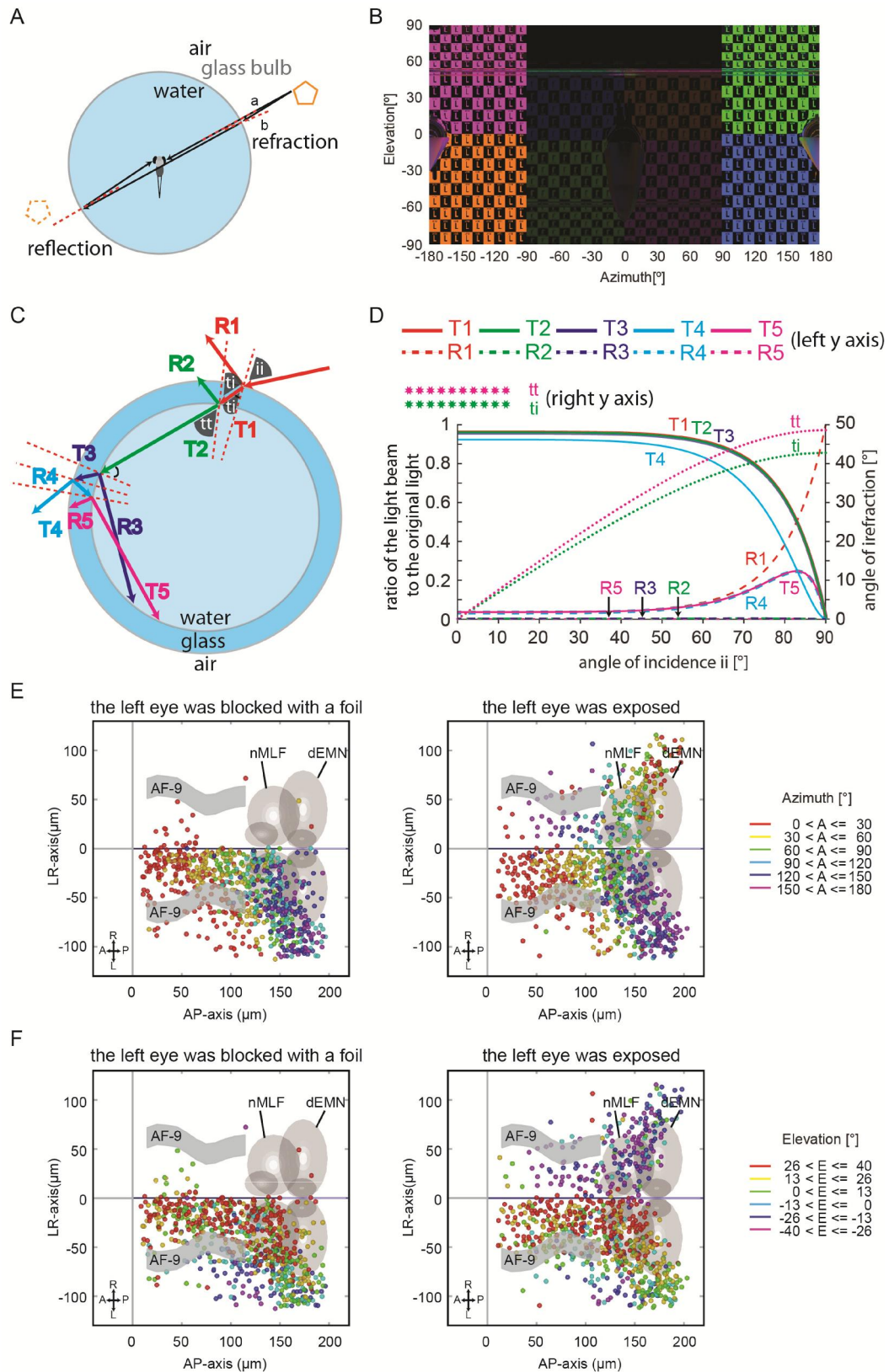


Figure 3, Reflection from the air-glass-water interface within the glass bulb activated the neurons corresponding to the unstimulated eye. (A) A simple illustration of the light

reflection from the air-glass-water interface to the unstimulated eye due to light reflection and refraction. Light beams a and b come from the same point of one object (orange pentagon). Light beam a, perpendicular to the glass bulb surface, reaches the right eye of the fish directly without refraction. In this case, no reflection occurs on the opposite side (relative to the fish) of the light source since the light beam is absorbed by the fish right eye. Light beam b, not perpendicular to the glass bulb surface and with a small incidence angle, is refracted and reflected to the left eye due to its large size but does not reach the glass bulb centre. **(B)** The rear of the fish (90° to 180° and -90° to -180° in azimuth) shows the checkerboard stimulus seen from the centre of the glass bulb stage. The front half (-90° to 90° in azimuth) shows the reflection of the checkerboard stimulus from the rear of the fish while the original visual stimulus pattern in frontal region is omitted. **(C)** The light reflection and refraction of a light beam shed into the glass bulb in detail. Reflective and transmitted refracted light beams are labelled with letters 'R' and 'T', respectively. Angles i_i and t_i indicate the angles of incidence and refraction for the first refraction on the air-glass interface. Since the glass is thin and the refractive angle t_i is relatively small, the angle of incidence for the second refraction approximates the first refractive angle t_i . The original light beam is theoretically refracted and reflected infinite times. But the majority of light power is contained in the light beams shown in the figure and other light beams are negligible. Light beams R3 and T5 can reach the unstimulated eye when the incidence angle i_i of the original light beam is small. **(D)** Final reflection and refraction rates of the light and angles of refraction calculated according to the Fresnel equation and Snell's law when the angle of incidence i_i increases from 0° to 90° . The colours correspond to the colours and light beams in panel (C). T5 is about 14 times stronger than R3 when the incidence angle i_i is smaller than 30° . **(E)** Topographic maps of tectal small-size RF neurons in azimuth when the left unintended eye was covered by a black foil (left) or not (right). Each coloured dot represents a single neuron with its receptive field centre in the corresponding azimuth range. For example, all receptive field centres of the neurons in red are located between 0° azimuth (in front of the fish) and 30° azimuth on the nasal right side of the fish. $n = 6$ fish, 3 composite brains. **(F)** Topographic maps of tectal small-size RF neurons in elevation when the left unintended eye was covered by a black foil (left) or not (right). Each coloured dot represents a single neuron with its receptive field centre in the corresponding elevation range. For example, receptive field centres of the neurons in green are located slightly above the equator of the view field (0° to 13° in elevation). $n = 6$ fish, 3 composite brains.

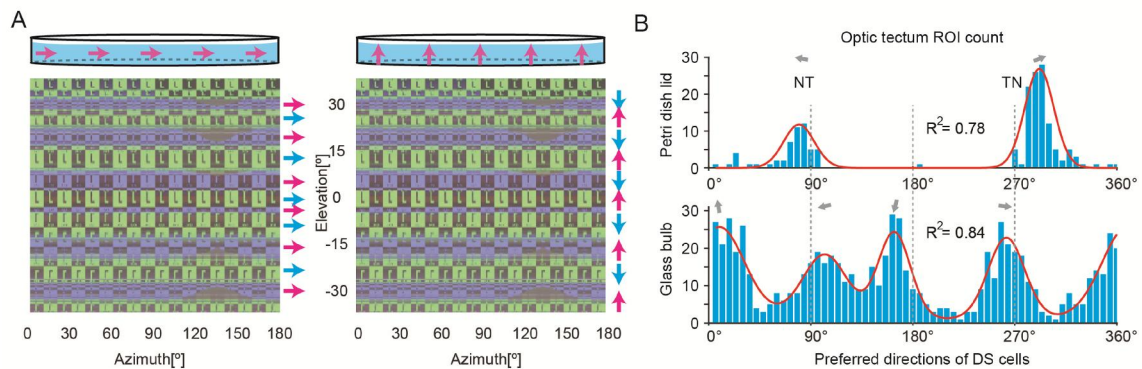


Figure 4, vertical motion seen from the centre of the Petri dish lid is disrupted due to light refraction and reflection. (A) Because of the light refraction and reflection, the visual stimulus patterns near the horizontal equator (-41° to 41° in elevation) from below and above are intermingled and reversed (background, also see Figure 1F). Left side, horizontal motion (indicated with magenta arrows) to the right is presented from outside of a Petri dish lid. Seen from the centre of the Petri dish, the whole moving pattern is still continuous, consistent and homogeneous (cyan and magenta arrows). Right side, vertical upward motion (indicated with magenta arrows) is presented from outside of a Petri dish. The whole moving pattern is disrupted and not continuous from the perspective of the animal in the centre of the container. On different elevation levels, the stimulus patterns move upwards (magenta arrows) or in the opposite direction (cyan arrows). **(B)** Histograms of the preferred directions of direction-selective tectal neurons recorded with a Petri dish lid (top, $n = 5$ fish) or a glass bulb (bottom, $n = 9$ fish). The peaks were fitted with a sum of two (top) or four (bottom) Von-Mises functions (red lines). The PDs are indicated with grey arrows.

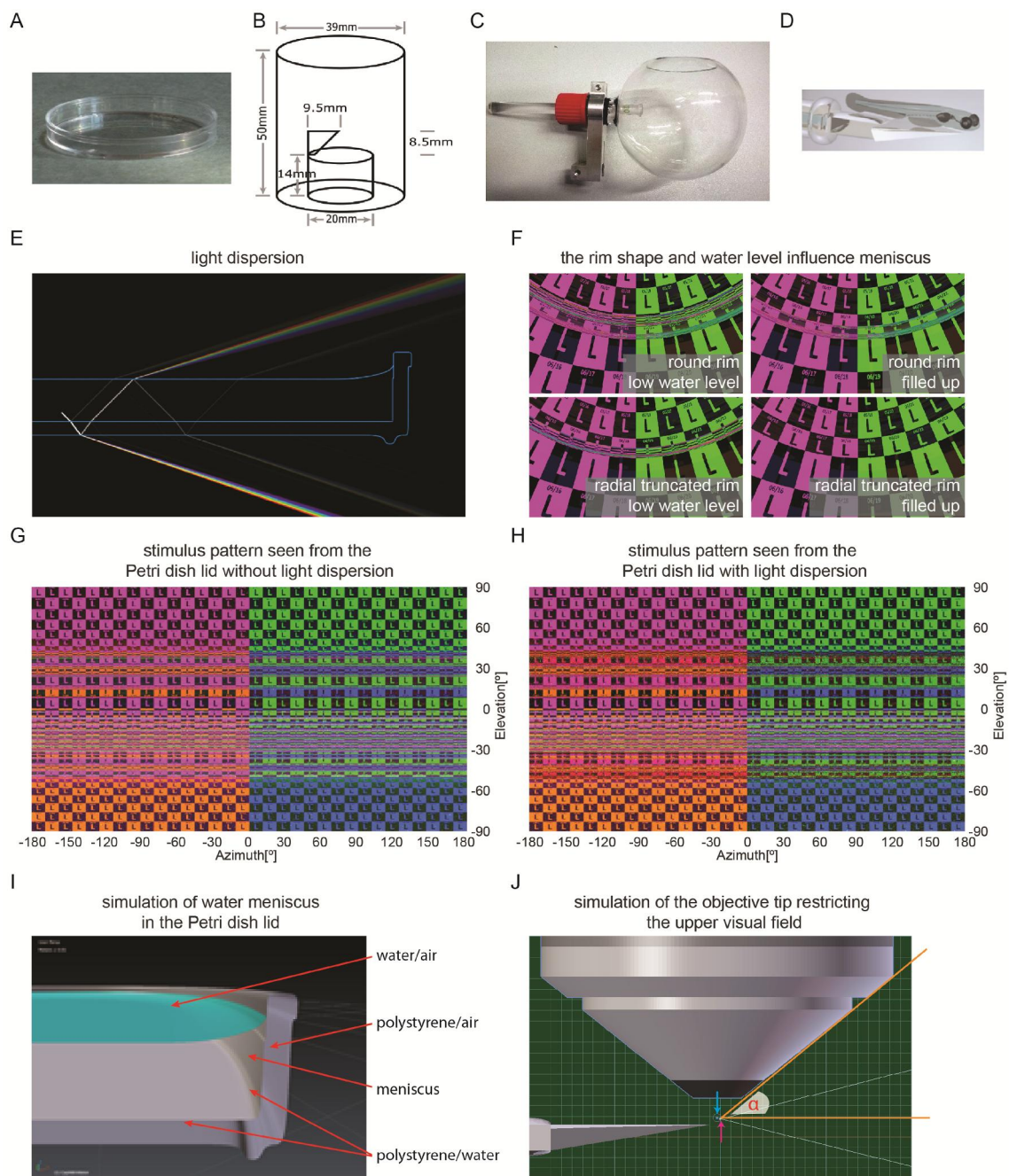


Figure S1. Three different containers for fish visual research and simulation of geometrical optics. Related to figure 1. (A) A commercially available Petri dish lid (35 mm in diameter). **(B)** A plastic cylindrical container made by a fine mechanics workshop (40 mm in diameter). **(C)** A custom-made glass bulb (80 mm in diameter) attached to its metal holder. **(D)** A simulation of a 5 dpf larval zebrafish is embedded in low melting agarose on a triangular stage. **(E)** A white light beam is shed 45° downwards in the centre of a Petri dish lid (side view). Because of different indices of refraction from the white light components,

light dispersion occurs on the water-air interface. **(F)** The rim shape and water level influence the water meniscus in the glass bulb. Using radial truncated rim and filling up the glass bulb with water reduce the optical influences of water meniscus. The view perspective is from the centre of the glass bulb centred at the view field of 0° in azimuth and 50° in elevation. **(G)** The checkerboard stimulus seen from the centre of the Petri dish lid (without the holder stage) without light dispersion. **(H)** The checkerboard stimulus seen from the centre of the Petri dish lid (without the holder stage) with light dispersion. Colour distortions and blurring exist in comparison to panel (G) but their influences are weaker than those of light refraction and reflection. **(I)** A symbolic simulation of water meniscus in the Petri dish lid (side view). On the inner wall of the Petri dish lid, the water level is higher than more central regions. **(J)** The accessible angle α (orange angle) of the fish to the visual stimulus is only 1° larger than the angle of the objective tip since the location of the fish eyes (magenta arrow) are roughly 0.3mm in front of the focus point (cyan arrow) of the objective.

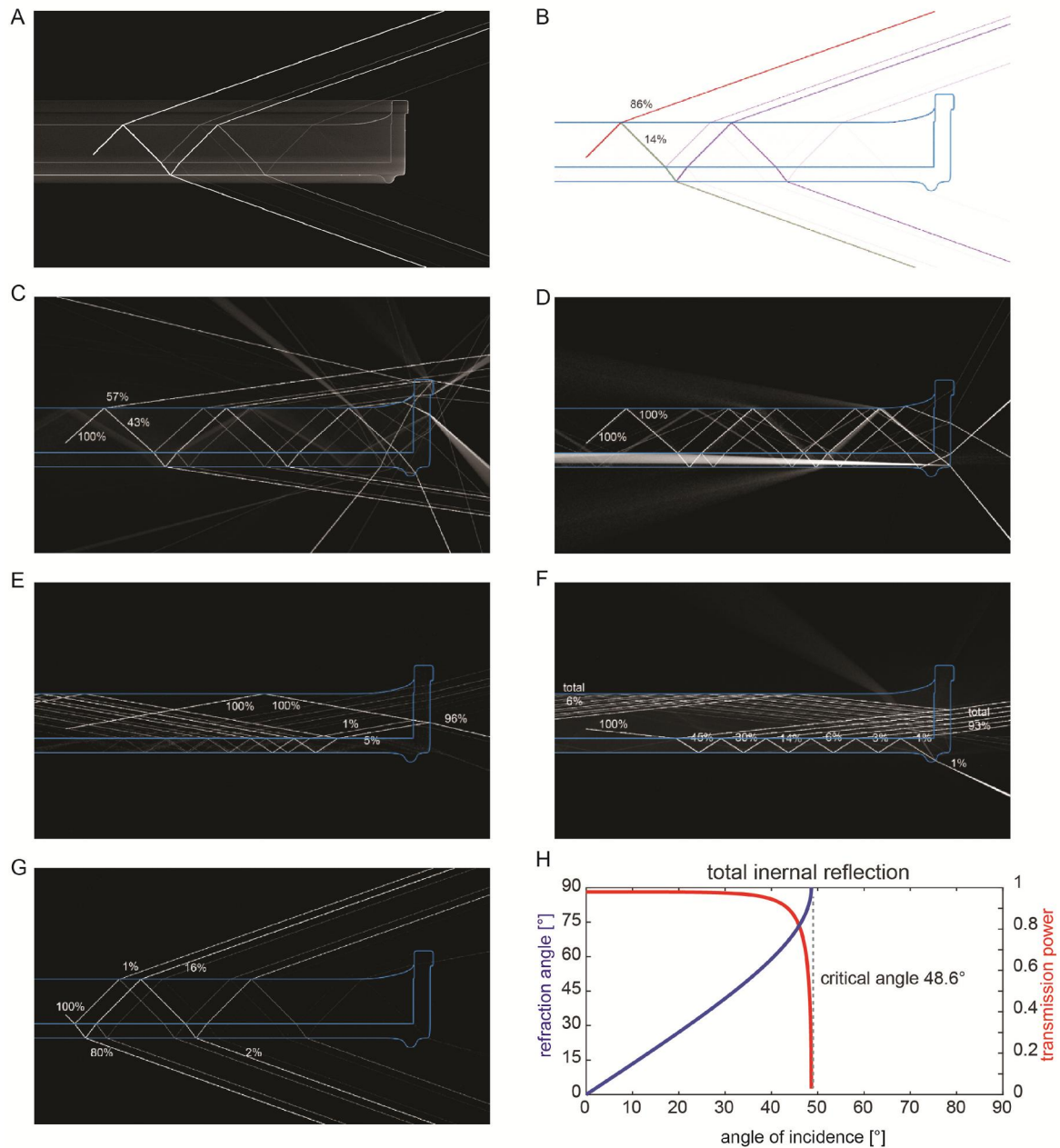


Figure S2. Simulation of the optics underlying visual stimulus distortion and blurring resulting from light fraction and reflection in the Petri dish lid. Related to Figure 1. For each panel from (A) to (G), only one single light beam is shown under different conditions (angles of incidence and directions). **(A)** A light beam is shed 45° (applicable from 0° to 48.6°) upwards. 86% of the light is refracted into the air and only 14% is reflected back. Light reflections and refractions continue to the Petri dish side wall. **(B)** The same as in panel (A) except that the light intensity is colour coded (red to purple representing 100% to 2% of original light power). **(C)** A light beam is shed 48° (applicable from 0° to 48.6°) upwards. 48% of the light is refracted into the air and only 43% is reflected back. Light reflections and

refractions continue to the Petri dish side wall. **(D)** A light beam is shed 49° (larger than critical angles, 48.6° from water to air and 39.6° from polystyrene to air) upwards. The light beams cannot be refracted from water or polystyrene to air. **(E)** The same as in panel (D) except that the light beam is shed 80° upwards. The light beam can only come out of the Petri dish lid through the vertical lid wall. **(F)** A light beam is shed 84° downwards. **(G)** A light beam is shed 45° downwards. **(H)** Refraction angle (in blue) and transmission power (in red) change when a light beam is projected from water (IOR = 1.333) to air (IOR = 1) and the angle of incidence increases from 0° to 90° . The critical angle of total internal reflection from water to air is indicated with a vertical dashed line.

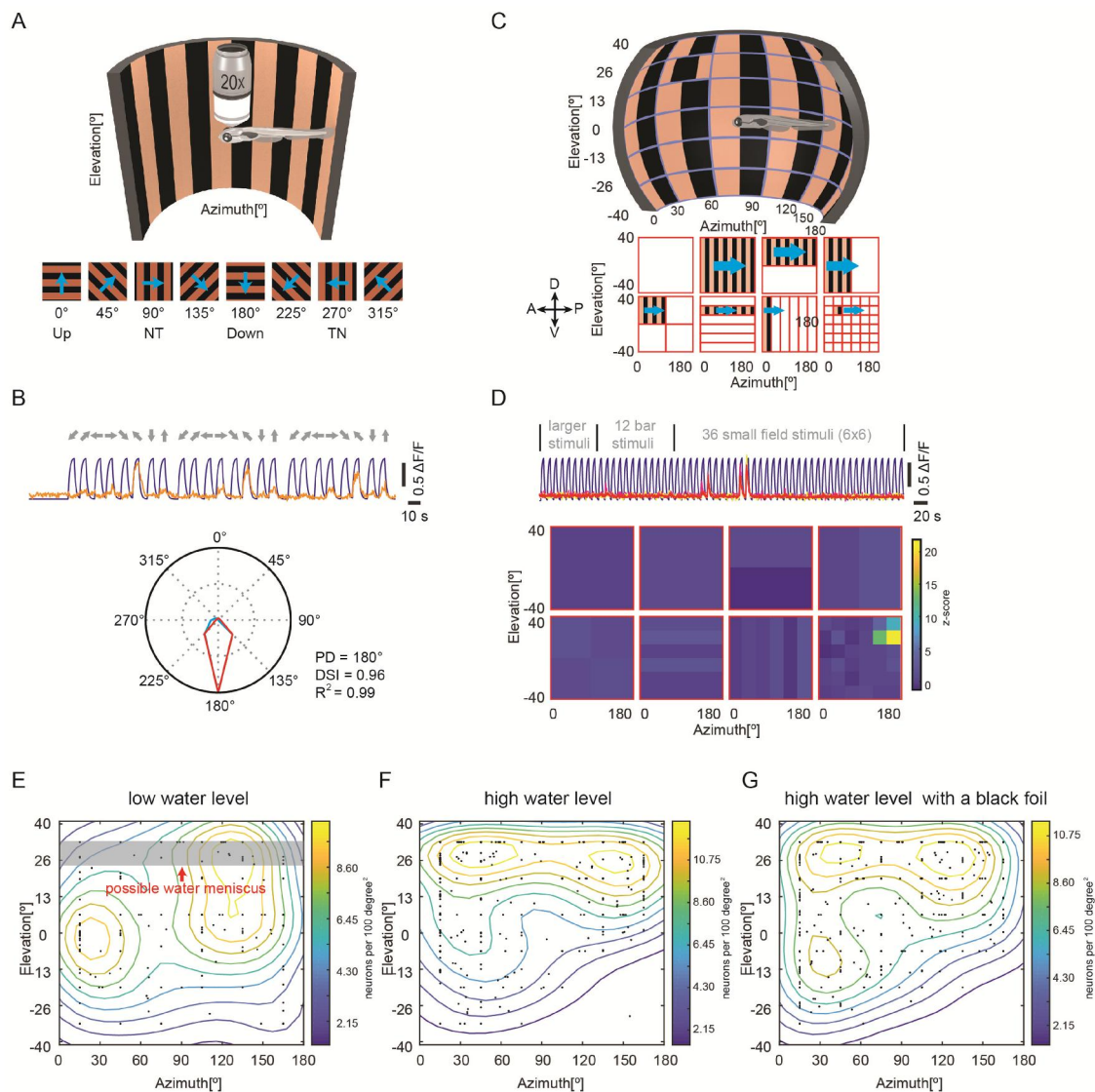


Figure S3. Experimental protocols for monocular direction selectivity analysis and RF mapping; low water level disrupts the distribution of receptive field centres from

small-size RF tectal neurons measured with the glass bulb. Related to Figures 2-4. (A)

A diagram of the monocular direction selectivity analysis setup. Upper, gratings, 0.033 cycles per degree, moving in eight different directions, were presented to the right eye of the animal, which was embedded in low melting agarose in the centre of the cylindrical half arena. The sizes of the fish and the arena are not proportional to the real experiments in this illustration. Below, an illustration of the 8 moving patterns. The cyan arrows indicate the moving directions. NT, nasaltemporal; TN, temporalnasal. **(B)** An example DS tectal neuron. Upper, the original calcium trace of the DS neuron in three repetitions (in orange). The blue background curve indicates the convolved ($\tau = 1.5$ s) motion-stationary phase regressor. Below, the DS tuning curve. The neuron responded most robustly to the downward motion. **(C)** A diagram of the monocular RF mapping protocol. Upper, vertical gratings (0.033 cycles per degree) with different sizes and locations were presented to the right eye of the animal, which was embedded in low melting agarose in the centre of the cylindrical half arena. The sizes of the fish and the arena are not proportional to the real experiments in this illustration. Below, an illustration of the whole visual stimulus protocol. The cyan arrows indicate the moving directions. A, anterior; P, posterior; D, dorsal; V, ventral. **(D)** The response profile of a small-size RF neuron plotted z-score. Upper, the original calcium traces (yellow, cyan and magenta) of the neuron in the three repetitions and their median (orange). The blue background curve indicates the convolved ($\tau = 1.5$ s) motion-stationary phase regressor. Below, the response profile of a small-size RF neuron plotted with z-score. The response in each phase is corresponding to one of the motion phases in panel (C). **(E-G)** Visual field locations and density contour plot of receptive field centres of small-size RF tectal neurons recorded with low water level (panel (E), $n = 4$ fish, 2 composite tecta), high water level without left eye covered (panel (F), $n = 6$ fish, 3 composite tecta) and high water level with left eye blocked by a black foil (panel (G), $n = 6$ fish, 3 composite tecta), respectively. In panel (E), the low neuron density in the upper visual field potentially resulted from water meniscus (grey shade).

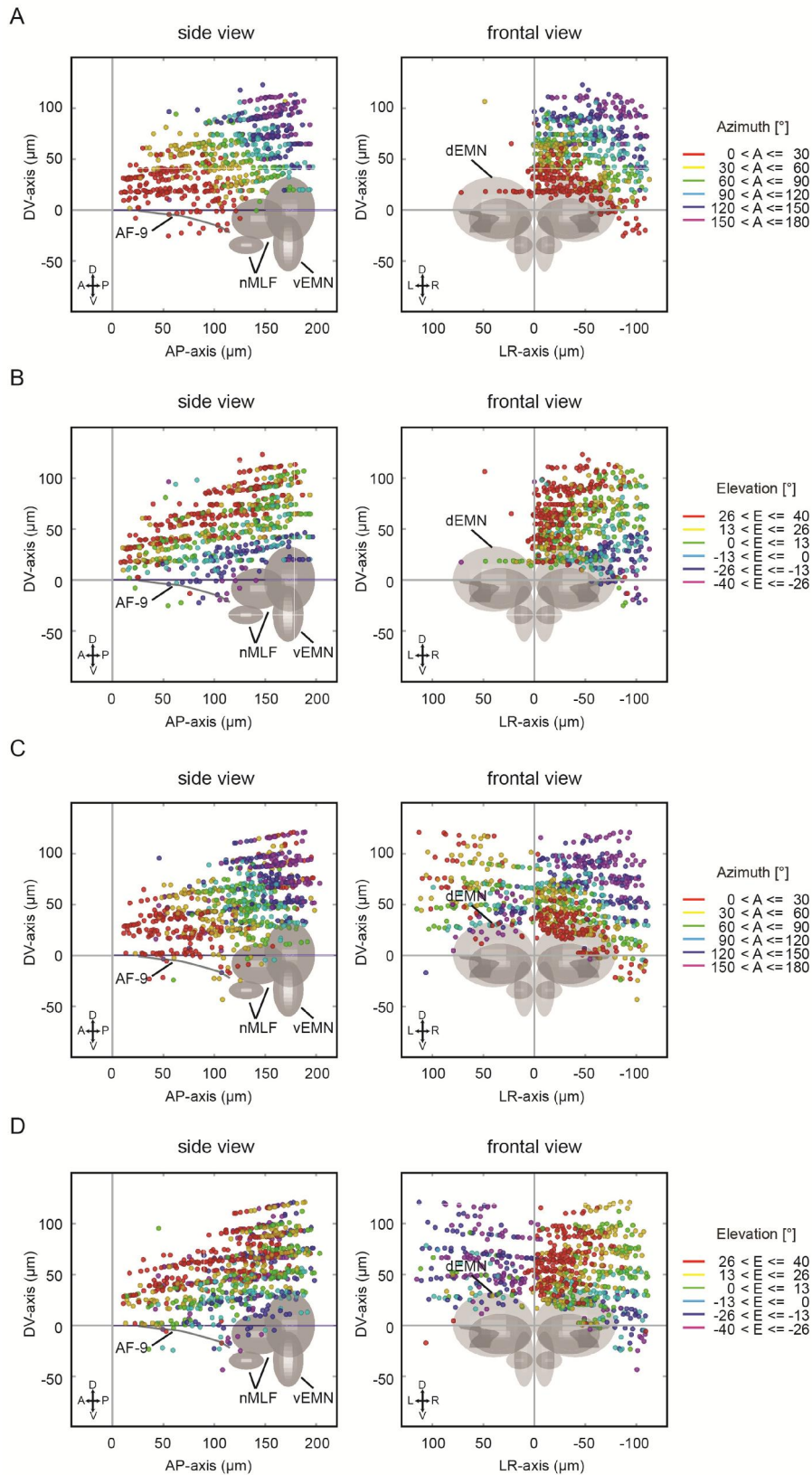


Figure S4. Reflection in inner surface of the glass bulb activated tectal neurons corresponding to the unstimulated eye. Related to Figure 3. (A, B) Topographic maps of

tectal small-size RF neurons in azimuth (A) or elevation (B), when the left unintended eye was covered by a black foil. Each coloured dot represents a single neuron with its receptive field centre in the corresponding azimuth (A) or elevation (B) range. For example, all receptive field centres of the neurons in red are located between 0° azimuth (in front of the fish) and 30° azimuth on the nasal right side of the fish (A). For example, receptive field centres of the neurons in green are located slightly above the equator of the view filed (0° to 13° in elevation) (B). n = 6 fish, 3 composite brains. **(C, D)** Topographic maps of tectal small-size RF neurons in azimuth (C) or elevation (D), when the left unintended eye was not covered by a black foil. Each coloured dot represents a single neuron with its receptive field centre in the corresponding azimuth (C) or elevation (D) range. For example, all receptive field centres of the neurons in red are located between 0° azimuth (in front of the fish) and 30° azimuth on the nasal right side of the fish (C). For example, receptive field centres of the neurons in green are located slightly above the equator of the view filed (0° to 13° in elevation) (D). n = 6 fish, 3 composite brains.

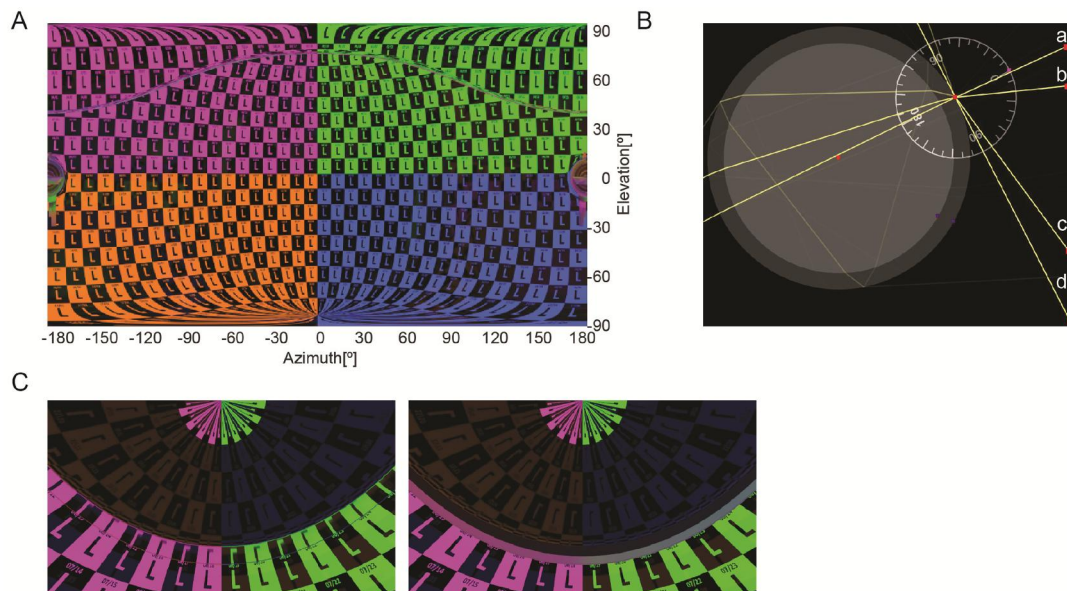


Figure S5. Other factors which influence the visual stimulus patterns perceived by the fish. Related to Figure 4 and the discussion. (A) An ideal checkerboard stimulus perceived when the animal is located 15 mm in front of the glass bulb centre. **(B)** Four light beams (a, b, c and d) are shed into the glass bulb with different angles of incidence simulated with software (Ray Optics Simulation). The indices of refraction from water (inner circle) and glass (outer ring) are 1.333 and 1.47. The reflected light reaches the unstimulated eye (close to the centre of the glass bulb) of the fish (left eye) only when the incidence angle of the visual stimulus is small (e.g., beam a). **(C)** Reflection of the stimulus pattern by microscope objective tips with different textures. Left side, glossy metal results in upside


down reflection (upside down letters 'L'); right side, Matt black and white, like Zeiss W N-Acroplan.

RESEARCH ARTICLE

Open Access



Selective processing of all rotational and translational optic flow directions in the zebrafish pretectum and tectum

Kun Wang^{1,2}, Julian Hinz^{1,2,3}, Väinö Haikala⁴, Dierk F. Reiff⁴ and Aristides B. Arrenberg^{1*} 

Abstract

Background: The processing of optic flow in the pretectum/accessory optic system allows animals to stabilize retinal images by executing compensatory optokinetic and optomotor behavior. The success of this behavior depends on the integration of information from both eyes to unequivocally identify all possible translational or rotational directions of motion. However, it is still unknown whether the precise direction of ego-motion is already identified in the zebrafish pretectum or later in downstream premotor areas.

Results: Here, we show that the zebrafish pretectum and tectum each contain four populations of motion-sensitive direction-selective (DS) neurons, with each population encoding a different preferred direction upon monocular stimulation. In contrast, binocular stimulation revealed the existence of pretectal and tectal neurons that are specifically tuned to only one of the many possible combinations of monocular motion, suggesting that further downstream sensory processing might not be needed to instruct appropriate optokinetic and optomotor behavior.

Conclusion: Our results suggest that local, task-specific pretectal circuits process DS retinal inputs and carry out the binocular sensory computations necessary for optokinetic and optomotor behavior.

Keywords: Optomotor response, Optokinetic response, Pretectum, Optic tectum, Zebrafish, Optic flow, Binocular integration, Calcium imaging

Background

Animals process optic flow and execute optokinetic (OKR) and/or optomotor responses (OMR) to actively stabilize their gaze and position relative to the visual world [1–6]. The underlying sensorimotor transformations involve direction-selective retinal ganglion cells (DS-RGCs) that project to the pretectum/accessory optic system (AOS). The pretectum in turn projects to (pre-)motor midbrain and hindbrain areas to evoke compensatory eye and tail movements [1, 7–10]. The optic tectum also receives DS-RGC inputs and is involved in detecting the location of small visual stimuli, as needed during prey capture behavior [11–13]. The directional tuning of neurons in the zebrafish pretectum is still unknown, while the optic tectum has been shown to be represented by four preferred directions, roughly

corresponding to up, down, temporal-to-nasal (TN), and nasal-to-temporal (NT) [12, 14, 15]. For the detection of ego-motion directions, comparing the motion information across the two eyes is an efficient strategy for lateral-eyed animals, which has been shown to be implemented in the zebrafish pretectum for certain directions [10]. Corresponding binocular neurons (selective for translational or rotational motion) have also been identified in other species [16, 17]. However, a recent study suggested that the hindbrain is necessary for the unambiguous identification of optic flow directions in zebrafish and reported the binocular sensory representation in the pretectum to be incomplete for this task [9].

Here, we investigated the binocular sensory representation in the main visual brain areas of zebrafish, the optic tectum and the pretectum. First, we characterized the direction selectivity of zebrafish pretectal and tectal neurons using monocular visual stimuli. Based on the preferred directions of these neurons, binocular stimulation was used to identify neurons selective for specific binocular visual

* Correspondence: aristides.arrenberg@uni-tuebingen.de

¹Werner Reichardt Centre for Integrative Neuroscience, Institute of Neurobiology, University of Tübingen, 72076 Tübingen, Germany
Full list of author information is available at the end of the article



stimulus combinations. For each of the six spatial degrees of freedom, we identified corresponding neurons selectively representing it. These binocular-selective neurons may evoke appropriate compensatory swim and eye movements by direct axonal projections to motor nuclei in the tectum and hindbrain [1, 18, 19]. Our results suggest that optic flow directions are readily detected in local, retinorecipient sensory circuits to support reflexive optomotor and optokinetic responses.

Results

Neurons of the pretectum and tectum prefer one of four cardinal motion directions during monocular stimulus presentation

Since monocular motion processing likely forms the basis for the comparison of binocular motion patterns, we first set out to investigate the representation of preferred motion direction (PD) using monocular gratings moving in eight different directions. Grating motion was presented to the right eye of larval zebrafish (*HuC:GCaMP5G*) [20] that broadly expressed GCaMP5G in the brain. Stimulus-associated changes in the concentration of somatic calcium ions in neurons of the diencephalon and midbrain were recorded using two-photon population calcium imaging (Fig. 1a–c) [10]. Tectal and pretectal brain regions were identified based on anatomical landmarks (Additional file 1: Figure S1A). Identified motion-sensitive neurons were further classified based on their orientation- (OS) or direction-selective (DS) responses (calculation of orientation and direction selectivity indices, OSI and DSI). Neurons were considered DS if the DSI was larger than 0.7 (Additional file 1: Figure S1C), and OS if OSI > 0.5 and DSI < 0.7. About half of the motion-sensitive neurons were DS (pretectum, $50 \pm 4\%$ (43/85); tectum, $56 \pm 3\%$ (68/120); mean \pm SEM across fish, $n = 9$ for both pretectum and tectum), and a minority were OS (pretectum, $3 \pm 0.8\%$ (3/85); tectum, $12 \pm 1.8\%$ (14/120); $n = 9$ fish). We identified 43 ± 7 DS neurons per recorded pretectum and 68 ± 5 DS cells per recorded tectum (Fig. 1d). The tuning specificity of DS neurons, measured by the normalized vector sum, varied greatly across neurons (Additional file 1: Figure S1D).

Tectal DS neurons were each tuned to one out of four preferred directions of motion (Fig. 1e), corresponding to up (9°), down (164°), TN (263°), and NT (103°). The observed preferred directions are comparable to those reported in a previous study [14]. We found that the four classes of DS neurons were approximately equally abundant (Fig. 1e), while horizontal directions were more prominently represented in the previous study [14]. Notably, DS neurons of the pretectum preferred the same directions (up, 358° ; down, 167° ; TN, 258° ; NT, 97°). Intriguingly, the preferred directions of neurons in

both the pretectum and tectum were not precisely orthogonal to each other: the angle between down and NT was smaller ($\sim 70^\circ$) and the angle between up and TN was larger ($\sim 100^\circ$) than 90° (Fig. 1e, f).

Tectal and pretectal DS neurons were predominantly identified in the brain hemisphere contralateral to the stimulated eye (laterality indices for tectum, 0.88 ± 0.04 ; pretectum, 0.70 ± 0.12 ; with a value of -1 corresponding to an exclusively ipsilateral and $+1$ to an exclusively contralateral placement of neurons). No salient anatomical clustering of functionally similar DS neurons was observed (Fig. 1g). In summary, our monocular stimulation experiments showed that the four Cartesian axes of motion are well represented in both tectum and pretectum.

Pretectal and tectal neurons encode specific binocular optic flow patterns corresponding to rotation or translation about or along the yaw, roll, or pitch axes

We have previously shown that many neurons of the zebrafish pretectum differentially respond to rotation and translation in the horizontal plane (clockwise, counter-clockwise, forward, or backward motion). Many of these neurons were selectively tuned to one specific binocular optic flow pattern [10]. Based on the assumption that the binocular responses result from simple combinations of synaptic inputs from monocular neurons and the four monocularly preferred directions identified above, stimulus motion along the rostral-caudal and dorsal-ventral axes was used in the binocular direction selectivity experiment. To investigate the three-dimensional binocular encoding of optic flow in the zebrafish brain and how the monocular visual representations are combined binocularly, we designed seven monocular stimulus patterns consisting of (1) stationary grating (St), (2) temporal-to-nasal motion (TN), (3) nasal-to-temporal motion (NT), (4) up, (5) down, (6) pitch down, and (7) pitch up. Presentation of each of these seven stimuli to both eyes resulted in $7 \times 7 = 49$ combinations of binocular stimulus patterns (Fig. 2a, b).

For each neuron, we identified the stimulus patterns for which the neuron was active (see “Materials and methods”). We then classified neurons into binary response types based on the active/silent status for all stimulus phases (Fig. 2c, d). We analyzed responses to St, TN, NT, up, and down separately from the responses to pitch stimuli (see “Materials and methods”). The binarization of neuronal response profiles during the first $5 \times 5 = 25$ stimulus phases (TN, NT, up, down, and St) resulted in 2^{25} (ca. 34 million) mutually exclusive, theoretically possible response types. The number of frequent response types, however, for which three or more neurons (Fig. 2e) were identified was much smaller than this: 49. These 49 response types (excluding pitch-specific response types) accounted for a large proportion (39%) of the recorded motion-sensitive neurons (300/763 neurons).

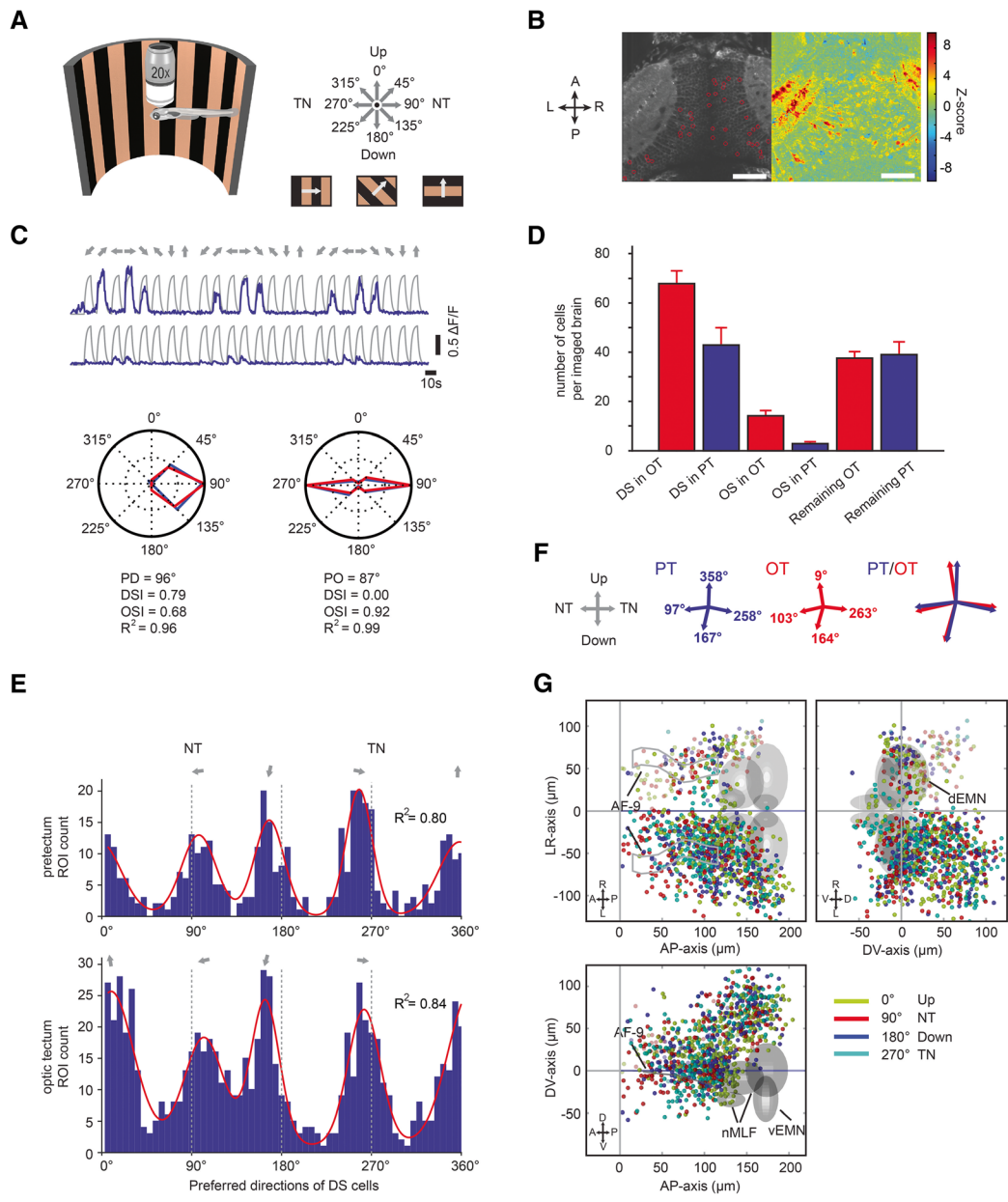


Fig. 1 Monocular motion stimuli reveal four orthogonal preferred directions in the zebrafish pretectum and optic tectum. **a** A half-cylindrical stimulus arena was used to present motion in eight different directions to the zebrafish (not drawn to scale). **b** Time-averaged optical slice of tectal GCaMP5G expression (left). The z-score heat map (right) was used to detect motion-sensitive pixels and circular regions of interest (ROIs) were drawn manually (left). Scale bar, 50 μm **(c)** Top: $\Delta F/F$ responses (of three stimulus repetitions) of two example neurons. Grey lines indicate the motion phases; their shape corresponds to the signal expected for a motion-sensitive cell (regressor, see “Materials and methods”). Bottom: Polar plots illustrating responses for each stimulus phase for one direction-selective (left) and one orientation-selective (right) cell. Blue lines correspond to the median $\Delta F/F$ from three repetitions, red lines to the fitted von-Mises function used to infer the preferred direction (PD), the direction and orientation selectivity indices (DSI and OSI), and the goodness of fit (R^2). **d** Number of identified DS and OS cells per recorded brain in optic tectum (OT) and pretectum (PT). Motion-sensitive cells that are neither DS nor OS are classified as “Remaining.” **e** Histograms of the preferred directions of direction-selective neurons in pretectum (top) and optic tectum (bottom) (pooled from nine imaged brains). The four peaks were fitted with a sum of four von-Mises functions (red line). **f** The four fitted peak directions from **e** are plotted for pretectum (blue) and optic tectum (red). Please note that in panels **e** and **f** the illustration arrow for NT points in a different direction than in panels **a** and **c**. We chose to switch arrangement to allow an easier comparison of panel **(e)** to the plots published in a previous report (Fig. 2a of Hunter et al [14]). **g** Anatomical maps of DS neurons (color-coded according to PD) in the tectum and pretectum. AF-9, arborization field 9-containing neuropil; nMLF, nucleus of the medial longitudinal fasciculus; vEMN/dEMN, ventral and dorsal extraocular motoneurons. Error bars correspond to SEM. A, anterior; P, posterior; L, left; R, right; D, dorsal; V, ventral

Within these 49 response types, about a third of the neurons (32%, 95/300) showed simple monocular DS responses without any contribution of motion presented to the other eye (Fig. 2d, top, and 2f). However, we also frequently observed binocular selective neurons, which were activated only during one specific combination of motion presented to the left and the right eye and silent to other combinations of motion (35%, 105/300, Fig. 2d, middle, and 2g). Among these binocular selective neurons, those coding for up-up (i.e., up to the right eye and up to the left eye), down-down, roll rightwards (down-up), roll leftwards (up-down), TN-TN (forward), and NT-NT (backward) were found frequently (5 to 17 neurons each). TN-NT and NT-TN neurons (yaw rotation-selective) were only found three times each. In our separate analysis of responses to pitch stimuli, we identified monocular pitch-responding neurons (Fig. 2h) and also four binocular pitch-selective neurons. Each of these pitch neurons was silent during the first 5×5 stimulus phases. Additional auxiliary analyses, which included all neurons and avoided forcing them into particular binary response types as above, confirmed the binocular selectivity of pretectal neurons (Additional files 1 and 2: Figures S1 and S2).

Taken together, our data show that a large fraction of the motion-sensitive pretectal and tectal neurons encode specific binocular optic flow patterns during horizontal, vertical, and pitch motion, resulting, among others, in translation- or rotation-selective responses in three different axes.

Pretectal computations can distinguish between optic flow stimuli that elicit forward swimming and turning OMR behavior

To investigate whether the same type of binocular selectivity also exists for stimulus combinations presented from below the animal, we analyzed a dataset from a previously published study [9] (Fig. 3a). The stimuli were chosen to elicit two different behaviors during certain stimulus phases: leftward/rightward OMR turning behavior was elicited by sideward visual motion and forward OMR swimming was elicited by forward visual motion [21, 22]. Five different monocular stimuli (leftward, rightward, forward, backward, and stationary gratings) were combined binocularly to achieve in total 10 different binocular stimulus phases (Fig. 3b, Inw, moving inward; Left, moving sideward to the left; Outw, outward; FW, forward; Right, moving to the right; RE, right eye, LE, left eye and BE, both eyes), resulting in $2^{10} = 1024$ possible binary response types. However, as in the experiment in Fig. 2, only a very small fraction of the theoretically possible response types were detectable in the activity recordings (Fig. 3c–e and the response profiles of the mirror-symmetrical rightward counterparts in Additional file 3: Figure S3). Activity was generally

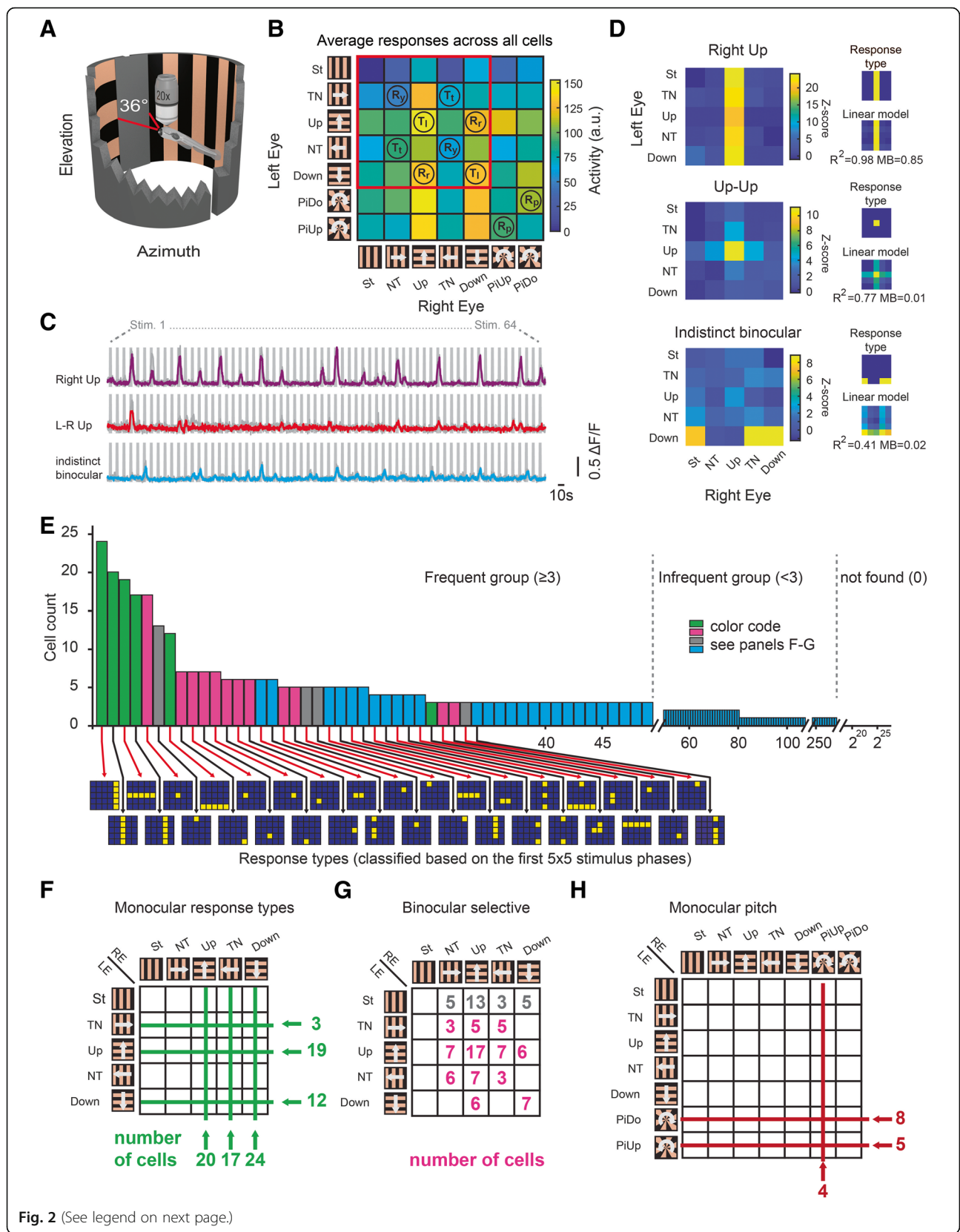
phase-locked to motion (Fig. 3b, motion phases are indicated by the colored bars which share the same colors of the icons above) and the eight most frequent response types (and their six mirror-symmetrical counterparts) encompassed 45% (753/1672) of the neurons (Fig. 3d, the indicated neuron numbers correspond to the sums of the response type pairs active during leftward and rightward motion, except for FW and BW response types.).

The frequent response types fall into three major response categories. First, more than 13% (176 + 44 neurons) were selective for optic flow corresponding to forward or backward translation. Second, 5% of the recorded neurons (88/1672) were selective for optic flow corresponding to sideward translation. Third, the other neurons showed responses that were not fully selective for either forward, backward, or sideward translation, i.e., they were also active during additional binocular stimulus combinations.

Discussion

We show that both pretectum and optic tectum contain monocular DS neurons tuned to one out of four roughly orthogonally arranged directions. In addition, monocular pitch-selective neurons were also identified. This layout is in agreement with previous reports on the pretectum/AOS in other species [1, 19, 23]. Zebrafish swim in a three-dimensional environment. During forward swimming, they mainly experience horizontal motion, although pitch angle changes are associated with swimming bouts [24]. The perpendicularly arranged preferred directions are potentially the result of efficient coding strategies. The angular spacing between the neighboring represented preferred directions does, however, not match precisely 90° in each case, and this “odd” angular spacing could potentially correspond to a specific adaptation of the zebrafish visual system, which still remains to be discovered and understood. Since zebrafish DS-RGCs show different directional preferences than somata in the pretectum/tectum [15, 25], a transformation of directional axes needs to be computed in the pretectum/tectum [13]. Since the optic chiasm is completely crossed in the lateral-eyed zebrafish, pretectal binocular integration is likely established by the intra-pretectal commissures connecting the pretectum across hemispheres (Fig. 4a, b). In our experiment, we detected about 49 frequent response types. These responses encode different binocular combinations of image motion in each eye along the four cardinal directions.

Most of our manually drawn regions of interest (see “Materials and methods”) corresponded to the contours of individual cells (Additional file 4: Figure S4), confirming that the binocular responsivity described in this study was only minimally affected by potential cross-talk from



(See figure on previous page.)

Fig. 2 Binocular selective neurons in the optic tectum and pretectum. **a** Two half-cylindrical arenas were used to present moving gratings. The binocular zone (nasal 36°) was blocked. **b** The stimulus protocol consisted of 7 × 7 binocular motion phases. A unique combination of stimuli (stationary: St, temporal-to-nasal: TN, upwards: Up, nasal-to-temporal: NT, downwards: Down, pitch up: PiUp, pitch down: PiDo) was shown to both eyes in each phase. For each stimulus combination, the summed activity (z-score) across motion-sensitive neurons is indicated in arbitrary units (a.u.). The red rectangle indicates the 5 × 5 stimulus phases further analyzed in panels **d–g**. R_p, R_r, R_y : binocular pitch, roll and yaw rotational stimulus phases. T_v, T_l : binocular thrust (forward/backward) and lift (up/down) translational stimulus phases (also see Fig. 4a). **c** Calcium responses of three example cells (median activity across three repetitions). The rectangular gray shades correspond to the 64 motion stimulus phases (Additional file 1: Figure S1E). **d** Calcium activity heat maps, classified binary response types and linear model fits of the cells from (c). **e** Binary response type analysis. The number of neurons (in pretectum and tectum, $n = 8$ animals, four composite brains, see “Materials and methods”) is plotted versus the ~34 million (2^{25}) theoretically possible binary response types. Green, monocular response types; magenta and gray, binocular-selective response types; light blue: indistinct binocular response types. The first 34 frequent response types are illustrated below. Yellow, responsive phases; blue, non-responsive phases. **f** The number of neurons for the frequent monocular response types (each line corresponds to one response type), **g** binocular-selective response types (active only during one binocular stimulus combination) and **h** monocular pitch-responding type (only active during the indicated monocular pitch phases) are indicated in green (monocular responsive), magenta (binocular selective), gray (stationary selective), and red (pitch responsive). LE/RE: left/right eye

multiple cells in our calcium imaging experiments. Many binocular neurons were selective for particular binocular combinations of visual stimuli that occur during translation, while being suppressed or non-responsive during any of the other combinations of binocular stimulus patterns. Furthermore, abundant sideward-selective responses were identified in the pretectum using stimuli presented from below (Fig. 3). Binocular rotational responses were also frequently observed, particularly for optic flow generated during roll or pitch, while yaw-specific responses were underrepresented. The number of identifiable binocular-selective neurons depends on the choice of the active/non-active threshold (Additional files 5 and 6: Figures S5 and S6). However, binocular-selective and monocular response types are still identifiable at each tested threshold, providing further support for our conclusions.

Our finding of abundant pretectal translation- and rotation-selective responses differs from findings reported in a recent study investigating zebrafish OMR circuits [9]. Since there were 10 stimulus phases, there were $2^{10} = 1024$ theoretically possible response types. However, in the authors' analysis, only the first eight stimuli (w/o forward and backward) were considered for building the response types, so that in their analysis the “sideward-selective” response type contained forward-responsive signals as well (see explicit example in Fig. 3e). This analysis difference explains why the forward translation-selective and sideward translation-selective pretectal responses have not been reported in the original study (see Fig. 5b in [9]).

The stimulus sets that were used in the experiments presented here were not fully realistic. For example, our forward “translation” stimulus (Fig. 2) did not contain realistic optic flow contraction in front of the animal as would be expected during backward ego-motion in a contrast-rich environment. Furthermore, some of the monocular motion stimuli (e.g., right eye inward in Fig. 3 and stimulus TN-St in Fig. 2) contained a stationary stimulus presented to one eye, which results in conflicting information for the fish. While presentation of such

stimuli helps scientists to understand how the zebrafish brain processes motion, such stimuli are unlikely to occur in nature and therefore might evoke different (e.g. smaller) brain responses than more naturalistic stimuli would evoke.

Our results are in agreement with reports on binocular neurons in the pretectum/AOS of other species [26–28]. However, in birds and goldfish, the preferred axes for rotations and translations have been shown to differ from the motion axes used in our stimulus set. Three preferred axes have been reported, with one corresponding to the vertical axis (yaw rotation, lift translation) and two axes located in the horizontal plane, oriented at 45° to either side of the midline [16, 29–32]. Such layout supports a common reference frame with the axes of the vestibular canals. In this study, we intended to investigate the binocular combination of the four monocularly preferred directions, which roughly correspond to the Cartesian directions (see Fig. 1). We therefore did not include stimuli containing binocular motion along or about the horizontal oblique axes suggested in previous studies. If the binocular neurons are not tuned to oblique directions of motion in any part of their receptive fields (which seems likely given that during monocular stimulation the vertical or horizontal motion is preferred, see Fig. 1), then the precise preferred (binocular) rotation and translation axes largely depend on the receptive field locations. Suppose a hypothetical neuron with one small receptive field patch in each eye, responding to up in the right eye and down in the left eye. In total, this neuron has two receptive field patches, like the binocular bipartite receptive fields that have been measured in the rabbit AOS [33]. If the receptive field patches were located laterally in each eye, the neuron would respond maximally to stimulus rotations about the roll axis. If, however, the receptive field patches were located on the equator but shifted nasally (by 45° relative to the lateral location) for the right eye and temporally for the left eye, the neuron would prefer

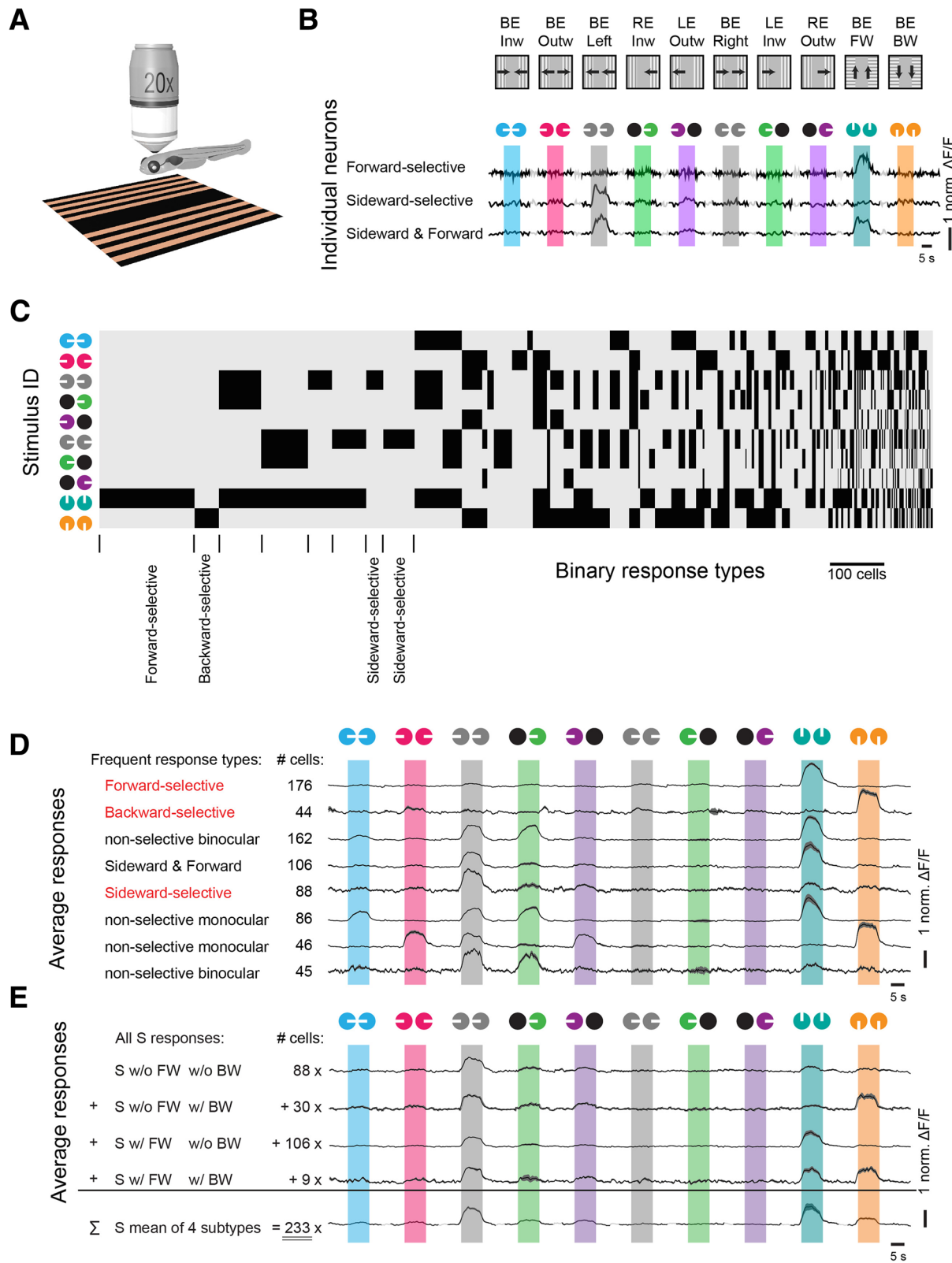


Fig. 3 (See legend on next page.)

(See figure on previous page.)

Fig. 3 Pretectal binocular selective neurons processing visual stimuli presented from below. **a** The visual stimulus was presented from below the animal, while calcium activity was recorded from above. **b** *Top*: Ten binocular stimulus phases were repeated 3 to 10 times. The black arrowheads indicate the gratings' moving directions. *Bottom*: normalized $\Delta F/F$ calcium responses for three examples, forward-selective, sideward-selective, and forward-and-sideward-selective neurons. White bars indicate the gratings' moving directions for the corresponding eyes (colored circles); black circles represent eyes when stationary gratings were presented. **c** Neuronal response types were classified based on the calcium activity during the ten stimulation phases (y-axis, black: active). The width in the x-axis corresponds to the cell number for each response type. Response types are ordered according to frequency. **d** Response profiles of the eight most frequent response types (Additional file 3: Figure S3 for the mirror-symmetrical response types). Response types labeled "non-selective" are active for more than one stimulus phase. Response types labeled "binocular" are influenced by stimulus motion presented to either eye. **e** Grouped and averaged response profiles of all neurons (leftward or rightward) that are sideward-selective, when only the first 8 stimulus phases are considered, corresponding to response type "S" in the previous study [9]. The first four rows show all possible response combinations for S type cells (including all 10 — not just 8 — stimulus phases) and the last row shows the weighted average of all S type neurons. The cell numbers correspond to the sum of S type cells and the mirror-symmetrical S' type cells. Note that the response type exclusively active for leftward motion (S w/o FW w/o BW, first row) cannot be detected when all responses are merged together (fifth row). In the study by Naumann et al., only this fifth merged response type has been reported

the horizontal axis identified in previous studies (+45° to the left from the midline). Since the receptive field sizes and centers have not been investigated in this study, more elaborate stimulus sets, including binocular oblique motion, would be necessary to identify the precise orientation of the preferred binocular motion axes for translation and rotation. This would allow to conclude whether the preferred motion axes in zebrafish correspond to those identified in other vertebrate species or not. Furthermore, knowledge about receptive field locations is needed to relate response types identified using sideward stimulation and stimulation from below. For example up-down binocular-selective neurons (Fig. 2) could correspond to sideward-selective neurons (Fig. 3), if the receptive fields of both eyes were located laterally and slightly below the equator of the view field.

We found that binocular responsive neurons are present in both pretectum and optic tectum. While the function of binocular neurons in the pretectum is likely related to its role in mediating OKR and OMR behavior (as discussed above and below), the role of binocular tectal neurons is less clear. While the optic tectum is dispensable for OKR and OMR in zebrafish [34], the tectal binocular neurons might still be involved in modulating these behaviors or be involved in different behaviors that require binocular representations. The high number of identified binocular response types (in comparison to the number of recorded neurons) made it difficult to compare binocular representations across the two brain areas. Ideally, the comparison of the binocular responsiveness in these two brain areas should also include an estimation of the receptive field sizes in each eye, since pretectal receptive fields are expected to be larger than tectal ones. However, receptive field size estimation was not included in this study, since the associated long stimulus protocol durations prohibited it.

In the invertebrate visual system of flies, the optic flow is considered to be encoded by the lobula plate tangential cells, mainly including vertical system neurons (VS)

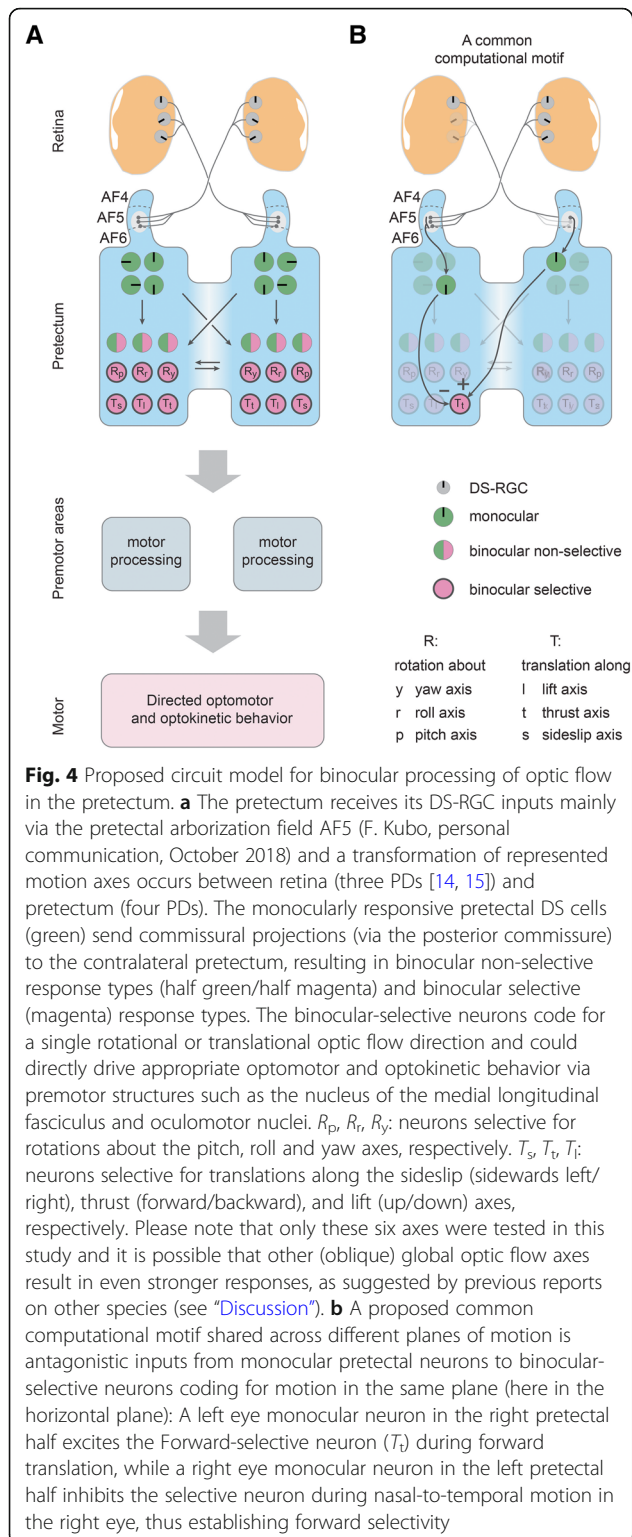
and horizontal system neurons (HS), which are directional selective for vertical and horizontal motion, respectively [35, 36]. Intriguingly, these neurons show large and complex monocular or binocular receptive fields, with different preferred directions across local receptive field positions, resembling the roll rotational or nasalward translational optic flow [36–39]. Similarly, bipartite receptive fields with opposing preferred directions, e.g., upwards and downwards, within one entire receptive field of one neuron have been identified in the rabbit AOS and pigeon vestibulocerebellum, though these bipartite receptive fields do not precisely match any optic flow pattern expected to occur during ego-motion [33, 40].

Taken together, our experiments and analyses revealed the existence of binocular sensory neurons in pretectum and optic tectum which are selective for optic flow corresponding to motion in each of the six degrees of freedom (Fig. 4): rotation (roll, pitch, yaw) and translation (lift, thrust, sideslip). These selective neurons could—in principle—directly instruct appropriate OKR and OMR behavior, since no further sensory processing is needed. Indeed, in the case of OKR, direct projections of pretectal neurons into a cranial nerve nucleus responsible for horizontal eye movements (nucleus abducens) have been shown to exist in other vertebrate species [1, 18, 19].

A biologically faithful model, describing each processing step from the retina to OMR and OKR behavioral outputs, would significantly advance our understanding of neural processing principles in the vertebrate brain. Future studies are needed to investigate the connectivity of functionally identified cells in the pretectum, as well as the receptive field properties of DS-RGCs and pretectal neurons.

Conclusion

The optic tectum and pretectum of larval zebrafish contain motion-sensitive neurons, which each prefer one out of four directions (up, down, temporal-to-nasal, nasal-to-



temporal). Many neurons are binocular selective and respond maximally to either rotational or translational motion along or about one of three orthogonally arranged axes.

Materials and methods

Contact for reagents and resource sharing

Further information and requests for resources and reagents should be directed to the Contact Aristides Arrenberg (aristides.arrenberg@uni-tuebingen.de).

Animal care and the transgenic line

All animal procedures conformed to the institutional guidelines of the University of Tübingen. The previously described transgenic zebrafish line *Tg(HuC:GCaMP5-G)a4598Tg* was used in this study [20]. The transgenic line was kept in either a TL or TLN (nacre) background. Zebrafish larvae were raised in E3 medium until day 5 or 6 post-fertilization (dpf).

Animal preparation

At the day of experiments (5 or 6 dpf), larvae were transferred into a petri dish and embedded in 1.6% low melting agarose (E3 medium). The agarose surrounding the eyes was not removed as to minimize the range of possible eye movements. Ten animals received an injection of α -bungarotoxin into the caudal vein to paralyze them and prevent eye movements and motion artifacts. Seven animals were recorded without paralysis (regarding the neuronal responses, we did not observe any differences between paralyzed and non-paralyzed animals and therefore we pooled the data from all fish). The animals were then transferred and mounted in agarose on a glass triangle and the fish head protruded the point of the glass triangle, so that the eyes could see through the (agarose and) water clearly. The volume of agarose surrounding the fish head was trimmed on the sides and in front of the animal in order to reduce the amount of agarose surrounding the eyes. However, the eyes were still covered by agarose to minimize the range of possible eye movements. The glass triangle was held from the back by a 5-mm-thin shaft which was fixed to an 8-cm-diameter glass bulb (made by a glass blower) filled with E3 medium. The glass bulb resembled a consumer market light bulb (threading of the light bulb/glass bulb shaft in the back of the fish), and a 5-cm-diameter hole was cut on the top of the spherical part to allow lowering the microscope objective towards the fish. From stimulus arena to the fish eye, the light traveled through air, glass (light hit glass roughly orthogonally in the spherical part as to minimize refraction of light rays), water, and finally agarose. The glass bulb was fixed with its shaft (15.5 mm diameter) to the metal holder, which allowed making adjustments in pitch and yaw (the glass shaft allowed for adjustments in roll). In the monocular direction selectivity experiments, the first batch of data ($n = 5$ larvae, included in the reported results) were acquired using a cylindrical plastic stage and container instead of the glass bulb container with glass triangle

stage. In the first batches of pretectal monocular direction selectivity experiments ($n = 5$ larvae), we noticed a problem with reflections on the transparent stage wall on the opposite side of stimulation (plastic cylinder), resulting in responsive neurons on the ipsilateral side of (intended) stimulation in the tectum. In the second set of recordings (monocular DS: $n = 4$ larvae), we exclusively used the glass bulb stage and wrapped a piece of black, half-cylindrical aluminum foil around the objective. The black aluminum foil was then lowered beyond the eye contralateral to the stimulus in order to prevent this eye from seeing the reflections. In these recordings, only very few ipsilateral tectal neurons were detected. The ipsilateral neurons from the first batch (with reflection issue) are depicted in a more transparent color in Fig. 1g, while the ipsilateral neurons from the second batch have normal colors in Fig. 1g. Both sets of recordings were included in data analysis, because only few additional neurons were detected due to the reflections in the ipsilateral tectum, suggesting that the vast majority of the detected neurons of the contralateral side were detected due to the stimulus presented to the intended eye.

Microscopy of somatic responses

Calcium imaging was performed with a two-photon microscopy setup based on the MOM microscope (Sutter Instruments, Novato, CA, USA) [41], using a Coherent Vision-S Ti-Sa laser and a $\times 20/1.0$ Zeiss objective to image calcium signals in the transgenic fish line *HuC:GCaMP5G* (*Tg(elavl3:GCaMP5G)^{a4598}*) [20]. Calcium time series were recorded at two frames per second, with an image size of 512×512 pixels and $\times 2$ magnification, at 920 nm, pre-pulse compensation set to 9756 fs^2 . The midbrain and diencephalon were sampled from $+60 \mu\text{m}$ below the landmark (posterior commissure) to $-80 \mu\text{m}$ above the landmark. Optical slices were taken every $10 \mu\text{m}$ (monocular direction selectivity) or $20 \mu\text{m}$ (binocular stimulation) in the dorsoventral direction in individual fish. Across individual fish, all dorsoventral positions were recorded in $10\text{-}\mu\text{m}$ increments relative to the landmark (i.e., no recording at e.g. 5 or $15 \mu\text{m}$ below the landmark). We recorded eight animals using the binocular stimulus protocol, which corresponded to four recorded composite brains (one optical slice per $10 \mu\text{m}$). Since we only recorded every $10 \mu\text{m}$ in dorsoventral extent for the monocular direction selectivity dataset, more than twice as many DS neurons should have been detectable in the respective brain areas (Fig. 1d), if we had sampled the brain areas at optimal spacing given the neuron soma diameter of ca. $5 \mu\text{m}$. Where specified, error bars correspond to measures per completely imaged brain volume. Care was taken to record the same number of slices in each anatomical region. Oftentimes, more than one animal was used to image one brain

volume completely. Due to the long recording times and positioning instability (likely resulting from the fish drifting within its agarose embedding), we corrected position drifts along the optical axis manually during the recording (mostly less than $4 \mu\text{m}$ per 30 min). Using the $\times 20$ objective and a magnification of $\times 2$, our spatial resolution was $0.43 \mu\text{m}/\text{pixel}$ on the x -axis (medial-lateral) and the y -axis (anterior-posterior).

LED arena for visual stimulation (Figs. 1 and 2)

Visual stimulation of zebrafish was conducted with a cylindrical LED arena consisting of 14,336 LEDs (Kingbright TA08-81CGKWA): 2 (arena halves) $\times 8$ (rows) $\times 14$ (columns) $\times 64$ (8×8 multiplexed LED matrix) LEDs. The caudal-most column of each arena half was left without LEDs (i.e., 14, not 15 columns), since the space was needed for the glass bulb stage metal holder. The arena covered -168° to $+168^\circ$ in azimuth and -40° to 40° in elevation. A few degrees in angle of the dorsal field of view were likely blocked by the objective due to its access angle of 38.39° ($< 40^\circ$); however, the eyes were located $\sim 200 \mu\text{m}$ below the objective focus which should have resulted in a maximal viewing angle exceeding 38.39° (i.e., 39.2°). In the binocular stimulation experiments, the nasal view was intentionally blocked from -18° to $+18^\circ$ azimuth to prevent the stimulus being visible to the non-intended eye. The LEDs emitted at 570 nm and an additional high-pass filter foil (LEE no. 779, article 595-1700-7790, castinfo.de, Hagen, Germany) and diffusion filter foil (LEE no. 252, article 595-1780-2520) were placed in front of the arena to optimize GCaMP signal detection and make the stimulus appear more homogeneous. This resulted in a yellow appearance of the stimulus. The LED arena was controlled as described previously [42, 43]. LEDs were only lit during fly-back time of the scanning mirrors. Due to the high repetition rate of the line scans ($\sim 1000 \text{ Hz}$), the stimulus was perceived as continuous (not flickering) by the fish.

Identification of regions of interest

For analysis of activity, a custom Matlab script (MOM_Load) identified regions based on their correlation to the stimulus (using a regressor that was active during motion stimuli and inactive otherwise) and ROIs were manually drawn as described previously [10, 44]. The 3D mapping of cell location was performed using custom written Matlab scripts (Midbrain Localizer and Cell Viewer), which allowed to register the two-dimensional recordings to a 3D z-stack which was acquired after recording sessions [10].

Since manual selection always comes with an inherent bias and potential confounds, we estimated the impact of the manual selection, on the monocular direction selectivity analysis and the binocular selectivity analysis, by

first manually assigning three categories to each ROI, either (1) single-cell ROI, (2) multiple-cell ROI, or (3) unclear ROI (Additional file 4: Figure S4A). The vast majority of ROIs corresponded to the “single-cell” class, likely a result of our careful drawing of ROIs using information from the median image time series to visualize the outline of the cells. With this classification, we repeated the binocular direction selectivity analysis (Additional file 4: Figure S4B–D). We only found very few ROIs for which the (complex) response types could have been explained by potential overlap of signals from two neurons. Furthermore, no evidence for signal mixing was apparent when we plotted the linear model R^2 and MB index values for the ROIs that corresponded to multiple cells (Additional file 7: Figure S7B, method see “[Binocular directional tuning](#)”). The distribution looked similar to the one for the single-cell ROIs (Additional file 7: Figure S7A), again supporting the validity of our manual ROI selection. Therefore, our post-hoc analysis suggests our manual ROI drawing only had minor impact on our conclusions.

To further test the potential impact and bias of the manual selection on binocular selectivity of the neurons, Pearson’s linear correlation coefficient between each pixel within a manually selected ROI and the average activity of the ROI for the binocular direction selectivity analysis data was calculated with Matlab. The histogram analyses of the average Pearson’s linear correlation coefficients from the identified monocular and binocular neurons or single-cell and multiple-cell ROIs were compared, respectively. The average correlation coefficient in binocular neurons was lower than that in monocular neurons (Additional file 7: Figure S7D). There are three possible explanations. First, monocular neurons are much more active with our stimulus protocol, while binocular neurons typically only show activities to one or a few stimulus phases, leading to a lower signal-to-noise level and pixel-wise correlation in these binocular neurons. Second, binocular-selective neurons (which correspond to a large fraction of the binocular neurons plotted in Additional file 7: Figure S7D) are defined by their selective responses: they do not fire in a pattern that resembles a superposition of two monocular-responsive neurons, but rather fire only when stimuli were presented to both eyes (for one particular stimulus phase). Therefore, it is quite unlikely that binocular-selective ROIs would erroneously result from monocular neuronal responses (but of course, the non-linearity of the calcium indicator needs to be considered). A third possible reason for the higher pixel-wise correlation values of monocular neurons could be that the monocular neurons are more frequent in the optic tectum, which is located superficially in the animal, resulting in a higher signal-to-noise ratio for tectal recordings. As expected, the

average correlation coefficient of isolated ROIs (single-cell ROI) was about the same as that of the potentially contaminated ROIs (multiple-cell ROI, Additional file 7: Figure S7E).

In addition, another analysis based on principal component analysis and clustering was performed (Additional file 8: Figure S8). To show the potential of the technique, we first used four ROIs identified as separate cells in the manual selection. Principal component analysis (PCA) and subsequent expectation maximization clustering were performed for all pixels of the four ROIs. To identify the optimal number of clusters, we used the Bayesian information criterion (BIC). We then used the clusters and can show that the method is well suited to separate non-correlated sources, even when they are in close proximity (Additional file 8: Figure S8A), because pixels from the same ROIs clustered together. The same technique was applied to find the optimal number of clusters (i.e., different neurons) in the ROI masks that were previously classified as most likely being composed of multiple sources (Additional file 8: Figure S8B). As the analyses described above already suggested, the resulting fluorescence pixel time series showed high correlation with each other for individual ROI masks (Additional file 8: Figure S8C), suggesting that the variability stems mostly from noise and not from separated sources that were erroneously assumed to be one cell.

3D anatomical mapping

To distinguish from tectal neurons, we proceeded as follows. For each fish, the whole z-stack—which was imaged from the top of tectum to deep ventral pretectum—was resliced to generate a transverse view in each image plane. On selected, regularly spaced transverse planes (more than ~ 50 planes), the ventral border of the tectum was drawn: on each of these transverse plane (512 pixels from left to right, x dimension), a curve was drawn through the area devoid of neuronal somata and fluorescence, which was ventrally adjacent to periventricular tectal area with densely packed, fluorescent somata. From each curve, 51 homogeneously distributed points were selected as key points with which a new boundary curve was generated by linear interpolation or three-term Gaussian fitting. Using this method, we obtained a boundary curve with 512 data points corresponding to the pixels in x/y dimensions (left-right and dorsal-ventral) for each transverse plane (Additional file 1: Figure S1A, curves in red color). In-between the annotated transverse planes, the 2D curves were interpolated to receive a surface that separated the tectum from the pretectum in all three dimensions.

Monocular directional tuning

We presented moving gratings in eight directions ($48^\circ/\text{s}$) to the right eye of the fish with one LED half-cylindrical arena. In order to control for possible adaptation of neural activities, we showed the visual stimuli in two different orders for different individual animals as depicted in Additional file 1: Figure S1B. All eight visual stimulus phases were repeated three times. A stationary grating (pause) was presented between motion phases, as illustrated in Additional file 1: Figure S1E. The spatial frequency of the visual stimuli was $0.033 \text{ cycles}/^\circ$. Each stimulus period started with a stationary grating (4 s), and then the motion stimulus phase (using the same, but moving grating) ensued for 4.8 s. After each motion phase, the stationary pattern was presented for 2 s (pause) and then the pattern was changed to the stationary grating of the next stimulus period (4 s). Tectal and pretectal identity was assigned to neurons based on the semi-automatically drawn anatomical border visible in the z-stack (see 3D anatomical mapping). Neurons below the tectum and more rostral than $140 \mu\text{m}$ caudal of the landmark (anterior edge of the posterior commissure, see Kubo et al. [10]) were considered as pretectal neurons and plotted in the histogram of preferred directions. Neurons located more caudally ($> 140 \mu\text{m}$ caudal to the landmark) potentially corresponded to premotor neurons (nMLF) and were therefore excluded from further analysis.

Motion phase-locked activity for individual neurons was calculated by a series of analysis steps. First, we calculated a DFF ($\Delta F/F$) trace from the raw fluorescence trace [$\text{DFF} = (F(t) - F_b)/F_b$, with F_b corresponding to the baseline fluorescence]. Then, we filtered the DFF fluorescence traces with a low pass wavelet decomposition [type Daubechies, Matlab: `wavedec (DFF,1,'db4')`] and a sliding median filter (the median of three data points). Then, deconvolution was performed on the filtered data with the decay time constant (τ) of GCaMP5G, 1.5 s. We calculated the mean of phase-averaged signal (MPAS; averaged over stimulus phase time) from the deconvolved traces. The baseline was defined as the MPAS of all the non-stimulus phases (i.e., without moving stimulus). The standard deviation (STD) of all phase-averaged signals was calculated for the non-motion phases. And the z-score was calculated using the equation [$\text{z-score} = (\text{MPAS} - \text{mean}(\text{baseline}))/\text{STD}(\text{baseline})$]. We then calculated the median MPAS z-score (i.e., the median across the three repetitions of a stimulus phase of the average of all data points within one stimulus phase).

The tuning curve of the calcium signal z-score from eight directions was fitted with one or two von-Mises distributions (Matlab function 1: $A/(2\pi \times \text{besseli}(0, \kappa)) \times \exp(\kappa \times \cos(X - \text{PD})) + \text{baseline}$, function 2: $A1/(2\pi \times \text{besseli}(0, \kappa)) \times \exp(\kappa \times \cos(X - \text{PO})) + A2/(2\pi \times \text{besseli}(0, \kappa)) \times \exp(\kappa \times \cos(X - \text{PO} - \pi)) + \text{baseline}$). In

the well fitted data ($R^2 > 0.8$), the preferred direction (PD), the response (R_{pref}) in the PD, and the opposite direction (R_{opp}) were calculated from the fitting with one von-Mises distribution. Similarly, we calculated the preferred orientation (PO) of the motion (not the grating), the response in the PO (R_{ori}) and the orthogonal orientation (R_{orth}) from the fitting with the sum of two von-Mises distributions which had peaks separated by 180° . The DSI and OSI were calculated as: $\text{DSI} = (R_{\text{pref}} - R_{\text{opp}})/(R_{\text{pref}} + R_{\text{opp}})$ and $\text{OSI} = (R_{\text{ori}} - R_{\text{orth}})/(R_{\text{ori}} + R_{\text{orth}})$. The neurons with DSI larger than the threshold; 0.7 were considered as direction selective. The following criteria were used to define orientation-selective neurons: $\text{OSI} > 0.5$ and $\text{DSI} < 0.7$. In the histogram analysis of the PDs for tectal and pretectal neurons, 6° was used as the bin width. We identified the peaks of the PDs via fitting the histogram data with the sum of four von-Mises distributions (plus a baseline summand). For each of the four peaks i , the summand took the following form: $a_i \times \exp(\kappa \times \cos(X - \text{Peak}_i))/(2\pi \times \text{besseli}(0, \kappa_i))$.

The agarose embedding resulted in a slightly variable pitch orientation of the body across animals. The magnitude of the pitch rotation was between 1° and 10° for each animal. Pitch correction of the PD values did not result in sharper tuning curves. We present the PD data with pitch correction for body positions here. Note that we did not measure torsional eye positions and it is therefore possible that eyes had different pitch positions relative to the body.

To calculate the laterality index, we took the number of cells contralateral to the stimulated eye and subtracted the number of ipsilaterally located neurons and divided the result by the sum of neurons in both hemispheres. This resulted in an index running from 1 (all contralateral) to -1 (all ipsilateral).

Binocular directional tuning

In the binocular DS experiments, moving bars or rotating radial patterns, at the velocity of $15^\circ/\text{s}$, were used as visual stimuli. The spatial frequency was $0.067 \text{ cycles}/^\circ$. We showed 3 repetitions of the 64 combinatory stimulus phases using two half-cylindrical stimulus arenas. The combinations were shown in a pseudo-randomized order, as illustrated in the Additional file 1: Figure S1E (in the diagonal direction shown by the numbers and the first few phases are indicated by red arrows). Patterns from both arenas were changed during the pause phase to temporally separate the possibly occurring calcium responses to a changed static stimulus from the motion-sensitive calcium responses we were interested in. In each trial, every stimulus phase lasted 4.8 s, followed by a 6 s pause. During the first 2 s of the pause, the stimulus combination remained on the arenas and for the remaining 4 s the next stimulus combination was

presented motionlessly. The repetitions were separated by 9-s long pauses. In a pilot experiment, we recorded neural activity in two animals with a stimulus protocol consisting of 12×8 instead of 8×8 stimulus phases. In the additional phases, one of the eyes was stimulated with $45^\circ/135^\circ/225^\circ/315^\circ$ oblique motion directions. We only found very few neurons that preferred binocular stimulus combinations including oblique motion or had specifically suppressed activity during oblique motion. This result indicated that oblique directions apparently do not play a major role in binocular optic flow representations, which was in agreement with our results from monocular stimulations. We therefore decided to omit the oblique stimulus phases in the stimulus protocol used to acquire the data presented here.

Tectal or pretectal identity was assigned to neurons based on the semi-automatically drawn anatomical border visible in the z-stack (see section on “3D anatomical mapping”). Neurons below the tectum that were not located in the brain volumes corresponding to nMLF, vEMN, and dVEMN (see gray brain volumes in Fig. 1g) were considered as pretectal neurons and included in further analysis, while the neurons from (pre-) motor brain volumes were excluded.

To analyze the directional tuning of neurons, we reduced the complexity by using a binary response type (RT) classification [9, 10]. To do this, we compared the average inter-stimulus interval before every stimulus phase with the median averaged activity in the stimulus phase. If the mean $\Delta F/F$ during the stimulation exceeded $3 \times \text{STD}$ over its local baseline, it was assigned a 1, otherwise a 0. This method was applied to all stimulus phases ($7 \times 7 + 1$), excluding stimulus phases that included a blank screen on one of the half cylinders. We excluded these 14 ($7 + 7$) phases after noticing that the reflections of about 4% of the light on the inside of the opposite glass bulb wall (theoretically to be expected, see Fresnel equations) were visible to the fish eye which should have received a black stimulus during this stimulation phase. In the calcium imaging data, we could clearly see that many (but not all) neurons responded to the motion of the reflected stimulus as well. Since the activity during these 14 stimulus phases was therefore contaminated, we decided to remove those phases from further analysis. In all other phases (except the black-black phase), a bright stimulus was presented on both halves of the arena so that the reflection was likely hard to see for the animal and did not confound the analysis of the rest of the data. A potential caveat of the binary classification of motion phases in active and inactive is that the selectivity of cells depends on the chosen threshold. A low threshold will introduce noise to the binary classification, while a high threshold will lead to increased “selectivity” of cells that might still

respond to other stimulation phases, but whose responses do not reach the threshold to be classified as active. In order to confirm the validity of the chosen threshold, we performed an additional analysis, in which a lower ($2.5 \times \text{STD} + \text{mean}$) and a higher ($3.5 \times \text{STD} + \text{mean}$) threshold were used. This analysis returned similar results as that of using the $3 \times \text{STD}$ threshold and therefore suggests that our chosen threshold value is an acceptable threshold, which did not strongly bias response types to getting classified as binocular selective or monocular responsive (Additional file 6: Figure S6).

Additionally, we calculated the “MB index,” a metric that depends on the fit of measured activity to a linear model consisting of purely monocular responses (Fig. 2d and Additional file 1: Figure S1F). To examine how well the neuronal responses can be explained by monocular direction-selective excitatory input, we fitted a linear model to the data recorded with the binocular stimulus protocol and calculated the goodness of fit R^2 value. The coefficients of the model were used to calculate the monocular-binocular index (MB index) for each neuron. The function consists of 14 summands, each a product of a weight (α for columns, β for rows) and a 7×7 matrix consisting of one column or row with ones (C and R in the depicted linear model equation). The neural activity (z-scores) of a given neuron during the 7×7 stimulus phases (i.e., 49 z-score values) is then fitted to the equation to identify how well the neuronal responses can be explained by monocular direction-selective excitatory input, which should always activate a whole row or column. To calculate the MB index, we took the difference between the sum of all row coefficients and the sum of all column coefficients and divided it by the sum of all coefficients for normalization. A value close to 1 or -1 corresponds to mainly monocularly driven neurons, while a value of 0 corresponds to binocularly driven neurons. The expectation would be that cells whose activity can be explained by input from excitatory DS-RGCs in the absence of inhibition (e.g., monocularly driven simple cells) would have a high R^2 value and additionally a high (absolute) MB index value, since they should be active only in one row or column of the 7×7 matrix (i.e., their activity depends on the stimuli presented to a single eye, while the other eye’s stimulus does not affect activity). The activity of many neurons could not be explained by this simple linear regression model, while the model worked well for monocular neurons. This difference indicates that the activity of the former neurons strongly depended on the combination of binocular phases, i.e., these neurons performed binocular computations. Note, that the “MB index” analysis of response profiles did not depend on thresholds or classifications and still assessed whether the activity of a neuron in question can be explained by input from DS-RGCs alone or shows evidence of binocular inhibitory

computations. The MB index helps to visualize the grade of binocular response selectivity and binocular drive. Low values of the goodness of fit to a linear model (R^2) on the x -axis in the scatter plot (Additional file 1: Figure S1G) correspond to neurons with binocular selectivity. High values can be interpreted as neural responses without suppressed activity during particular binocular phases. In the case of TN, up, NT, and down (but not pitch) responses, neurons with high R^2 can be fully explained by simple excitatory input from DS-RGCs (monocular and binocular simple responses). The MB index is plotted on the y -axis in Additional file 1: Figure S1G. Red points correspond to cells shown in Fig. 2d.

We subdivided all further analysis to reduce the theoretical complexity of response types (RTs), which is given by 2^{49} possible RT combinations and the receptive field (RF) locations of neurons. Our Pitch stimuli were different from the remaining motion phases in that the motion directions differed wildly across the surface of the stimulus arena. Since we did not know the RF locations in these experiments, it was difficult to interpret the neuronal activity observed during Pitch stimulation. For example, a neuron that is responding to Up in the right eye and also to Pitch-Up could be non-specific for Pitch and simply have a relatively small RF in the nasal visual field at the level of the equator. However, it is also possible that this neuron could have a large receptive field and a complex selectivity for RE Up and RE Pitch-Up. Without proper knowledge about the RF locations, in an RT classification based on all 2^{49} possible RTs, the mere locations of (small) RFs will already result in several different found response types (combinations of Pitch responses with other motion responses). Furthermore, the limited recording time prohibited a combination of RF mapping and binocular directional selectivity analysis of a sufficiently high number of animals and recordings to identify all such response types at a sufficient frequency. We therefore analyzed Pitch responses separately from the other stimulation phases. We selected the five phases of each eye corresponding to stationary (ST), temporal-to-nasal (TN), Up, nasal-to-temporal (NT), and Down, leading to a total of 25 stimulation phases. Based on these 25 phases we then classified neurons, which had the same binary response type. The same analysis was applied to stationary and pitch stimulation phases alone. Pitch and stationary phase RTs were further sub-selected to exclude overlap with the 5×5 analysis (i.e., not active during the 5×5 phases for the pitch analysis and not active during the 6×6 motion phases for the stationary analysis). The resulting RTs were then classified as either frequent (≥ 3 cells) or infrequent RTs (≤ 2 cells).

While 39% of the neurons contributed to the group of the frequent response types, for the large number of infrequent response types, only one or two neurons were

identified. It was unclear whether these neurons just had noisy response profiles and thereby largely resembled the more frequent response types, or whether these neurons showed a very special responsiveness. To estimate the potential variability and the possibility of missing important RTs, we calculated the distance of infrequent to frequent RTs by first identifying the most similar frequent RT to an infrequent response based on the difference in the binary RT profile from the 5×5 analysis (Additional file 1: Figure S1H) for each neuron. For this purpose, we calculated the correlation of its response profile (5×5 z-score heat map as in Fig. 2d) with the median response profile of the best matching response type from the frequent group (red line). We used Pearson correlation of the median $\Delta F/F$ response of all neurons within the best-fitting frequent RT with the $\Delta F/F$ response of the infrequent response type in question. We further calculated the correlation of the individual responses of neurons in a frequent RT group with its own RT median response (blue line in Additional file 1: Figure S1H). As a control, we calculated the correlation of each neuronal response to a randomly selected existing RT (random choice of an existing RT response, drawn from a distribution accounting for the frequency of each RT). We then plotted the cumulative sum of neurons for each of the three analyses (individual frequent RT vs. RT median, infrequent individual RT vs. most similar RT median, any neuron vs. random RT median) versus the achieved Pearson correlation (Additional file 1: Figure S1H). This analysis was performed to show the validity of the approach and the assignment of binary RTs. Note that the responses of the neurons from the infrequent group were mostly very similar to one of the more frequent response types, suggesting that the computational repertoire (in the context of the employed stimulus phases) is well described by the first 49 most frequent response types.

The binocular-selective response types presented in Fig. 2 are only active during one particular stimulus phase (a combination of two motion directions in the left and right eye, respectively) and silent during all other stimulus phases. These neurons clearly show the needed selectivity to detect a particular type of optic flow, e.g., to distinguish rotational from translational optic flow. However, other neurons that are active during two or more stimulus phases can still be somewhat binocular selective for certain directions (and maybe not selective for certain other directions). In order to characterize the existence of selectivity in single neurons that is suited to distinguish rotation from translation in the same plane of motion (e.g., forward versus clockwise for stimuli moving in the horizontal plane), we devised a “phase pair analysis” (Additional file 2: Figure S2). We compared responses to 18 different stimulus phase pairs (BW-CC, FW-CC,

FW-BW, CW-CC, CW-BW, CW-FW, RCC-TD, RCW-TD, RCW-RCC, TU-TD, TU-RCC, TU-RCW, PU-AP2, PD-AP2, PD-PU, AP1-AP2, AP1-PU, AP1-PD; forward, FW; backward, BW; clockwise, CW; counter-clockwise, CC; roll clockwise, RCW; roll counterclockwise, RCC; translation up, TU; translation down, TD; pitch up, PU; pitch down, PD; antagonistic pitch directions 1 (PiUp-PiDo), AP1; antagonistic pitch directions 2 (PiDo-PiUp), AP2.) and classified neuronal responses to phase pairs in four different categories (1–1, 1–0, 0–1, 0–0). If cells are generally able to distinguish between these different types of motion (rotation vs. translation), the expectation would be that we have an over-proportionally large number of 0–1 or 1–0 classifications. For instance, with our visual stimuli, motion could occur in the horizontal plane, transversal plane or sagittal plane (stimulus phase fields without filled text in Additional file 2: Figure S2A correspond to optic flow combinations that should not occur frequently in nature and have therefore not been analyzed here). For each kind of motion in the three planes, there are four stimulus phases. The six possibilities of combining two of these four phases for the horizontal plane of motion are depicted in Additional file 2: Figure S2A. For each of the $3 \times 6 = 18$ possible stimulus phase pairs, there are four possible response types for each neuron, which are illustrated for the possible stimulus phase pair CW-FW: active during both stimulus phases (1:1), selective for phase 1 or selective for phase 2 (1:0, and 0:1), or the neuron can remain silent during these two stimulus phases (0:0). We analyzed the responses of all 591 motion-sensitive neurons for the presence of super-threshold activity in the 3×4 stimulus phases of interest and calculated how frequent the four different phase pair responses were for each of the $3 \times 6 = 18$ stimulus phase pairs in question. Every neuron contributes a count of 1 to just one out of the possible four binary combinations (1:1, 1:0, 0:1, 0:0), according to its active/silent status for the stimulus phase pair in question. The *y*-axis in Additional file 2: Figure S2A is labeled “number of observations” and not “number of neurons,” because we analyzed the responses of all 591 neurons for each of the 18 phase pair combinations. Since virtually all neurons were only active for a small fraction of the 64 stimulus phases from the original stimulus protocol, the (0:0) phase pair responses are very frequent. The monocular, simple neurons should be responsible for many of the observed (1:1) phase pair responses. The (1:0) and (0:1) phase pair responses can be inspected in this plot to judge how selective the neurons were for particular types of optic flow directions. For example, selective responses to rotation (CW, CCW) appeared to be less frequent than responses to translation (FW, BW) in the horizontal plane (Additional file 2:

Figure S2B). We performed a bootstrap analysis to verify which of the selectivities were significantly over- or underrepresented than the chance level. For each motion plane, we calculated the percentage of neurons that responded during 0, 1, 2, 3, or 4 stimulus phases out of the available four binocular stimulus phases. We then simulated response types of 591 neurons by drawing the number of active stimulus phases (0 to 4) for each simulated neuron and randomly specifying which of the four phases are active. This was done for each plane of motion separately and 25000 simulated datasets of 591 neurons were generated. The simulated data was then processed in the phase pair analysis as described above. The percentage of datasets, in which a higher or lower number of neurons was found for each of the bars, was determined in order to achieve a one-tailed *p* value (bootstrapping, alpha = 0.05) and the results are plotted (Additional file 2: Figure S2C). To account for multiple comparisons, we also performed Bonferroni correction, which led to a threshold of < 0.00069 equalling 17 or fewer than 17 events (Additional file 2: Figure S2D).

Inclusion criteria for somatic calcium responses

We calculated the Pearson linear correlation coefficients between the stimulus phase *z*-scores (see above) of the three stimulus protocol repetitions (for all three pairwise combinations) to characterize the reproducibility of stimulus-evoked calcium responses. In our further data analysis, we only kept the neurons for which all three correlation coefficients were higher than a certain threshold. The threshold was set between 0.7 and 0.8 to exclude around 20% neurons with low reproducibility of stimulus-evoked activity in the monocular direction selectivity experiment (2556 out of 3271, 78% neurons were kept). The thresholds for the binocular direction selectivity experiments were relatively lower, ranging from 0.65 to 0.75, due to the long experimental protocols and the low fraction of stimulus phases that a neuron was responsive to. Only 64% (853 out of 1325) neurons were kept for further analysis in the binocular direction selectivity experiments. We then performed signal-to-noise ratio (SNR) analysis to exclude neurons with unstable baseline. In the SNR analysis, a threshold of four was used on the *z*-score to detect positive neural responses. Signal-to-noise ratio (SNR) was defined as the ratio of the average response of all the responsive phases to the standard deviation of the baseline. All the neurons with SNR lower than a certain threshold were excluded. The threshold was set between 8 and 10 to exclude about 10% remaining neurons with SNR in the monocular direction selectivity experiment (2290 out of 2556, 90% neurons were kept). We kept about 90% (763 out of 853) neurons in the binocular direction selectivity experiments for further analysis.

Analysis of the data from Naumann et al.

The data used for the pretectal forward/backward and sideward selectivity analysis were kindly provided by Florian Engert and Eva Naumann. The file contained (alongside with other information) repetition-averaged calcium responses for each neuron. Each stimulus phase response consisted of 64 data points each (including 19 data points before onset of motion, 3 data points per second). In addition, the file included the assigned binary classification (response type). We analyzed the neurons which had been stimulated with all 10 relevant stimuli (1672 pretectal neurons out of the 3070 neurons from Fig. 5B in their study). The DFF fluorescence traces were filtered with a low pass wavelet decomposition using a custom script [type Daubechies, Matlab: `wavedec(DFF,1,'db4')`]. The resulting traces were filtered again using a sliding median filter (the median of three data points). Then, the filtered data were deconvolved with the decay time constant (τ) of GCaMP5G, 1.5 s. The mean of stimulus phase-averaged signal calculated from the deconvolved traces was compared with an arbitrary threshold, the $1.0 \times \text{STD}$ above the baseline of the deconvolved traces. To ensure that the chosen threshold reflects the underlying selectivity of neurons, we performed the same analysis with three different thresholds ($1.0 \times \text{STD}$, $1.8 \times \text{STD}$, and $3 \times \text{STD} + \text{mean}$) and found that all major conclusions were still supported, irrespective of the chosen threshold (Additional file 6: Figure S6). The baseline was determined by taking the time periods without motion stimulus for each cell and calculating the mean of the response during each pause. The standard deviation was then calculated by taking the standard deviation of these mean values across stimulus pauses for each neuron. The value “1” was assigned to a stimulus phase when the mean value was larger than the threshold. Otherwise, the stimulus phase was assigned as the value “0.” In our analysis, all ten different stimulus phases, including the forward and backward motions were considered and theoretically 1024 (2^{10}) different response combination classes could have been detected.

Quantification and statistical analysis

The statistical information is provided in each of the sections above.

After obtaining the raw data (pixel calcium signal time series), the data was quantified, anatomically registered, and statistically analyzed according to the descriptions given in the above sections entitled “[Identification of regions of interest](#)”, “[Monocular directional tuning](#)”, “[Binocular directional tuning](#)”, and “[Analysis of the data from Naumann et al.](#)”.

The analyzed number of zebrafish and brains is indicated in the main text and figure legends. Error bars correspond to SEM unless stated otherwise.

Additional files

Additional file 1: Figure S1. (related to Figs. 1 and 2). Experimental parameters and auxiliary analyses. (A) Defining the tectal-pretectal boundary. Each image is a transverse view and the number indicates the pixel position (1 pixel = $0.43 \mu\text{m}$ in the anterior-posterior direction). D, dorsal; V, ventral; R, right; L, left. (B) Monocular stimulus protocols to map preferred directions. Left: motion directions; Right: Temporal sequence (rightwards) of the two stimulus protocols used in different recordings. A, anterior; P, posterior. (C) Histogram of direction selectivity from all recorded motion-sensitive cells. (D) Histogram of the normalized vector sum of DS neurons ($n = 9$ brains, pretectum and tectum combined in (C) and (D)). (E) Stimulus protocol for the binocular direction selectivity experiment. Top: 8×8 unique stimulation phases were presented in the indicated order and repeated three times in the protocol. Bottom: Schematic of two individual stimulus periods. (F) Linear model equation used to assess functional properties of binocular optic flow processing (see “Materials and methods”). (G) Linear model analysis. Monocular neurons (with high absolute MB index) tended to be fit very well by the linear sum model, while more binocularly driven neurons (MB index close to 0) were not fit well. This suggests that binocularly driven neurons are often suppressed during particular stimulus phases, but not for other stimulus phases in the same row or column, thus establishing binocular response selectivity. (H) Analysis of the similarity of infrequent responses to the more frequent response types found in Fig. 2e. The red and blue lines show the cumulative distributions of the correlations of neurons from the infrequent group with the best matching frequent response type and correlations of neurons from the frequent group with their response type, respectively. The yellow line shows the correlation of the neuronal responses with a randomly selected, existing response type (shuffled). (JPG 10220 kb)

Additional file 2: Figure S2. (related to Fig. 2). Analysis of stimulus phase pairs for horizontal, transversal and sagittal planes of motion. (A) *Left:* possible binocular combinations of motion in the horizontal plane (gray text), transversal plane (orange), or sagittal plane (blue). *Middle:* For each kind of motion in the 3 planes, there are 4 stimulus phases. The 6 pair combinations of these phases are depicted for the motion in the horizontal plane. *Right:* For each of the $3 \times 6 = 18$ possible stimulus phase pairs, there are 4 possible response types for each neuron, which are illustrated for the possible stimulus phase pair CW-FW: active during both stimulus phases (1:1), selective for phase 1 or selective for phase 2 (1:0, and 0:1), or silent (0:0). (B) Phase pair responses across all 591 motion-sensitive neurons. The monocular, simple neurons should be responsible for many of the observed (1:1) phase pair responses. The (1:0) and (0:1) phase pair responses can be inspected in this plot to judge how selective the neurons were for particular types of optic flow directions, e.g., selective responses to rotation (CW, CCW) appeared to be less frequent than responses to translation (FW, BW) in the horizontal plane (compare the cyan and green bar heights). (C) Bootstrap analysis. “Higher” in red color denotes response types which were found significantly more frequently in the zebrafish brain than expected by chance in the shuffled dataset. (D) Same analysis as in (C), but using a two-tailed p value and Bonferroni correction for multiple tests ($n = 72$). The FW-selective responses were significantly more frequent than CC-selective responses for the FW-CC phase pair in column 2. For many phase pairs consisting of antagonistic directions, a significantly lower number of neurons with non-direction-selective 1:1 responses was identified (RCW-RCC, TU-TD, PD-PU), when compared to the shuffled data. (JPG 5187 kb)

Additional file 3: Figure S3. (related to Fig. 3). Analysis of pretectal response types (forward/backward and sideward). (A) Average response profiles of the eight most frequent response types (*Top*) and their (rightward-responding) mirror-symmetrical response types (*Bottom*). Except for FW and BW response types, for which no mirror-symmetrical response types exist, neuron numbers on the left correspond to the sums of the response type pairs active during leftward motion and their mirror-symmetrical counterpart. Numbers on the right correspond to the individual (non-merged) response types. (JPG 2301 kb)

Additional file 4: Figure S4. (related to Fig. 2). The manually drawn ROIs correspond to single neurons in most cases in the binocular stimulation dataset. (A) Examples of the manually drawn ROIs from the

binocular direction selectivity analysis experiment. Single-cell ROIs (90% of all ROIs), multiple-cell ROIs (7%) and unclear ROIs (3%) are shown in three rows. For each example ROI, the left plot shows the manually selected ROI (in red) on the median fluorescence of the calcium signal time series. The z-score heat map is shown on the right plot. The warm color and blue color (from red to yellow, the correlation coefficient decreases) indicate the region where the fluorescence is correlated or reverse-correlated with the motion-stationary regressor (see Methods). The numbers in black indicated the neuron ID when we analyzed the data. (B) Binary response type analysis of the single-cell ROIs. The number of ROIs (in pretectum and tectum, $n = 8$ animals, 4 composite brains, see “Materials and methods”) corresponding to single-cell ROIs is plotted versus the ~ 34 million (2^{25}) theoretically possible binary response types. The color code corresponds to monocular (green) and binocular selective neurons (magenta: selective for a single binocular motion stimulus, gray: selective for a single binocular stimulus containing motion on one side and a stationary grating on the other side; light blue: indistinct binocular response types). The first 34 frequent response types are illustrated below. Yellow, responsive phases; Blue, non-responsive phases. (C) Binary response type analysis of the multiple-cell ROIs, similar to (A). (D) Binary response type analysis of the unclear ROIs, similar to (A). (JPG 7743 kb)

Additional file 5: Figure S5. (related to Fig. 2). Binary response type analysis with different thresholds. (A) Response type analysis using 10 different thresholds. While the median number of identified neurons per response type is affected by the choice of threshold, the number of identified binocular-selective and monocular response types is only mildly affected by threshold choice. (B) A lower threshold of $2.5 \times \text{STD} + \text{mean}$ was used. (C) Analysis for the original threshold of $3 \times \text{STD} + \text{mean}$. (D) Analysis using a higher threshold of $3.5 \times \text{STD} + \text{mean}$. STD and mean correspond to the standard deviation and mean of the calcium signal $\Delta F/F$ during the stationary phases (related to Fig. 2e). (JPG 7371 kb)

Additional file 6: Figure S6. (related to Fig. 3). Effect of changing the activity threshold on identified response profiles of the neurons from the data of Naumann et al. Response profiles of the eight most frequent response types are illustrated in (A, B) using different thresholds. The visual stimulus-evoked calcium signals were detected with thresholds, $1 \times \text{STD} + \text{mean}$ (A), $1.8 \times \text{STD} + \text{mean}$ (B) and $3 \times \text{STD} + \text{mean}$ (C). In this study we used a threshold of $1 \times \text{STD}$, while the previous study used $1.8 \times \text{STD}$. Except for FW and BW response types, in each panel, the indicated neuron numbers on the left side of the plot correspond to the sums of the response type pairs active during leftward and rightward motion. On the right side of the plot, the numbers indicated the neuron numbers of each individual response type (i.e., without mirror-symmetrical response type). The mirror-symmetrical response type pairs were plotted separately on the upper and lower panel. The proportions of the forward-, backward-, and sideward-selective neurons are indicated on the right of each panel. STD, standard deviation of the calcium signal $\Delta F/F$ during the stationary phases; mean, mean of the calcium signal $\Delta F/F$ during the stationary phases. The icons and colors are identical to those in Fig. 3. (JPG 6249 kb)

Additional file 7: Figure S7. (Related to Fig. 2). Pixel-wise correlation analysis suggests that manually drawn ROIs correspond to single neurons in most cases in the binocular stimulation dataset. (A–C) Linear model analysis of the binocular experiment data for the single-cell ROIs (A), multiple-cell ROIs (B) and unclear ROIs (C) (related to Additional file 1: Figure S1G). (D) Histogram of average ROI correlation coefficients for the correlation between a given ROI's pixel time series and the average fluorescence time series of this ROI, for single-cell ROIs from the 49 frequent response types (left, original plot; right, normalized plot). Blue, binocular neurons (binocular selective or indistinct neurons); pale red, monocular neurons. (E) histogram analysis of the correlation coefficients of the pixel time series to the average fluorescence of single-cell ROIs and multiple-cell ROIs from the 49 frequent response types (left, original plot; right, normalized plot). (JPG 5536 kb)

Additional file 8: Figure S8. (Related to Fig. 2). Clustering of local pixel correlations reveals highly correlated activity patterns for cells that were classified as multiple ROIs. (A) Examples demonstrating the effectiveness of the method. Four ROIs that were manually identified to be single cells (their activity traces are shown on the right) were combined and each pixel of these ROIs was correlated with each other. Subsequently, we

performed principal component analysis (PCA) and expectation maximization clustering, which automatically segmented even spatially close neurons as independent units. Pixels were plotted according to the first two principal components (PCs) at the bottom, illustrating that the developed algorithm (PCA and clustering) successfully identified the correspondence of the pixels to their original ROIs (lower left: color code based on manual ROI selection, lower right: color code based on assigned cluster identity). (B) Example cluster analysis showing a potential “multiple-cell” ROI (see manual analysis in Additional file 7: Figure S7) that was split into three separate clusters by the algorithm (left); and the accompanying activity traces for each cluster (shown on the right). (C) Example cluster analysis showing an ROI that wasn't split, and its corresponding activity trace. (D) Quantification of the average correlation of the mean ROI traces resulting from the clustering (e.g., average correlation of the three traces shown in (B)). Correlation is overall high, suggesting that there is no major signal contamination even for neurons that were manually assigned to potentially contain multiple-cell activity. (JPG 2823 kb)

Acknowledgements

We thank Eva Naumann and Florian Engert for sharing their data (pretectal calcium responses induced by motion of 10 combinations), Alexander Borst for providing the LED panel board design, Thomas Nieß (glassblower shop) and Klaus Vollmer (fine mechanics workshop) for technical support, and Prudenter-Agas (Hamburg, Germany) for generating illustrations. Christian Brysch, António Miguel Fernandes, Marco Dal Maschio, Johannes Larsch, Julianne Skinner, Fumi Kubo, and Herwig Baier for feedback on the manuscript.

Funding

This work was funded by the Deutsche Forschungsgemeinschaft (DFG) grants EXC307 (GIN – Werner Reichardt Centre for Integrative Neuroscience) and INST 37/967–1 FUGG, and a Human Frontier Science Program (HFSP) Young Investigator Grant RGY0079.

Availability of data and materials

The processed data and associated Matlab codes, 8 example original datasets and two Matlab scripts for the analysis are available as a GIN repository, at https://web.gin.g-node.org/Arrenberg_Lab/Directional_selectivity_data. The raw datasets and software will be made available upon request.

Authors' contributions

ABA conceived the experiments and associated analysis protocols. KW performed the experiments and analyzed the monocular direction selectivity. KW and JH analyzed the binocular direction selectivity. JH implemented the linear sum model analysis. KW and ABA analyzed the data provided by Naumann et al. VH and DFR helped to set up the LED arena experiments. KW, JH, and ABA wrote the manuscript. All authors commented on the manuscript. All authors read and approved the final manuscript.

Ethics approval and consent to participate

The animal experiments were licensed by the local authorities (Regierungspräsidium Tübingen) in accordance with German federal law and Baden-Württemberg state law.

Competing interests

All authors declare that they have no competing interests.

Publisher's Note

Springer Nature remains neutral with regard to jurisdictional claims in published maps and institutional affiliations.

Author details

¹Werner Reichardt Centre for Integrative Neuroscience, Institute of Neurobiology, University of Tübingen, 72076 Tübingen, Germany. ²Graduate Training Centre for Neuroscience, University of Tübingen, 72076 Tübingen, Germany. ³Present address: Friedrich Miescher Institute for Biomedical Research, 4058 Basel, Switzerland. ⁴Neurobiology and Behavior, Institute of Biology 1, Faculty of Biology, University of Freiburg, 79104 Freiburg, Germany.

Received: 25 November 2018 Accepted: 13 March 2019

Published online: 29 March 2019

References

- Masseck OA, Hoffmann KP. Comparative neurobiology of the optokinetic reflex. *Ann N Y Acad Sci.* 2009;1164:430–9.
- Orger MB, Gahtan E, Muto A, Page-McCaw P, Smear MC, Baier H. Behavioral screening assays in zebrafish. *Methods Cell Biol.* 2004;77:53–68.
- Maaswinkel H, Li L. Spatio-temporal frequency characteristics of the optomotor response in zebrafish. *Vis Res.* 2003;43(1):21–30.
- Busch C, Borst A, Mauss AS. Bi-directional control of walking behavior by horizontal optic flow sensors. *Curr Biol.* 2018;28(24):4037–45 e5.
- Ibbotson MR, Hung YS, Meffin H, Boeddeker N, Srinivasan MV. Neural basis of forward flight control and landing in honeybees. *Sci Rep.* 2017;7(1):14591.
- Kretschmer F, Tariq M, Chatila W, Wu B, Badea TC. Comparison of optomotor and optokinetic reflexes in mice. *J Neurophysiol.* 2017;118(1):300–16.
- Cazin L, Precht W, Lannou J. Pathways mediating optokinetic responses of vestibular nucleus neurons in the rat. *Pflugers Arch.* 1980;384(1):19–29.
- Schiff D, Cohen B, Raphan T. Nystagmus induced by stimulation of the nucleus of the optic tract in the monkey. *Exp Brain Res.* 1988;70(1):1–14.
- Naumann EA, Fitzgerald JE, Dunn TW, Rihel J, Sompolinsky H, Engert F. From whole-brain data to functional circuit models: the zebrafish optomotor response. *Cell.* 2016;167(4):947–60. e20
- Kubo F, Hablitzel B, Dal Maschio M, Driever W, Baier H, Arrenberg AB. Functional architecture of an optic flow-responsive area that drives horizontal eye movements in zebrafish. *Neuron.* 2014;81(6):1344–59.
- Gahtan E, Tanger P, Baier H. Visual prey capture in larval zebrafish is controlled by identified reticulospinal neurons downstream of the tectum. *J Neurosci.* 2005;25(40):9294–303.
- Gabriel JP, Trivedi CA, Maurer CM, Ryu S, Bollmann JH. Layer-specific targeting of direction-selective neurons in the zebrafish optic tectum. *Neuron.* 2012;76(6):1147–60.
- Abbas F, Triplett MA, Goodhill GJ, Meyer MP. A three-layer network model of direction selective circuits in the optic tectum. *Front Neural Circuits.* 2017;11:88.
- Hunter PR, Lowe AS, Thompson ID, Meyer MP. Emergent properties of the optic tectum revealed by population analysis of direction and orientation selectivity. *J Neurosci.* 2013;33(35):13940–5.
- Lowe AS, Nikolaou N, Hunter PR, Thompson ID, Meyer MP. A systems-based dissection of retinal inputs to the zebrafish tectum reveals different rules for different functional classes during development. *J Neurosci.* 2013;33(35):13946–56.
- Simpson JJ, Leonard CS, Soodak RE. The accessory optic system. Analyzer of self-motion. *Ann N Y Acad Sci.* 1988;545:170–9.
- Crowder NA, Wylie DR. Responses of optokinetic neurons in the pretectum and accessory optic system of the pigeon to large-field plaids. *J Comp Physiol A Neuroethol Sens Neural Behav Physiol.* 2002;188(2):109–19.
- Cochran SL, Dieringer N, Precht W. Basic optokinetic-ocular reflex pathways in the frog. *J Neurosci.* 1984;4(1):43–57.
- Masseck OA, Hoffmann KP. Responses to moving visual stimuli in pretectal neurons of the small-spotted dogfish (*Scyliorhinus canicula*). *J Neurophysiol.* 2008;99(1):200–7.
- Ahrens MB, Orger MB, Robson DN, Li JM, Keller PJ. Whole-brain functional imaging at cellular resolution using light-sheet microscopy. *Nat Methods.* 2013;10(5):413–20.
- Orger MB, Kampff AR, Severi KE, Bollmann JH, Engert F. Control of visually guided behavior by distinct populations of spinal projection neurons. *Nat Neurosci.* 2008;11(3):327–33.
- Antinucci P, Hindges R. A crystal-clear zebrafish for in vivo imaging. *Sci Rep.* 2016;6:29490.
- Klar M, Hoffmann KP. Visual direction-selective neurons in the pretectum of the rainbow trout. *Brain Res Bull.* 2002;57(3–4):431–3.
- Ehrlich DE, Schoppik D. Control of movement initiation underlies the development of balance. *Curr Biol.* 2017;27(3):334–44.
- Nikolaou N, Lowe AS, Walker AS, Abbas F, Hunter PR, Thompson ID, et al. Parametric functional maps of visual inputs to the tectum. *Neuron.* 2012;76(2):317–24.
- Manteuffel G. Electrophysiology and anatomy of direction-specific pretectal units in *Salamandra salamandra*. *Exp Brain Res.* 1984;54(3):415–25.
- Manteuffel G. Binocular afferents to the salamander pretectum mediate rotation sensitivity of cells selective for visual background motions. *Brain Res.* 1987;422(2):381–3.
- Wylie DR. Binocular neurons in the nucleus lentiformis mesencephali in pigeons: responses to translational and rotational optic flowfields. *Neurosci Lett.* 2000;291(1):9–12.
- Wylie DR, Bischof WF, Frost BJ. Common reference frame for neural coding of translational and rotational optic flow. *Nature.* 1998;392(6673):278–82.
- Simpson JJ. The accessory optic system. *Annu Rev Neurosci.* 1984;7:13–41.
- Wylie DR, Frost BJ. Responses of pigeon vestibulocerebellar neurons to optokinetic stimulation. II. The 3-dimensional reference frame of rotation neurons in the flocculus. *J Neurophysiol.* 1993;70(6):2647–59.
- Masseck OA, Hoffmann KP. Question of reference frames: visual direction-selective neurons in the accessory optic system of goldfish. *J Neurophysiol.* 2009;102(5):2781–9.
- Simpson JJ, Leonard CS, Soodak RE. The accessory optic system of rabbit. II. Spatial organization of direction selectivity. *J Neurophysiol.* 1988;60(6):2055–72.
- Roeser T, Baier H. Visuomotor behaviors in larval zebrafish after GFP-guided laser ablation of the optic tectum. *J Neurosci.* 2003;23(9):3726–34.
- Krapp HG, Hengstenberg R, Egelhaaf M. Binocular contributions to optic flow processing in the fly visual system. *J Neurophysiol.* 2001;85(2):724–34.
- Egelhaaf M, Kern R, Krapp HG, Kretzberg J, Kurtz R, Warzecha AK. Neural encoding of behaviourally relevant visual-motion information in the fly. *Trends Neurosci.* 2002;25(2):96–102.
- Krapp HG, Hengstenberg R. Estimation of self-motion by optic flow processing in single visual interneurons. *Nature.* 1996;384(6608):463–6.
- Hopp E, Borst A, Haag J. Subcellular mapping of dendritic activity in optic flow processing neurons. *J Comp Physiol A Neuroethol Sens Neural Behav Physiol.* 2014;200(5):359–70.
- Haikala V, Joesch M, Borst A, Mauss AS. Optogenetic control of fly optomotor responses. *J Neurosci.* 2013;33(34):13927–34.
- Winship IR, Wylie DR. Receptive-field structure of optic flow responsive Purkinje cells in the vestibulocerebellum of pigeons. *Vis Neurosci.* 2006;23(1):115–26.
- Euler T, Hausselet SE, Margolis DJ, Breuninger T, Castell X, Detwiler PB, et al. Eyecup scope—optical recordings of light stimulus-evoked fluorescence signals in the retina. *Pflugers Arch.* 2009;457(6):1393–414.
- Joesch M, Plett J, Borst A, Reiff DF. Response properties of motion-sensitive visual interneurons in the lobula plate of *Drosophila melanogaster*. *Curr Biol.* 2008;18(5):368–74.
- Reiser MB, Dickinson MH. A modular display system for insect behavioral neuroscience. *J Neurosci Methods.* 2008;167(2):127–39.
- Miri A, Daie K, Burdine RD, Aksay E, Tank DW. Regression-based identification of behavior-encoding neurons during large-scale optical imaging of neural activity at cellular resolution. *J Neurophysiol.* 2011;105(2):964–80.

Ready to submit your research? Choose BMC and benefit from:

- fast, convenient online submission
- thorough peer review by experienced researchers in your field
- rapid publication on acceptance
- support for research data, including large and complex data types
- gold Open Access which fosters wider collaboration and increased citations
- maximum visibility for your research: over 100M website views per year

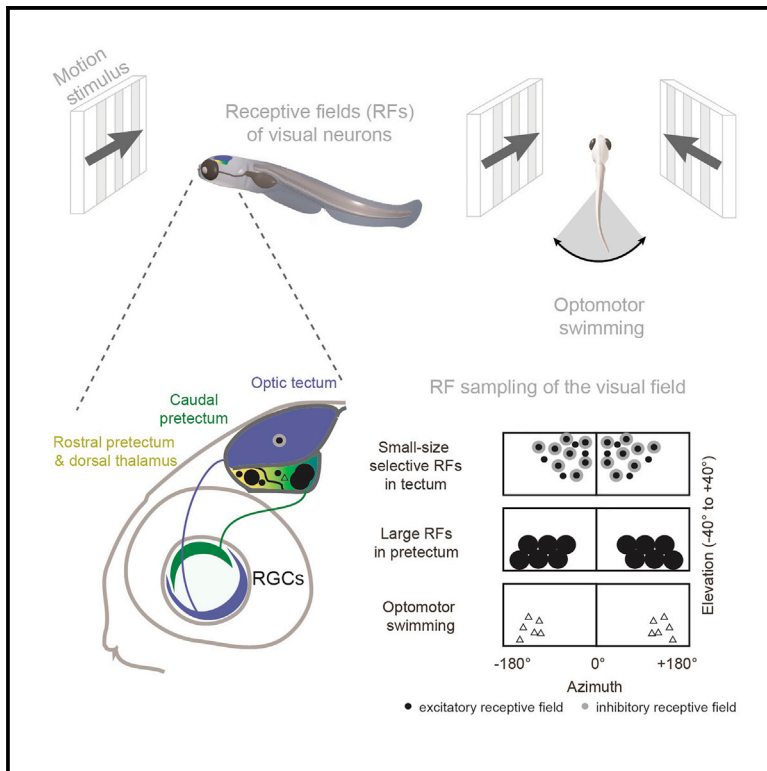
At BMC, research is always in progress.

Learn more biomedcentral.com/submissions



Parallel Channels for Motion Feature Extraction in the Pretectum and Tectum of Larval Zebrafish

Graphical Abstract



Authors

Kun Wang, Julian Hinz, Yue Zhang, Tod R. Thiele, Aristides B. Arrenberg

Correspondence

aristides.arrenberg@uni-tuebingen.de

In Brief

Wang et al. show that the zebrafish optic tectum and pretectum extract visual motion features associated with hunting and optomotor behavior, respectively. The tectum preferably represents small stimuli in the upper nasal visual field, whereas the pretectum is biased toward larger stimuli in the lower visual field.

Highlights

- Optic tectum and pretectum sample visual space differently (upper nasal versus lower)
- Receptive fields are mainly small-size selective in tectum and large in pretectum
- Motion in the lower temporal visual field drives optomotor swimming
- The unequal sampling is likely an adaptation to hunting and optomotor behavior



Parallel Channels for Motion Feature Extraction in the Pretectum and Tectum of Larval Zebrafish

Kun Wang,^{1,2,4} Julian Hinz,^{1,2,4,5} Yue Zhang,^{1,2} Tod R. Thiele,³ and Aristides B. Arrenberg^{1,6,*}

¹Werner Reichardt Centre for Integrative Neuroscience, Institute for Neurobiology, University of Tübingen, 72076 Tübingen, Germany

²Graduate Training Centre for Neuroscience, University of Tübingen, 72074 Tübingen, Germany

³Department of Biological Sciences, University of Toronto Scarborough, Toronto, ON M1C 1A4, Canada

⁴These authors contributed equally

⁵Present address: Friedrich Miescher Institute for Biomedical Research, 4058 Basel, Switzerland

⁶Lead Contact

*Correspondence: aristides.arrenberg@uni-tuebingen.de

<https://doi.org/10.1016/j.celrep.2019.12.031>

SUMMARY

Non-cortical visual areas in vertebrate brains extract relevant stimulus features, such as motion, object size, and location, to support diverse behavioral tasks. The optic tectum and preteectum, two primary visual areas in zebrafish, are involved in motion processing, and yet their differential neural representation of behaviorally relevant visual features is unclear. Here, we characterize receptive fields (RFs) of motion-sensitive neurons in the diencephalon and midbrain. We show that RFs of many preteectal neurons are large and sample the lower visual field, whereas RFs of tectal neurons are mostly small-size selective and sample the upper nasal visual field more densely. Furthermore, optomotor swimming can reliably be evoked by presenting forward motion in the lower temporal visual field alone, matching the lower visual field bias of the preteectum. Thus, tectum and preteectum extract different visual features from distinct regions of visual space, which is likely a result of their adaptations to hunting and optomotor behavior, respectively.

INTRODUCTION

Visual receptive fields (RFs) are specific regions in space where visual stimuli will alter the firing status of neurons (Spillmann, 2014). The ability of the visual system to extract useful information from the visual environment is directly related to the form, organization, and diversity of neuronal RFs within the vertebrate visual system. Task-relevant visual features are processed in parallel channels in the brain (Nassi and Callaway, 2009), starting in the retina (Baden et al., 2016).

The optic tectum and preteectum, two brain regions in the mes- and diencephalon, receive direct input from direction-selective retinal ganglion cells (Giolli et al., 2006; Hunter et al., 2013; Robles et al., 2014) and encode visual stimuli moving in different directions (Wang et al., 2019). These evolutionarily ancient structures share developmental origins with the superior colliculus (tectum) and part of the accessory optic system (AOS) (pretec-

tum) in mammals. They support navigation and orienting behavior in zebrafish—which lack a visual cortex—already soon after hatching in 5-day-old larvae (Beck et al., 2004; Niell and Smith, 2005). Zebrafish are an important model organism for non-cortical vision research, but the division of feature extraction tasks between tectum and preteectum is still largely unknown. In particular, their roles in feature extraction in relation to behavioral tasks are crucial for a mechanistic understanding of sensorimotor transformations in zebrafish.

In the preteectal area and in the AOS of many vertebrates, neurons having large RFs with broad direction tuning curves are abundant (Britto et al., 1981; Grasse and Cynader, 1984; Massey and Hoffmann, 2008; Simpson, 1984; Walley, 1967). Such large RFs should help the animal to distinguish wide-field optic flow from local motion and to estimate ego-motion. This computation is particularly important because many vertebrates use the outcome to stabilize gaze and body position (Portugues and Engert, 2009; Rinner et al., 2005). In larval zebrafish, both the optokinetic response (OKR) (Kubo et al., 2014) and the optomotor response (OMR) (Naumann et al., 2016) have been shown to rely on visual processing within the preteectum. In invertebrates, similar computations mediating OMR behavior were identified in the lobula plate, where horizontal system cells have large RFs with preferred directions matching the rotational optic flow around the yaw axis (Krapp et al., 2001). Additionally, it was shown that optogenetic manipulation of these neurons is sufficient to evoke yaw optomotor behaviors in fixed and tethered flies (Haikala et al., 2013; Busch et al., 2018). In zebrafish, the preteectum contains further anatomical sub-divisions (Yáñez et al., 2018), including structures involved in processing small visual stimuli during prey capture (Semmelhack et al., 2014; Muto et al., 2017), regions responsive to large-field motion stimuli (Kubo et al., 2014; Naumann et al., 2016), and a preteectal dopaminergic cluster providing input to the optic tectum (Tay et al., 2011). However, the RF properties of the preteectum at both the population and single neuron level are not known. It is also unclear how RF tuning within the preteectum may contribute to the production of visually mediated behaviors.

In contrast to the preteectum, RF sizes and locations for neurons within the zebrafish tectum have been described before (Niell and Smith, 2005; Sajovic and Levinthal, 1982; Bergmann et al., 2018; Preuss et al., 2014; Zhang et al., 2011). Tectal neurons have relatively small RFs, conforming to the idea that tectal



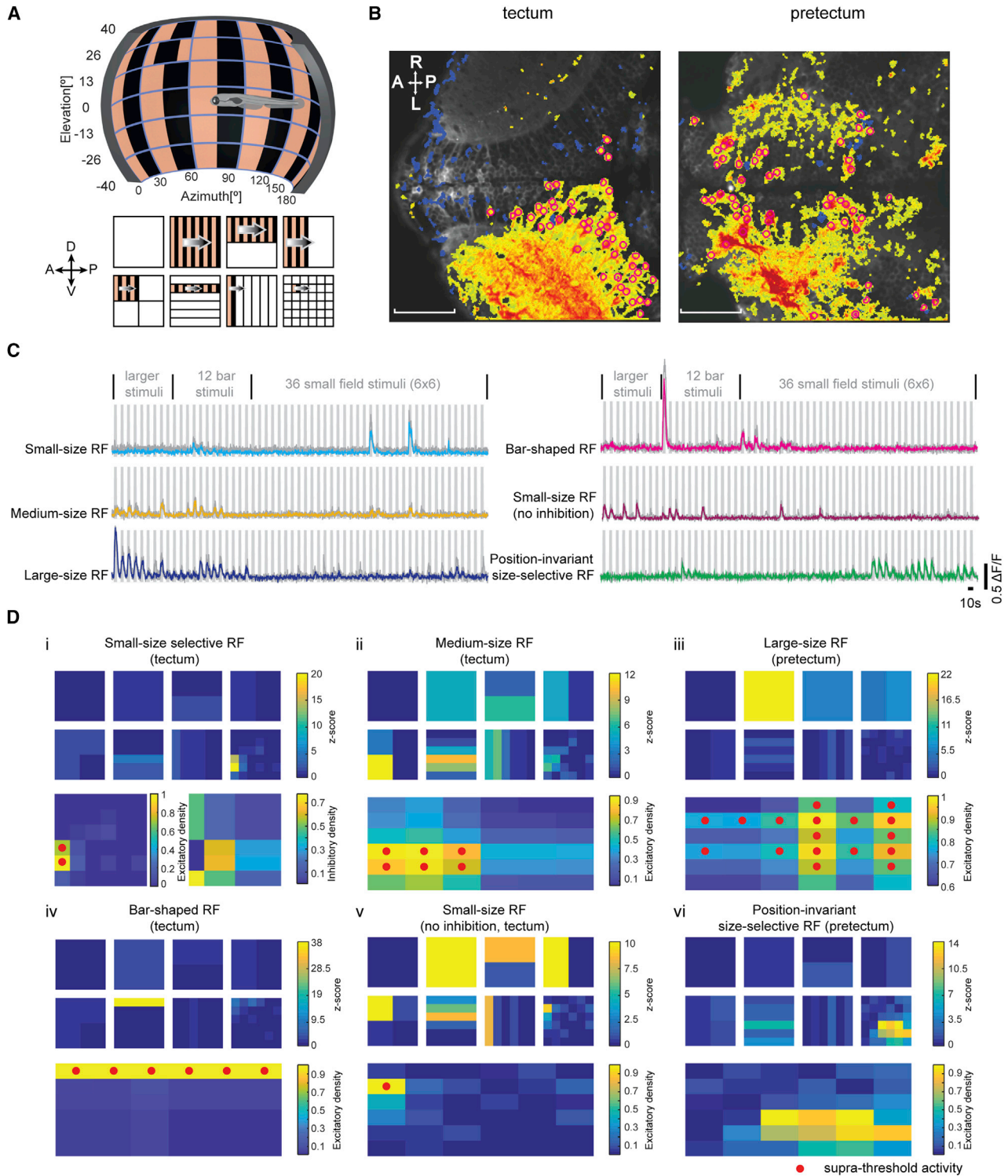


Figure 1. Different Receptive Field (RF) Types Were Identified Using Horizontally Moving Gratings

(A) Stimuli of naso-temporally moving gratings covering view fields of variable sizes were presented to the animal's right eye ($n = 8$ fish for naso-temporal and $n = 2$ fish for temporal-nasal motion). Motion stimuli consisted of whole-field (1×1 , $180^\circ \times 80^\circ$, azimuth \times elevation), half-field ($2 \times 1/2$ and $1/2 \times 2$), quarter-field ($2 \times 2 \times 1/4$), bar ($6 \times 1/6$ and $1/6 \times 6$), and small-field ($6 \times 6 \times 1/36$, each $30^\circ \times 13^\circ$) stimuli. The non-stimulated regions are shown in white for illustration purposes but contained a stationary grating. A snapshot during the small-field motion phase (depicted in the lower right) is shown on the display in the setup illustration (top).

(legend continued on next page)

neurons detect small-size moving objects in the view field and are needed for hunting behavior (Gahtan et al., 2005).

It is expected that each of the brain areas receiving input from the retina is adapted to the specific tasks and behaviors the animal executes in its environment. The behavioral relevance of a visual stimulus is influenced by the visual field location of the stimulus and will depend on the particular visually mediated behavior and the probability of observing such stimulus locations under natural conditions. For example, in the brain of macaque monkeys, it has been shown that RF properties in the superior colliculus, the homolog of the optic tectum, widely differ in the upper and lower visual view field, which likely represents adaptations to near space in the lower and far space in the upper visual field (Hafed and Chen, 2016). During hunting behavior, vertebrates typically keep the prey items, which are oftentimes small stimuli, in their nasal or frontal visual field, indicating that high visual acuity in this region of space is advantageous. Accordingly, both the primary visual cortex and superior colliculus show a magnification of foveal visual field regions (Grujic et al., 2018; Schwartz, 1980), i.e., more neurons are dedicated to representing these foveal locations than more peripheral locations. In the zebrafish retina, a region of heightened photoreceptor density (area centralis) has also been described (Schmitt and Dowling, 1999), corresponding to upper nasal visual field positions (Zimmermann et al., 2018). During prey capture, prey items need to be detected against the visual background, whereas for visual stabilization behaviors, animals need to detect their ego-motion by analyzing the global optic flow patterns resulting from the displacement of their bodies relative to the visual surround. To use brain resources efficiently, the reliable detection of optic flow directions is likely biased toward making use of the most informative visual field locations that occur in natural habitats and during behavior. The OMR is driven effectively by whole-field motion but—to our knowledge—there are no previous reports on particular visual field regions being preferably sampled by the animal to initiate OMR. Given the different roles of the optic tectum and the pretectum in hunting and stabilization behavior, respectively, it seems likely that these brain areas represent the visual field differently. It is unclear, however, whether the observed retinal anisotropies are relayed to primary visual areas in the zebrafish brain and whether magnifications of certain visual field locations exist in the tectum or pretectum of zebrafish. The characterization of such brain area-specific magnifications within the small vertebrate brain of larval zebrafish would advance our understanding of the efficient encoding of relevant information in the vertebrate brain

and help to reveal the specific computations that brains have evolved to perform.

Here, we characterize the RF properties of tectal and pretectal motion-sensitive neurons using *in vivo* 2-photon calcium imaging of GCaMP5G transgenic animals and investigate their organization in visual and anatomical space. In addition, we investigate how the identified RFs match to the visual locations, which drive the OMR behavior. Our results reveal complementary roles of the optic tectum and pretectum to support behaviorally relevant motion feature extraction.

RESULTS

To estimate RF properties of pretectal and tectal neurons, we stimulated the right eye of immobilized larval zebrafish with a series of horizontally moving grating patterns of different sizes and locations (Figures 1A and S1; STAR Methods) and measured GCaMP5G calcium responses of neurons in the diencephalon and midbrain (Figure 1B). 1,926 motion-sensitive neurons that responded reliably during the three repetitions of the stimulus protocol were recorded in 10 animals. Neurons were divided into four functionally defined groups (Figures 1C, 1D, and S2; see STAR Methods for classification), based on the size and shape of their RFs: (1) small-size RFs, (2) medium-size RFs, (3) large-size RFs, and (4) bar-shaped RFs. RF sizes ranged from very small RFs ($30^\circ \times 13^\circ$) to whole field (168° azimuth \times 80° elevation). In neurons with smaller RFs, we oftentimes observed suppressive effects for larger motion stimuli (Figure 1Di), showing that these neurons were small-size selective. Small-size RF neurons without signs of inhibition were frequently encountered as well; even though the excitatory RF density (STAR Methods) was localized to a small patch in the visual field, the neurons were also responsive to whole-field stimuli (Figure 1Dv). Furthermore, some of the small-size and medium-size RF neurons each responded to small moving stimuli in a range of different visual field positions but did not respond to larger moving stimuli covering the same visual field locations, i.e., their responses were small-size selective and position invariant (Figure 1Dvi).

Pretectal RFs Are Larger Than Tectal RFs and They Are Less Often Size Selective

For each motion-sensitive neuron, we measured the location of the RF center in the visual field and the anatomical position of the soma in the brain (see STAR Methods). Based on morphological tectal borders visible in our brain volumes and previous anatomical annotations of the pretectum and tegmentum

(B) The average fluorescence of an example calcium-imaging time series recorded from tectum and pretectum (PT) is shown in gray. Motion-sensitive image pixels are shown in false color, with warm and cold colors corresponding to positive and negative motion phase correlation, respectively. Manually selected regions of interest (ROIs) are labeled with magenta circles. Scale bar, 50 μ m; A, anterior; P, posterior; L, left; R, right.

(C) Example $\Delta F/F$ calcium responses of neurons with different RF sizes or shapes are shown. For each neuron, the colored trace corresponds to the median response across three repetitions (gray traces). The gray rectangular shades correspond to the 57 presented motion phases.

(D) RF maps for six example neurons corresponding to (C). Top: the eight squares correspond to the eight stimulus segments shown in (A), and each square corresponds to the stimulus arena surface ($180^\circ \times 80^\circ$, azimuth \times elevation). The calcium response is plotted as a Z score for each stimulus phase (for each ROI, the $\Delta F/F$, subtracted by the average of the $\Delta F/F$, divided by the standard deviation of the baseline $\Delta F/F$). Bottom: by comparison of the activities evoked by spatially overlapping stimuli of different sizes, excitatory RF densities were calculated to measure the size of the RFs as the number of patches with supra-threshold activity (red dots). For cells with small-size excitatory RFs with maximal responses during the small-size stimulus phases (see STAR Methods), an inhibitory RF density was calculated to judge the extent of small-size selectivity (cell i). The anatomical location of each neuron is indicated (tectum or PT).

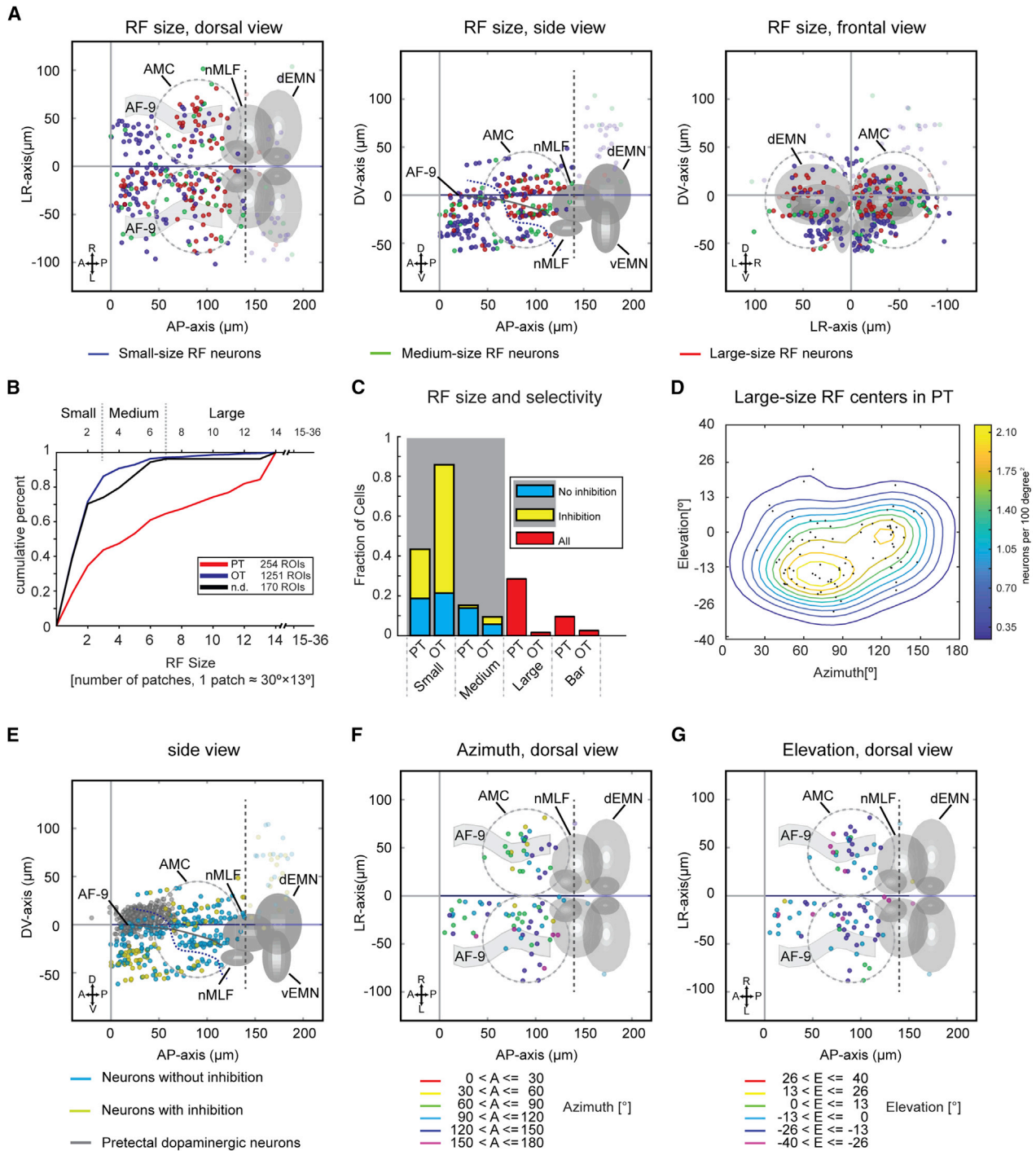


Figure 2. Pretectal RFs Are Large and Biased toward the Lower Visual Field

(A) Anatomical map of small-size (blue), medium-size (green), and large-size (red) RF neurons in the pretectal region. ($n = 10$ fish, 5 composite pretectal regions). Each colored dot represents a single neuron. Coordinates are defined as distances relative to the posterior commissure in the diencephalon (anterior-posterior axis and dorso-ventral axis) and midline (left-right axis). Many identified neurons were located within the previously annotated main pretectal cluster (AMC, dashed circle; Kubo et al., 2014) and additional neurons were located further rostrally (in the rostral PT and in the dorsal thalamus; Figures S6A–S6D). Neurons located $\geq 140 \mu\text{m}$ caudal to the posterior commissure (lighter colors) were located in the tegmentum and excluded from pretectal analysis (dashed gray line), whereas all rostral diencephalic neurons were included in the analysis.

(legend continued on next page)

(Kubo et al., 2014; Randlett et al., 2015), we identified tectal and tegmental neurons, as well as those located within the general pretectal area (Figure 2A). Neurons located in the tectum were excluded from further analysis. Within the general pretectal area, the caudal region corresponded to the pretectal anterior medial cluster (AMC) region described before (Kubo et al., 2014). In the recorded rostral diencephalic region, the dorsal part corresponded to the rostral pretectum (dorsal periventricular pretectal nucleus marked with dopaminergic neurons) and the ventral part to the dorsal thalamus annotated in the Z-Brain Atlas (Figures S6A–S6D) (Randlett et al., 2015; also see Discussion). However, the adult zebrafish brain contains several pretectal nuclei (Yáñez et al., 2018), and their exact identities and locations in the larval zebrafish brain still need to be resolved. We, therefore, included all diencephalic neurons in the analysis of the general pretectal area in this study. We investigated the topography of pretectal and tectal neurons as well as their sampling of the visual field. On average, we identified 205 ± 6 motion-sensitive neurons per tectum and 59 ± 13 neurons per pretectal region ($n = 10$ fish, corresponding to 5 complete composite brains sampled in 10- μm steps).

Pretectal neurons have larger excitatory RFs than those of tectal neurons (Figures 2B and 2C). Within the general pretectal area, 30% (88/295) of the motion-sensitive neurons had a large-size RF, compared to less than 2% (19/1,251) of the neurons within the tectum (Figure 2C). Most motion-sensitive tectal neurons (86%; Figure 2C) had excitatory RFs smaller than 1,200 deg^2 in area (3 of our small stimulus patches, each covering $30^\circ \times 13^\circ$ in azimuth and elevation), which is consistent with previous reports from other groups (Sajovic and Levinthal, 1982; Bergmann et al., 2018). Furthermore, similar to the findings in a previous report (Preuss et al., 2014), we found that 68% (853/1,251) of motion-sensitive neurons in the tectum were size selective, i.e., motion stimuli that were larger than the neuron's excitatory RF evoked lower calcium responses (Figures 1Di and 2C). In contrast, only 26% (77/295) of the motion-sensitive neurons in the general pretectal area were size selective (Figure 2C).

Large-Size RFs in the Caudal Pretectum Are Biased to the Lower Visual Field

The RF centers of 69% of the large-size RF pretectal neurons were located in the lower visual field, which represents a significant bias (Figures 2D and S1B; $p = 0.0002$, z test for one propor-

tion). These pretectal large-size RF neurons were located almost symmetrically in both hemispheres of the caudal pretectum, with some neurons in the rostral pretectum on the contralateral side (laterality index = -0.30 ; Figure 2A). The high number of ipsilateral neurons can—in part—be explained by reflections of the stimulus, which was revealed in an additional experiment in which the left eyes of the fish were blocked by a back foil (laterality index = -0.86 ; $n = 6$ fish, 6 pretecta; Figure S1C). In addition to the large-size RF neurons observed in the caudal pretectum, many neurons responsive to small moving stimuli were also identified (Figures 1Cvi, 2A, S6E, and S6F). These small-size RF neurons were most frequent in the rostral diencephalic region, which corresponds to the rostral pretectum and the dorsal thalamus (see Discussion; Figures S6A–S6D).

Because functionally identified neurons in the rostral diencephalon segregated from those in the caudal pretectum through an anatomical gap containing only few motion-sensitive neurons (Figure 2A, side view), we defined a boundary based on this gap to separate these two anatomical clusters (dashed line in Figures 2A, S4A, and S4B, and STAR Methods). The rostral diencephalic region contained a higher proportion of small-size RFs (57%, 85/148) than the caudal pretectum (29%, 43/147; $p < 0.001$, z-test for two proportions), whereas the caudal pretectum contained a higher proportion of large-size RFs (43%, 63/147) than the rostral diencephalic region (14%, 21/148; $p < 0.001$, z-test for two proportions) (Figures 2A and S1C). Furthermore, the rostral region contained a higher proportion of small-size selective neurons (Figures 2E and S4B–S4D), whose activity was suppressed for larger stimuli (rostral region: 34% [51/148], caudal pretectum: 18% [26/147], $n = 148$ and 147, $p < 0.001$, z-test for two proportions, see STAR Methods). Rostral diencephalic neurons responsive to our smallest grating stimuli were also frequently (63% of the neurons, $n = 6$ fish) responsive to small horizontally moving dots of variable diameters (3 to 18 degrees in diameter), as we tested in a separate experiment (data not shown).

It is well established that soma positions of zebrafish tectal neurons are topographically arranged within the tectum and that the RF centers cover almost the whole visual field at the population level (Attardi and Sperry, 1963; Niell and Smith, 2005; Romano et al., 2015; Bergmann et al., 2018). However, in the pretectum, we did not observe a clear topographic distribution of large-size RF neurons (Figures 2F, 2G, S1D, and S1E).

(B) Analysis of RF size differences across PT/diencephalon and optic tectum (OT). The cumulative distribution of RF sizes is shown for the general pretectal region within the diencephalon (PT, red), the OT (blue), and neurons of undefined provenance (black). Note that the PT has a larger fraction of large-size RF cells than the tectum.

(C) For each brain region (PT and OT), the fractions of small-size, medium-size, large-size, and bar-shaped RFs are shown. For small- and medium-size RFs, the inhibitory surround was investigated, and neurons with such inhibition are plotted in yellow.

(D) Locations and density contour plot of RF centers of large-size RF pretectal neurons in the contralateral and ipsilateral hemispheres ($n = 10$ fish, 5 composite brains).

(E) Anatomical map of three types of neurons in the pretectal region: neurons with (yellow) and without (cyan) signs of inhibition and pretectal dopaminergic neurons (gray). The dopaminergic neurons served as a landmark for the dorsal periventricular pretectal nucleus in the rostral PT and were recorded in a separate experiment.

(F and G) Topographic maps of large-size RF neurons in the pretectal region. Each colored dot represents a single neuron with its RF center in the indicated azimuth (F) and elevation (G) range ($n = 10$ fish, 5 composite pretectal regions).

Abbreviations are as follows: dEMN, dorsal extraocular motor neuron; vEMN, ventral extraocular motor neuron; dEMN and vEMN, the trochlear and oculomotor nuclei; nMLF, nucleus of the medial longitudinal fasciculus; A, anterior; P, posterior; D, dorsal; V, ventral; L, left; R, right; AF, arborization field. The abbreviations are applicable to all anatomical maps in this study.

Tectal RFs Dominate the Upper Nasal View Field

As expected from the topographic retino-tectal projection of retinal ganglion cells, strong rostro-caudal, dorso-ventral, and medio-lateral topographical gradients of RF centers were found for small-size RF neurons in the optic tectum (Figures 3B, 3D, 3E, and S3A). Responding tectal neurons were mainly located in the contralateral hemisphere relative to the stimulated eye (laterality index = -0.88 ; Figures 3D and 3E; see STAR Methods). More tectal neurons with small-size RFs corresponding to the upper nasal visual field were found than corresponding to the lower temporal visual field (420 versus 55 neurons, upper nasal versus lower temporal view field, Z score test for proportions: $p < 0.001$; Figures 3A and 3C). When comparing the upper nasal view field (26° elevation, 30° azimuth) to the lateral view field (0° elevation, 90° azimuth), the sampling difference corresponded to a 1.6-fold magnification factor (Figure S3B). In our experiments, we identified about 4 tectal small-size RF neurons per $10^\circ \times 10^\circ$ in the upper nasal field in each completely sampled fish (hypothetical sampling every $5 \mu\text{m}$ in the dorso-ventral direction, calculated based on our actually recorded 33.4 tectal motion-sensitive neurons per $60^\circ \times 27^\circ$ in each of 5 composite brains sampled every $10 \mu\text{m}$; see Figures S3B–S3D).

Zebrafish OMR Behavior Is Driven Best by Motion in the Lower Temporal Visual Field

Although it is known that during hunting behavior, prey stimuli are mostly located in nasal visual field locations in zebrafish (Bianco et al., 2011), the visual field regions that drive OMR and OKR behavior have not been identified. OMR behavior can be stably induced with whole-field forward motion projected from below or from the side in larval zebrafish (Severi et al., 2014; Thiele et al., 2014), and it had been assumed that large—or even whole-field—stimuli are necessary to drive stabilization behaviors. Given the uneven distribution of large-size RFs in the upper and lower visual fields in the pretectum (Figure 2D), we wanted to test whether OMR is mainly driven by the forward motion located in the lower visual field, which would implicate the large-size RF neurons in mediating the OMR behavior. We, therefore, recorded the tail motion of larvae while forward-moving gratings of different sizes were presented in different visual field locations. Care was taken to always stimulate animals in a binocularly symmetric fashion to drive forward OMR instead of OMR turning behavior (Figures 4A, 4B, S5A, and S5B). The angle between the anterior-posterior body axis and the tail tip was traced to detect single tail beats and swim bouts (Figures 4A, 4D, and 4E). Bouts, consisting of a series of tail undulations beating symmetrically to both sides (forward OMR), were induced in response to whole-field forward-moving gratings (Video S1, S2, S3, and S4). In contrast, unsymmetrical unilateral turning swim beats to one side (turning OMR) were oftentimes evoked by whole-field rotating visual stimuli, although symmetrical beats (forward OMR) were also observed (Figure S5F). Whole-field and half-field visual stimuli covering the temporal or lower view field could evoke forward OMR robustly (Figure 4C).

To our surprise, forward OMR swim beats could be induced by stimuli as small as $45^\circ \times 20^\circ$ (azimuth \times elevation, the smallest size in our protocol) in the lower temporal view field of both

eyes (Figure 4C). The OMR-evoking visual field locations were almost identical across all recorded animals ($n = 6$; Figure 4F). To test whether the OMRs evoked by small stimuli are stronger than what would be expected under the assumption that OMR drive was established by the sum of equal-sized motion inputs across the visual field, we normalized the evoked OMR tail-beat rate to the respective stimulus field size (analogous to the excitatory RF density estimation; see STAR Methods). The resulting visual field map of OMR drive (Figure 4G) shows the disproportionately large influence of moving stimuli in the lower temporal view field. We then compared OMR drive across different stimulus sizes (1×1 , 2×1 , ... 4×4), always considering the visual field positions/stimulus phases that drove OMR best. This analysis revealed that the smallest stimulus area evoked responses, which were on average ~ 11 times stronger than expected by an equal integration of optic flow inputs across the visual field (Figure 4H).

DISCUSSION

Our study reveals the functional segregation of visual motion processing in parallel channels, each extracting different sets of motion features across the visual field. The optic tectum, which processes the motion of small visual stimuli, has a bias for upper nasal visual field locations. Within the diencephalon, wide-field optic flow is mainly processed in the caudal pretectum using large RFs that mainly sample the lower visual field, whereas small motion stimuli are mainly processed in rostral regions of the diencephalon. Furthermore, we show that animals observe mainly the lower temporal visual field for optomotor forward swimming.

These findings agree with the need to process small visual stimuli, e.g., during prey capture (Preuss et al., 2014; Bianco et al., 2011), and the need to assess wide-field motion to inform stabilization behaviors (Kubo et al., 2014). The data support a circuit model in which these two distinct tasks are processed independently by multiple channels in different brain areas.

Caudal and Rostral Diencephalic Regions Are Biased toward the Encoding of Large-Field Optic Flow and Small Stimuli, Respectively

Within the diencephalon, large-size RF neurons are mainly found in the caudal pretectal region, whereas small-size RF neurons are biased toward more rostral anatomical locations. The large-size RFs of pretectal neurons preferably sample the lower half of the visual field (Figures 2D and S1B), which fits with previous reports from pretectal neurons in dogfish (Masseck and Hoffmann, 2008). Due to our use of a half-cylindrical stimulus arena to present exclusively horizontally moving stimuli to the right eye, neurons with more complex, e.g., rotational, binocular, or vertical optic flow fields could not be described in this study (Kubo et al., 2014; Wang et al., 2019). These types of RF structures exist in visual neurons of other species (Krapp et al., 2001; Karneier et al., 2003), and future studies are needed to identify them in zebrafish.

The adult zebrafish pretectum contains several nuclei distributed from the superficial to the periventricular regions, receives numerous retinal and tectal afferents, and projects to the optic

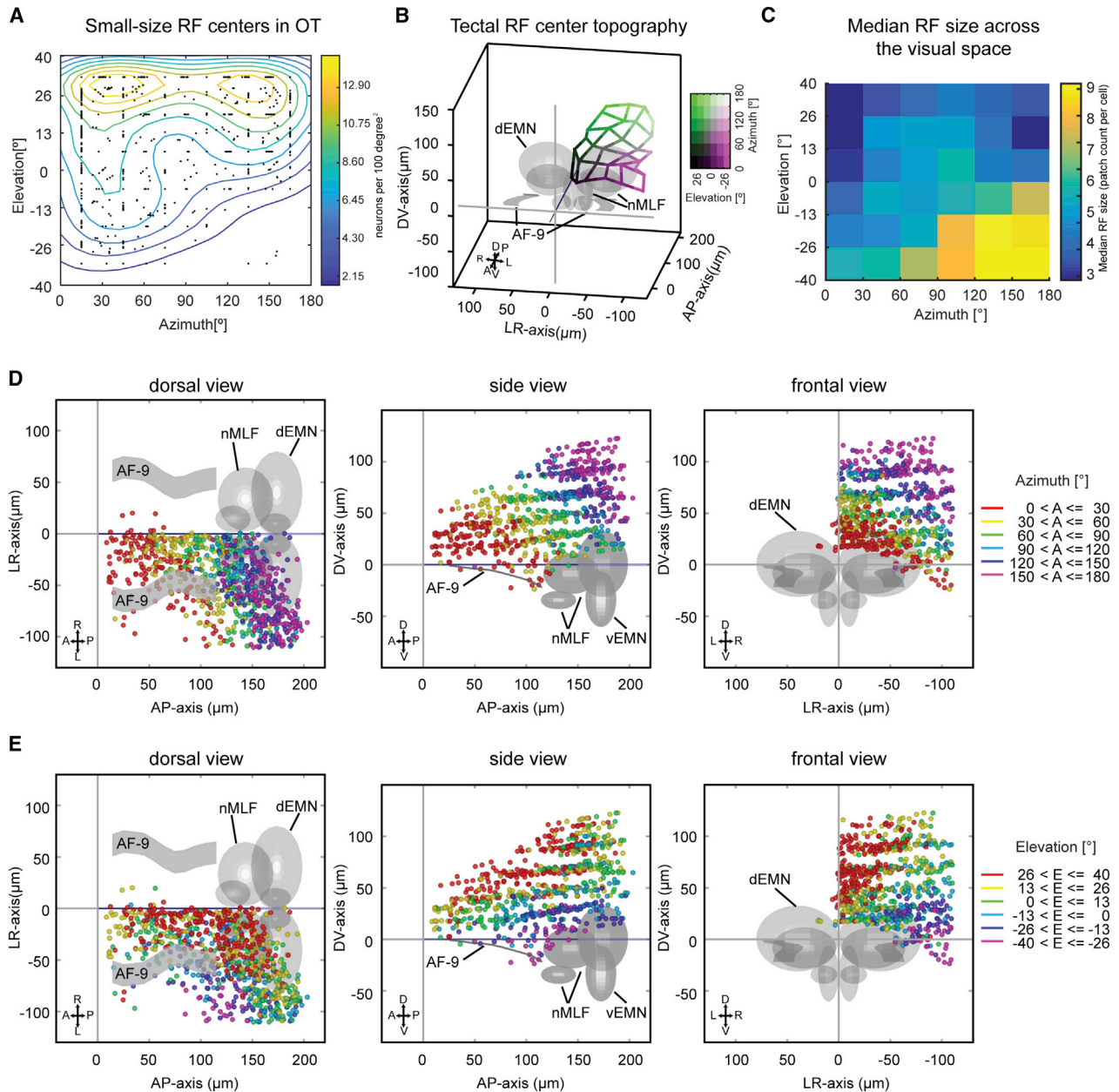


Figure 3. Tectal RFs Are Small and Biased toward the Upper Nasal Visual Field

(A) Visual field locations and density contour plot of RF centers of small-size RF tectal neurons ($n = 10$ fish, 5 composite tecta).

(B) Anatomical map of the tectal RF center topography. The average anatomical position of neurons with their RF centers in each of the 6×6 visual field bins was calculated and all 36 locations were connected by a grid to illustrate the mapping of visual space (color legend in the upper right) corresponding to anatomical space in the tectum (Figure S3A). The yaw angle (10° right) and the pitch angle (20° down) were adjusted to allow optimal view of the anatomical topography.

(C) Median RF size across the visual space. For each patch, we calculated the median RF sizes of all neurons (in tectum and PT) whose excitatory RFs covered the patch in question. The animals sample the lower temporal visual field mainly with large-size RF neurons, whereas small-size neurons dominate in the upper nasal visual field.

(D and E) Topographic maps of tectal small-size RF neurons for azimuth (D) and elevation (E). Each colored dot represents a single neuron with its RF center in the corresponding azimuth range in (D). For example, all RF centers of the neurons in red are located between 0° azimuth (in front of the fish) and 30° azimuth on the nasal right side of the fish. In (E), each colored dot represents a single neuron with its RF center in the corresponding elevation range. For example, RF centers of the neurons in green are located slightly above the equator of the view field (0° to 13° in elevation). $n = 10$ fish, 5 composite brains.

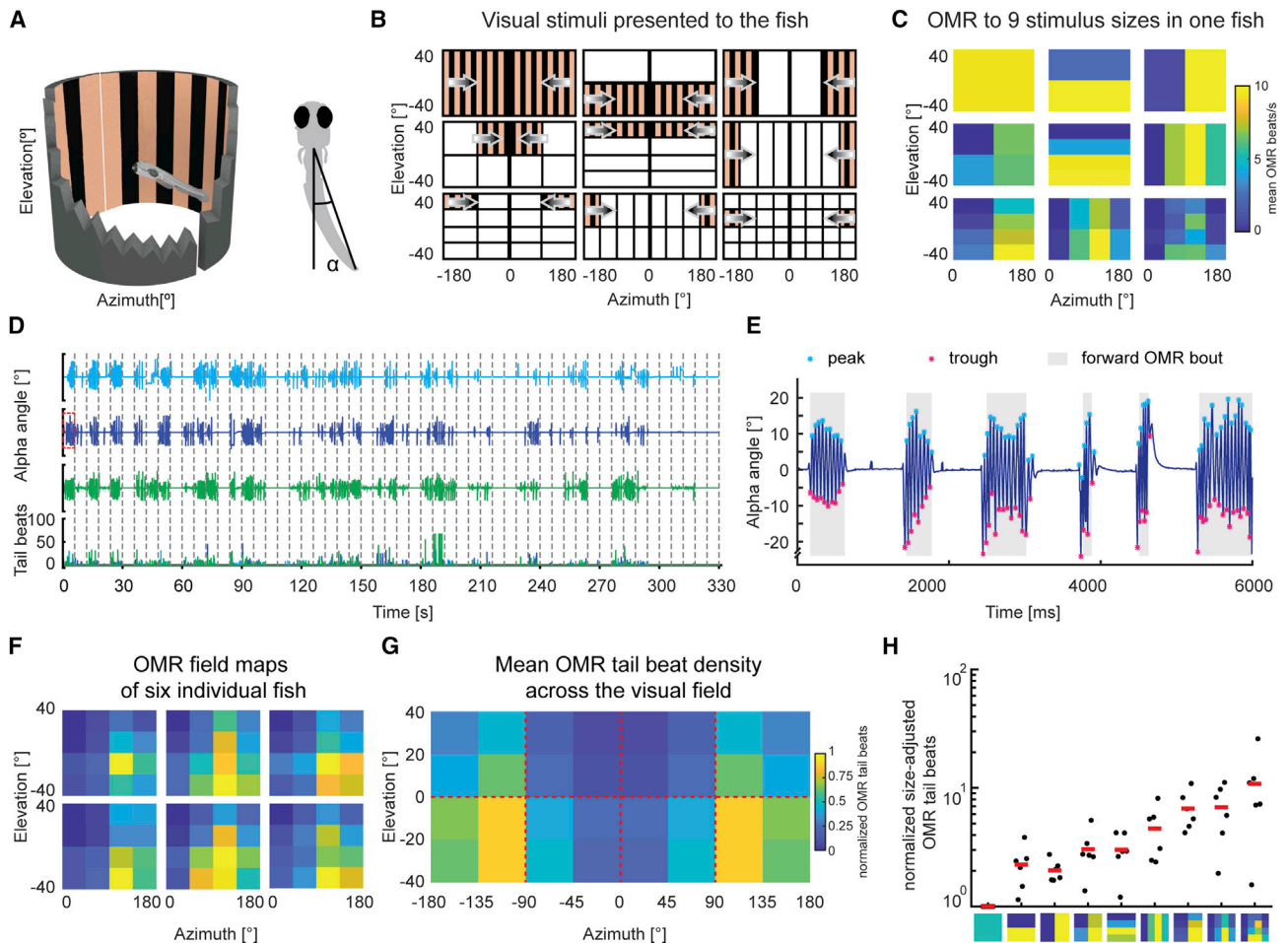


Figure 4. Zebrafish Optomotor Responses Are Driven by Motion from Below and in the Rear of the Animal

(A) Left: stimuli were presented binocularly to the animal with two half-cylindrical arenas while the behavior of the fish was recorded. A snapshot of the visual stimulus during the whole-field motion phase is shown in the setup illustration. Right: a schematic of a larval zebrafish performing OMR behavior. The indicated angle between the anterior-posterior body axis and the tail tip was measured to judge OMR performance.

(B) Motion stimuli of the OMR experiment consisted of whole-field (1×1 , 180° azimuth \times 80° elevation), half-field ($2 \times 1/2$, $1/2 \times 2$), quarter-field ($2 \times 2 \times 1/4$), bar ($4 \times 1/4$, $1/4 \times 4$), medium-field ($4 \times 2 \times 1/8$ and $2 \times 4 \times 1/8$), and small-field ($4 \times 4 \times 1/16$, each $45^\circ \times 20^\circ$) stimuli (for each size group, only one motion patch is illustrated). Each stimulus was mirror-symmetric about the mid-sagittal plane and shown with two half cylindrical arenas from both sides. The control stimulus phases (not shown in B) consisted of two stationary whole-field phases, counterclockwise and clockwise rotational moving gratings or looming visual stimuli on either side (Figure S5B). The regions in which no stimulus movement was present are shown as white areas for illustration purposes but contained a stationary grating.

(C) Average number of tail undulations per second for one larva, induced by forward-moving gratings of 9 different sizes (rectangles represent the stimulus hemifields from B).

(D) The full behavioral session for one animal, showing induced OMR behavior by stimuli of different sizes and locations as indicated in (B). The three stimulus repetitions are shown in different colors (cyan, blue, and green). Individual stimulus phases are separated by the dashed gray lines, and each row corresponds to 55 concatenated time periods in which motion stimuli were presented. The stimulus pauses in-between motion phases were cropped out and lasted 69 s each. Measured tail-beat counts (bottom) during each trial were consistent across the three repetitions.

(E) Tail movements induced by whole-field forward-moving gratings (from trial No. 2 indicated by a red rectangle in D). The peaks and troughs of each swim bout within the 6-s recording are labeled with cyan and magenta asterisks, respectively. OMR swim beats are indicated by gray background shade.

(F) Visual field heatmaps of the forward-OMR tail-beat rate for six individual larval zebrafish ($n = 6$). The visual field density of OMR behavior was quantified analogous to the excitatory RF densities in Figure 1. The density was normalized according to the size of the stimulation area in each fish individually (see STAR Methods).

(G) Average heatmap of the OMR beat density for stimulation across different visual field coordinates ($n = 6$ fish).

(H) Maximum OMR beats for each of the 9 stimulus fields shown in (B) and (C) after normalization according to stimulus size (see STAR Methods).

tectum as well (Fernald and Shelton, 1985; Presson et al., 1985; Kastner et al., 2010; Yáñez et al., 2018). The correspondence of these nuclei to functionally defined larval brain regions

is not fully resolved (Kubo et al., 2014; Muto et al., 2017; Semmelhack et al., 2014; Arrenberg and Driever, 2013). In our study, the pretectal dopaminergic neurons, which are evolutionarily

conserved across most amniotes (Yamamoto and Vernier, 2011), were used as a landmark to indicate the location of the periventricular pretectal nucleus (Filippi et al., 2014). The location of caudal pretectal neurons in this study corresponds to the AMC, previously described by Kubo et al. (2014), as well as to the annotated pretectal brain volume in the Z-Brain Atlas (Figures S6A–S6C; Randlett et al., 2015). Recorded extra-tectal neurons located more than 140 μm caudal to the posterior commissure most likely belonged to the tegmentum and were, therefore, excluded from the pretectal analysis (see STAR Methods). The rostral diencephalic neurons described in this study cover rostral pretectal and dorsal thalamic brain regions (Videos S5, S6, and S7) (Rupp et al., 1996; Yáñez et al., 2018). Functional properties of two larval pretectal nuclei have previously been described in relation to prey capture (parvocellular and magnocellular superficial nuclei [Psp and PSm]); however, they are located more laterally than the bulk of our recorded motion-sensitive neurons in the rostral pretectum (Semmelhack et al., 2014; Muto et al., 2017). Morphologically, the identity, extent, and overlap of larval pretectal neuron populations, which give rise to each of the known adult pretectal nuclei, is not easily discernible (Arrenberg and Driever, 2013). Further anatomical studies are needed to link our functionally identified neurons to specific pretectal and thalamic brain nuclei and connectivity in the larval brain.

The anatomical and visual field locations, as well as neuron numbers, were consistent for large-size RF neurons in the pretectum across fish and experiments (Figures 2A, 2D, S1B, and S1C), whereas the responses of position-invariant RF neurons (Figure 1Dvi) appeared to be more variable. Notably, the preferred visual field locations, exact anatomical locations, and the number of identified position-invariant neurons within the diencephalon differed in the first and second experiment we performed (Figures S4E and S4F). Further work is needed to elucidate the specific anatomical distribution and response properties of position-invariant RF neurons.

The Tectum—Poised for Prey Capture

Our analysis of a large number of tectal neurons extends previous reports on tectal physiology (Niell and Smith, 2005; Sajovic and Levinthal, 1982; Zhang et al., 2011; Preuss et al., 2014). Our finding that the tectum mostly comprises relatively small excitatory RFs, which oftentimes are small-size selective, is in agreement with a role of the tectum in prey capture (Bianco et al., 2011; Gahtan et al., 2005). It is noteworthy that our stimulus protocol only allowed the measurement of RF sizes down to 30° horizontally and 13° vertically (corresponding to our smallest visual stimulus), which is much larger than the minimal RF size in a previous report (Preuss et al., 2014). Also, due to the limitation of 2-photon calcium imaging, we are not able to directly assess inhibition but assess it only indirectly by comparing the reduction in responses evoked by larger stimuli.

The topographic arrangement of the zebrafish tectal neurons is well established both for the anatomical retino-tectal projection (Baier et al., 1996; Trowe et al., 1996) and the functional RF mapping (Bergmann et al., 2018; Niell and Smith, 2005). However, precise measurements of dedicated tectal anatomical volumes had not been performed previously and are needed to build faith-

ful models of zebrafish vision. We find that the upper nasal visual field (134 $\mu\text{m}^3/\text{deg}^2$) is magnified in the tectum by a factor of 1.6 relative to lateral (82 $\mu\text{m}^3/\text{deg}^2$) visual field locations (Figure S3), which is a relatively mild magnification in comparison to foveal magnification in the primate superior colliculus and visual cortex (Schwartz, 1980; Cowey and Rolls, 1974; Grujic et al., 2018). Given that the larval prey capture behavior depends on the optic tectum and larvae respond to the paramecia located in front and extending 60° temporalward of the fish (Bianco et al., 2011; Romano et al., 2015), a role of these tectal small-size RF neurons in prey capture seems likely. Because the density of small-size RF neurons is elevated in the upper nasal view field (Figures 3A and S3B), this would suggest that larval prey capture performance is best when the paramecia are located in front and slightly above the eyes and possibly the mouth. In this study, we have only investigated the RF distributions at a single developmental stage. It is possible that the reported tectal magnification of the upper nasal visual field is (in part) a result of the tectal developmental stage because new, initially non-functional neurons are added in the dorso-medial and caudo-lateral tectum (Boulanger-Weill et al., 2017; Recher et al., 2013).

The OMR Is Driven Most Strongly by the Lower Temporal Visual Field

Although it had been known from previous reports that motion stimuli presented from the bottom or from the side are effective in triggering OMR behavior (Thiele et al., 2014; Severi et al., 2014; Orger et al., 2008), it was unclear which parts of the visual field the animal preferentially responds to. We tested motion stimuli of variable size and position against a stationary background and show that for forward swimming OMR, the relevant region lies in the lower temporal view field of the fish (Figures 4F and 4G). We found that even motion stimuli as small as 45° × 20° (azimuth × elevation) can be effective OMR stimuli. This finding is in contrast to the concept that the OMR is a whole-field-induced behavior. Rather, it suggests that distinct parts of the visual field are sampled for body stabilization behaviors. This most likely reflects the ecological adaptations of zebrafish living in shallow waters (Engeszer et al., 2007) and the need to sample the most relevant parts of the visual field for different tasks (Zimmermann et al., 2018), such as putative high contrast textures within a river bed. Notably, zebrafish also sample different parts of their visual field for a related stabilization behavior, the OKR. The OKR of zebrafish is best driven by stimuli located laterally and slightly elevated (Dehmelt et al., 2019). Thus, each visually mediated behavior that has been investigated for visual field anisotropies (OMR, OKR, and prey capture behavior) preferentially samples information from different parts of visual space.

Because RGCs project directly to the optic tectum and pretectum (Robles et al., 2014), it seems likely that the small-size RFs without inhibition as well as the large-size RFs in the caudal pretectum are established by direct inputs from RGCs (Figure 5). Small-size-selective responses require inhibitory inputs, which could be calculated already within the retina or within the retino-recipient brain areas (Gramma and Engert, 2012; Ramdya and Engert, 2008).

Previous work suggests that visual stabilization behaviors are driven by the caudal pretectum (Naumann et al., 2016; Wang

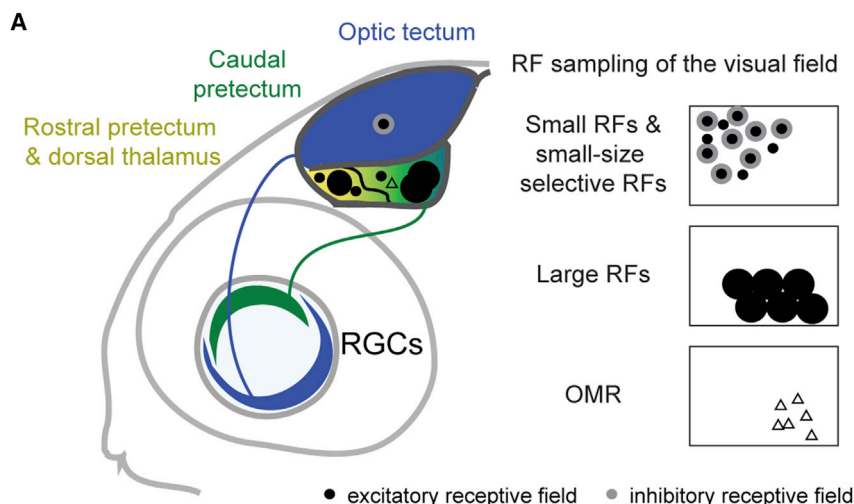


Figure 5. Illustration of the Major Anatomical Locations and Visual Field Preferences of the Characterized Functional Cell Types

The tectum mainly contains small-size-selective RFs, whereas a distribution of different RFs is observed in the PT and dorsal thalamus, ranging from small-size-selective (mainly in the rostral PT and dorsal thalamus) to large-size RFs (mainly in the caudal PT). Previous findings suggest that tectum and caudal PT receive direct retinal inputs (solid lines). To the right, the visual field distributions of RF centers are shown for each functional cell type. An additional visual field map is shown for OMR behavior, in which the regions driving OMR best are indicated. In the visual field maps, the horizontal axis (left-right) corresponds to the nasal-temporal spatial locations and the vertical axis to the upper and lower visual field locations.

et al., 2019; Kubo et al., 2014), which we show contains neurons of different RF sizes. Both whole-field and small-size optic flow stimuli evoke robust OMR tail beats, suggesting that both pretectal large-size and small-size RF neurons might form the basis for optic flow processing underlying the OMR. In agreement with this possibility, the RF centers of both pretectal large-size and small-size RFs match the bias of OMR drive to lower visual field locations (Figures S5E, S6E, and S6F). Further work is needed to identify the relative contributions of large-size RF and small-size RF pretectal neurons to OMR behavior.

In summary, we mapped the RFs of zebrafish tectal and pretectal neurons and demonstrated that both brain areas fulfill complementary roles for visual motion feature extraction. RFs of tectal neurons are predominantly small and size selective and have a strong bias in representing the upper nasal visual field (Figure 5). In contrast, caudal pretectal neurons have predominantly larger RFs with RF centers preferentially located in the lower visual field of the animal, which corresponds to the location of strongest OMR drive in the lower temporal visual field. Thus, each tectal and pretectal brain region extracts different motion stimulus features and samples distinct visual field regions. We speculate that this anisotropic visual field sampling in the tectum and pretectum could represent adaptations of zebrafish to feeding and stabilization behaviors, resulting in efficient usage of visual brain area volumes for the representation of behaviorally relevant stimulus features. Our study reveals the sensory layout of motion processing and, thus, constitutes an important advance for deriving a biologically faithful model of visuomotor transformations in zebrafish.

STAR★METHODS

Detailed methods are provided in the online version of this paper and include the following:

- KEY RESOURCES TABLE
- LEAD CONTACT AND MATERIALS AVAILABILITY

● EXPERIMENTAL MODEL AND SUBJECT DETAILS

- Animal care and transgenic lines

● METHOD DETAILS

- Animal preparation (tectal and pretectal imaging of neuronal somata)
- 2-photon microscopy of somatic calcium responses
- LED arena for visual stimulation (Figures 1, 2, 3, and 4)
- Identification of regions of interest (imaging of neuronal somata)
- Defining the borders of the tectum in our 3D datasets
- Registration of 3D pretectal volume from Z Brain atlas (related to Figure S6)
- Movies of 3D brain volumes with neurons shown inside
- Monocular receptive field mapping
- Inclusion criteria for somatic calcium responses
- Setup for measuring the receptive field of OMR behavior
- Receptive field mapping of OMR behavior

● QUANTIFICATION AND STATISTICAL ANALYSIS

● DATA AND CODE AVAILABILITY

SUPPLEMENTAL INFORMATION

Supplemental Information can be found online at <https://doi.org/10.1016/j.celrep.2019.12.031>.

ACKNOWLEDGMENTS

We thank Väinö Haikala and Dierk F. Reiff for help with the visual stimulus arena. The identification of the anatomical position of pretectal dopaminergic neurons was conducted in collaboration with Wolfgang Driever and Christian Altbürger, who provided anatomical z stacks of a double-transgenic dopaminergic line (unpublished data; see Fernandes et al., 2012 and Reinig et al., 2017). Furthermore, we thank Thomas Nieß (glassblower shop, University of Tübingen) and Klaus Vollmer (fine mechanics workshop, University Clinic Tübingen) for technical support, Prudenter-Agas (Hamburg, Germany) for generating illustrations, and Julianne Skinner for contributing to the analysis of RF center distribution. We thank Martin Meyer for feedback on a previous version of the manuscript. This work was funded by Deutsche Forschungsgemeinschaft (DFG) grants EXC307 (CIN-Werner Reichardt Centre

for Integrative Neuroscience) and INST 37/967-1 FUGG and Human Frontier Science Program (HFSP) Young Investigator grant RGY0079.

AUTHOR CONTRIBUTIONS

K.W. performed the experiments on pretectal and tectal somatic responses. K.W., J.H., and Y.Z. analyzed the data. A.B.A., K.W., J.H., and T.R.T. conceived the experiments and associated analysis protocols. K.W., J.H., and A.B.A. wrote the manuscript, with input from T.R.T.

DECLARATION OF INTERESTS

The authors declare no competing interests.

Received: May 17, 2019

Revised: July 27, 2019

Accepted: December 9, 2019

Published: January 14, 2020

REFERENCES

- Ahrens, M.B., Huang, K.H., Narayan, S., Mensh, B.D., and Engert, F. (2013a). Two-photon calcium imaging during fictive navigation in virtual environments. *Front. Neural Circuits* 7, 104.
- Ahrens, M.B., Orger, M.B., Robson, D.N., Li, J.M., and Keller, P.J. (2013b). Whole-brain functional imaging at cellular resolution using light-sheet microscopy. *Nat. Methods* 10, 413–420.
- Arrenberg, A.B., and Driever, W. (2013). Integrating anatomy and function for zebrafish circuit analysis. *Front. Neural Circuits* 7, 74.
- Attardi, D.G., and Sperry, R.W. (1963). Preferential selection of central pathways by regenerating optic fibers. *Exp. Neurol.* 7, 46–64.
- Baden, T., Berens, P., Franke, K., Román Rosón, M., Bethge, M., and Euler, T. (2016). The functional diversity of retinal ganglion cells in the mouse. *Nature* 529, 345–350.
- Baier, H., Klostermann, S., Trowe, T., Karlstrom, R.O., Nüsslein-Volhard, C., and Bonhoeffer, F. (1996). Genetic dissection of the retinotectal projection. *Development* 123, 415–425.
- Beck, J.C., Gilland, E., Tank, D.W., and Baker, R. (2004). Quantifying the ontogeny of optokinetic and vestibuloocular behaviors in zebrafish, medaka, and goldfish. *J. Neurophysiol.* 92, 3546–3561.
- Bergmann, K., Meza Santoscoy, P., Lygdas, K., Nikolaeva, Y., MacDonald, R.B., Cunliffe, V.T., and Nikolaev, A. (2018). Imaging Neuronal Activity in the Optic Tectum of Late Stage Larval Zebrafish. *J. Dev. Biol.* 6, E6.
- Bianco, I.H., Kampff, A.R., and Engert, F. (2011). Prey capture behavior evoked by simple visual stimuli in larval zebrafish. *Front. Syst. Neurosci.* 5, 101.
- Boulanger-Weill, J., Candat, V., Jouary, A., Romano, S.A., Perez-Schuster, V., and Sumbre, G. (2017). Functional Interactions between Newborn and Mature Neurons Leading to Integration into Established Neuronal Circuits. *Curr. Biol.* 27, 1707–1720.e5.
- Britto, L.R., Natal, C.L., and Marcondes, A.M. (1981). The accessory optic system in pigeons: receptive field properties of identified neurons. *Brain Res.* 206, 149–154.
- Busch, C., Borst, A., and Mauss, A.S. (2018). Bi-directional Control of Walking Behavior by Horizontal Optic Flow Sensors. *Curr. Biol.* 28, 4037–4045.e5.
- Chen, T.W., Wardill, T.J., Sun, Y., Pulver, S.R., Renninger, S.L., Baohan, A., Schreiter, E.R., Kerr, R.A., Orger, M.B., Jayaraman, V., et al. (2013). Ultrasensitive fluorescent proteins for imaging neuronal activity. *Nature* 499, 295–300.
- Cowey, A., and Rolls, E.T. (1974). Human cortical magnification factor and its relation to visual acuity. *Exp. Brain Res.* 21, 447–454.
- Dehmelt, F.A., Meier, R., Hinz, J., Yoshimatsu, T., Simacek, C.A., Wang, K., Baden, T., and Arrenberg, A.B. (2019). Spherical arena reveals optokinetic response tuning to stimulus location, size and frequency across entire visual field of larval zebrafish. *bioRxiv*. <https://doi.org/10.1101/754408>.
- Engeszer, R.E., Patterson, L.B., Rao, A.A., and Parichy, D.M. (2007). Zebrafish in the wild: a review of natural history and new notes from the field. *Zebrafish* 4, 21–40.
- Euler, T., Susanne, H., E., Margolis, D., J., Breuninger, T., Castell, X., Detwiler, P., B., and Denk, W. (2009). Eyecup scope—optical recordings of light stimulus-evoked fluorescence signals in the retina. *Pflügers Archiv - European Journal of Physiology* 457, 1393–1414.
- Fernald, R.D., and Shelton, L.C. (1985). The organization of the diencephalon and the pretectum in the cichlid fish, *Haplochromis burtoni*. *J. Comp. Neurol.* 238, 202–217.
- Fernandes, A.M., Fero, K., Arrenberg, A.B., Bergeron, S.A., Driever, W., and Burgess, H.A. (2012). Deep brain photoreceptors control light-seeking behavior in zebrafish larvae. *Curr. Biol.* 22, 2042–2047.
- Filippi, A., Mueller, T., and Driever, W. (2014). *vglut2* and *gad* expression reveal distinct patterns of dual GABAergic versus glutamatergic cotransmitter phenotypes of dopaminergic and noradrenergic neurons in the zebrafish brain. *J. Comp. Neurol.* 522, 2019–2037.
- Gahtan, E., Tanger, P., and Baier, H. (2005). Visual prey capture in larval zebrafish is controlled by identified reticulospinal neurons downstream of the tectum. *J. Neurosci.* 25, 9294–9303.
- Giolli, R.A., Blanks, R.H., and Lui, F. (2006). The accessory optic system: basic organization with an update on connectivity, neurochemistry, and function. *Prog. Brain Res.* 151, 407–440.
- Grama, A., and Engert, F. (2012). Direction selectivity in the larval zebrafish tectum is mediated by asymmetric inhibition. *Front. Neural Circuits* 6, 59.
- Grasse, K.L., and Cynader, M.S. (1984). Electrophysiology of lateral and dorsal terminal nuclei of the cat accessory optic system. *J. Neurophysiol.* 51, 276–293.
- Grujic, N., Brehm, N., Gloge, C., Zhuo, W., and Hafed, Z.M. (2018). Perisaccadic perceptual mislocalization is different for upward saccades. *J. Neurophysiol.* 120, 3198–3216.
- Hafed, Z.M., and Chen, C.Y. (2016). Sharper, Stronger, Faster Upper Visual Field Representation in Primate Superior Colliculus. *Curr. Biol.* 26, 1647–1658.
- Haikala, V., Joesch, M., Borst, A., and Mauss, A.S. (2013). Optogenetic control of fly optomotor responses. *J. Neurosci.* 33, 13927–13934.
- Hunter, P.R., Lowe, A.S., Thompson, I.D., and Meyer, M.P. (2013). Emergent properties of the optic tectum revealed by population analysis of direction and orientation selectivity. *J. Neurosci.* 33, 13940–13945.
- Joesch, M., Plett, J., Borst, A., and Reiff, D.F. (2008). Response properties of motion-sensitive visual interneurons in the lobula plate of *Drosophila melanogaster*. *Curr. Biol.* 18, 368–374.
- Karmeier, K., Krapp, H.G., and Egelhaaf, M. (2003). Robustness of the tuning of fly visual interneurons to rotatory optic flow. *J. Neurophysiol.* 90, 1626–1634.
- Kastenhuber, E., Kratochwil, C.F., Ryu, S., Schweitzer, J., and Driever, W. (2010). Genetic dissection of dopaminergic and noradrenergic contributions to catecholaminergic tracts in early larval zebrafish. *J. Comp. Neurol.* 518, 439–458.
- Krapp, H.G., Hengstenberg, R., and Egelhaaf, M. (2001). Binocular contributions to optic flow processing in the fly visual system. *J. Neurophysiol.* 85, 724–734.
- Kubo, F., Hablitzel, B., Dal Maschio, M., Driever, W., Baier, H., and Arrenberg, A.B. (2014). Functional architecture of an optic flow-responsive area that drives horizontal eye movements in zebrafish. *Neuron* 81, 1344–1359.
- Marques, J.C., Lackner, S., Felix, R., and Orger, M.B. (2018). Structure of the Zebrafish Locomotor Repertoire Revealed with Unsupervised Behavioral Clustering. *Curr. Biol.* 28, 181–195.e5.
- Masseck, O.A., and Hoffmann, K.P. (2008). Responses to moving visual stimuli in pretectal neurons of the small-spotted dogfish (*Scyliorhinus canicula*). *J. Neurophysiol.* 99, 200–207.

- Miri, A., Daie, K., Burdine, R.D., Aksay, E., and Tank, D.W. (2011). Regression-based identification of behavior-encoding neurons during large-scale optical imaging of neural activity at cellular resolution. *J. Neurophysiol.* *105*, 964–980.
- Muto, A., Lal, P., Ailani, D., Abe, G., Itoh, M., and Kawakami, K. (2017). Activation of the hypothalamic feeding centre upon visual prey detection. *Nat. Commun.* *8*, 15029.
- Nassi, J.J., and Callaway, E.M. (2009). Parallel processing strategies of the primate visual system. *Nat. Rev. Neurosci.* *10*, 360–372.
- Naumann, E.A., Fitzgerald, J.E., Dunn, T.W., Rihel, J., Sompolinsky, H., and Engert, F. (2016). From Whole-Brain Data to Functional Circuit Models: The Zebrafish Optomotor Response. *Cell* *167*, 947–960.e20.
- Niell, C.M., and Smith, S.J. (2005). Functional imaging reveals rapid development of visual response properties in the zebrafish tectum. *Neuron* *45*, 941–951.
- Orger, M.B., Kampff, A.R., Severi, K.E., Bollmann, J.H., and Engert, F. (2008). Control of visually guided behavior by distinct populations of spinal projection neurons. *Nat. Neurosci.* *11*, 327–333.
- Pologruto, T.A., Yasuda, R., and Svoboda, K. (2004). Monitoring neural activity and [Ca²⁺] with genetically encoded Ca²⁺ indicators. *J. Neurosci.* *24*, 9572–9579.
- Portugues, R., and Engert, F. (2009). The neural basis of visual behaviors in the larval zebrafish. *Curr. Opin. Neurobiol.* *19*, 644–647.
- Presson, J., Fernald, R.D., and Max, M. (1985). The organization of retinal projections to the diencephalon and pretectum in the cichlid fish, *Haplochromis burtoni*. *J. Comp. Neurol.* *235*, 360–374.
- Preuss, S.J., Trivedi, C.A., vom Berg-Maurer, C.M., Ryu, S., and Bollmann, J.H. (2014). Classification of object size in retinotectal microcircuits. *Curr. Biol.* *24*, 2376–2385.
- Ramdya, P., and Engert, F. (2008). Emergence of binocular functional properties in a monocular neural circuit. *Nat. Neurosci.* *11*, 1083–1090.
- Randlett, O., Wee, C.L., Naumann, E.A., Nnaemeka, O., Schoppik, D., Fitzgerald, J.E., Portugues, R., Lacoste, A.M., Riegler, C., Engert, F., and Schier, A.F. (2015). Whole-brain activity mapping onto a zebrafish brain atlas. *Nat. Methods* *12*, 1039–1046.
- Recher, G., Jouralet, J., Brombin, A., Heuzé, A., Mugniery, E., Hermel, J.M., Desnoullez, S., Savy, T., Herbomel, P., Bourrat, F., et al. (2013). Zebrafish midbrain slow-amplifying progenitors exhibit high levels of transcripts for nucleotide and ribosome biogenesis. *Development* *140*, 4860–4869.
- Reinig, S., Driever, W., and Arrenberg, A.B. (2017). The Descending Diencephalic Dopamine System Is Tuned to Sensory Stimuli. *Curr. Biol.* *27*, 318–333.
- Reiser, M.B., and Dickinson, M.H. (2008). A modular display system for insect behavioral neuroscience. *J. Neurosci. Methods* *167*, 127–139.
- Rinner, O., Rick, J.M., and Neuhauss, S.C. (2005). Contrast sensitivity, spatial and temporal tuning of the larval zebrafish optokinetic response. *Invest. Ophthalmol. Vis. Sci.* *46*, 137–142.
- Robles, E., Laurell, E., and Baier, H. (2014). The retinal projectome reveals brain-area-specific visual representations generated by ganglion cell diversity. *Curr. Biol.* *24*, 2085–2096.
- Romano, S.A., Pietri, T., Pérez-Schuster, V., Jouary, A., Haudrechy, M., and Sumbre, G. (2015). Spontaneous neuronal network dynamics reveal circuit's functional adaptations for behavior. *Neuron* *85*, 1070–1085.
- Ronneberger, O., Liu, K., Rath, M., Rueß, D., Mueller, T., Skibbe, H., Drayer, B., Schmidt, T., Filippi, A., Nitschke, R., et al. (2012). ViBE-Z: a framework for 3D virtual colocalization analysis in zebrafish larval brains. *Nat. Methods* *9*, 735–742.
- Rupp, B., Wullmann, M.F., and Reichert, H. (1996). The zebrafish brain: a neuroanatomical comparison with the goldfish. *Anat. Embryol. (Berl.)* *194*, 187–203.
- Sajovic, P., and Levinthal, C. (1982). Visual cells of zebrafish optic tectum: mapping with small spots. *Neuroscience* *7*, 2407–2426.
- Schmitt, E.A., and Dowling, J.E. (1999). Early retinal development in the zebrafish, *Danio rerio*: light and electron microscopic analyses. *J. Comp. Neurol.* *404*, 515–536.
- Schwartz, E.L. (1980). Computational anatomy and functional architecture of striate cortex: a spatial mapping approach to perceptual coding. *Vision Res.* *20*, 645–669.
- Semmelhack, J.L., Donovan, J.C., Thiele, T.R., Kuehn, E., Laurell, E., and Baier, H. (2014). A dedicated visual pathway for prey detection in larval zebrafish. *eLife* *9*, 3.
- Severi, K.E., Portugues, R., Marques, J.C., O'Malley, D.M., Orger, M.B., and Engert, F. (2014). Neural control and modulation of swimming speed in the larval zebrafish. *Neuron* *83*, 692–707.
- Simpson, J.I. (1984). The accessory optic system. *Annu. Rev. Neurosci.* *7*, 13–41.
- Spillmann, L. (2014). Receptive fields of visual neurons: the early years. *Perception* *43*, 1145–1176.
- Tay, T.L., Ronneberger, O., Ryu, S., Nitschke, R., and Driever, W. (2011). Comprehensive catecholaminergic projectome analysis reveals single-neuron integration of zebrafish ascending and descending dopaminergic systems. *Nat. Commun.* *2*, 171.
- Thiele, T.R., Donovan, J.C., and Baier, H. (2014). Descending control of swim posture by a midbrain nucleus in zebrafish. *Neuron* *83*, 679–691.
- Trowe, T., Klostermann, S., Baier, H., Granato, M., Crawford, A.D., Grunewald, B., Hoffmann, H., Karlstrom, R.O., Meyer, S.U., Müller, B., et al. (1996). Mutations disrupting the ordering and topographic mapping of axons in the retinotectal projection of the zebrafish, *Danio rerio*. *Development* *123*, 439–450.
- Walley, R.E. (1967). Receptive fields in the accessory optic system of the rabbit. *Exp. Neurol.* *17*, 27–43.
- Wang, K., Hinz, J., Haikala, V., Reiff, D.F., and Arrenberg, A.B. (2019). Selective processing of all rotational and translational optic flow directions in the zebrafish pretectum and tectum. *BMC Biol.* *17*, 29.
- Yamamoto, K., and Vernier, P. (2011). The evolution of dopamine systems in chordates. *Front. Neuroanat.* *5*, 21.
- Yáñez, J., Suárez, T., Quelle, A., Folgueira, M., and Anadón, R. (2018). Neural connections of the pretectum in zebrafish (*Danio rerio*). *J. Comp. Neurol.* *526*, 1017–1040.
- Zhang, M., Liu, Y., Wang, S.Z., Zhong, W., Liu, B.H., and Tao, H.W. (2011). Functional elimination of excitatory feedforward inputs underlies developmental refinement of visual receptive fields in zebrafish. *J. Neurosci.* *31*, 5460–5469.
- Zimmermann, M.J.Y., Nevala, N.E., Yoshimatsu, T., Osorio, D., Nilsson, D.E., Berens, P., and Baden, T. (2018). Zebrafish Differentially Process Color across Visual Space to Match Natural Scenes. *Curr. Biol.* *28*, 2018–2032.e5.

STAR★METHODS

KEY RESOURCES TABLE

REAGENT or RESOURCE	SOURCE	IDENTIFIER
Chemicals, Peptides, and Recombinant Proteins		
α -bungarotoxin	Sigma-Aldrich	T0195-.5MG
Poly-L-lysine solution	Sigma-Aldrich	P4832-50ML
Experimental Models: Organisms/Strains		
Zebrafish <i>Tg(HuC:GCaMP5G)a4598Tg</i>	Ahrens et al., 2013b	N/A
Zebrafish <i>Tg(th-E2A-QF2)m1512 x Tg(QUAS: EGFP)</i>	Driever lab (Freiburg University)	N/A
Software and Algorithms		
ImageJ/Fiji	NIH	https://fiji.sc
MATLAB R2010b, R2014b, R2015b	MathWorks	https://www.mathworks.com/products/matlab.html
LabVIEW 2015	National Instruments	http://www.ni.com/en-us/shop/labview.html
Mscan	Sutter Instrument	https://www.sutter.com/MICROSCOPES/mcs.html
Other		
Z-Brain Atlas	Randlett et al., 2015	https://engertlab.fas.harvard.edu/Z-Brain/

LEAD CONTACT AND MATERIALS AVAILABILITY

Further information and requests for resources and reagents should be directed to and will be fulfilled by the Lead Contact Aristides Arrenberg (aristides.arrenberg@uni-tuebingen.de).

EXPERIMENTAL MODEL AND SUBJECT DETAILS

Animal care and transgenic lines

All animal procedures conformed to the institutional guidelines of the Universities of Tübingen and Freiburg and the local government (Regierungspräsidium Tübingen and Regierungspräsidium Freiburg, respectively). The transgenic zebrafish lines *Tg(HuC:GCaMP5G)a4598Tg* and the unpublished double transgenic line *Tg(th-E2A-QF2)m1512 x Tg(QUAS: EGFP)* (Fernandes et al., 2012; Reinig et al., 2017) were used in this study. Transgenic lines were kept in either a TL or TLN (nacre) background. Zebrafish larvae were raised in E3 medium until day 5 or 6 post-fertilization (dpf).

METHOD DETAILS

Animal preparation (tectal and pretectal imaging of neuronal somata)

At the day of experiments (5 or 6 dpf), larvae were transferred into a Petri dish and embedded in low melting agarose (E3 medium). The agarose surrounding the eyes was not removed as to minimize the range of possible eye movements. 6 animals received an injection of α -bungarotoxin into the caudal vein to paralyze them and prevent eye movements and motion artifacts. 4 animals were recorded without paralysis. In addition, 6 animals were recorded without paralysis in another independent experiment and exclusively used for the analyses presented in the Figures S1B, S1C, S4B, and S4F. The animals were then transferred and mounted in agarose on a glass triangle and the fish head protruded the point of the glass triangle, so that the eyes could see through the (agarose and) water clearly. The agarose surrounding the fish head was trimmed on the sides and in front of the animal to reduce the amount of surrounding agarose (Figure S1F). However, the eyes were still covered by agarose to minimize the range of possible eye movements. The glass triangle was held from the back by a 5 mm thin shaft which was fixed to an 8 cm diameter glass bulb (made by a glass blower) filled with E3 medium. The glass bulb resembled a consumer market light bulb (threading of the light bulb/glass bulb shaft at the back of the fish) and a 5 cm diameter hole was cut on the top of the spherical part to allow for approach of the microscope objective onto the fish (Figure S1F). From stimulus arena to the fish eye, the light traveled through air, glass (light hit glass roughly orthogonally in the spherical part as to minimize refraction of light rays), water, and finally agarose. The glass bulb was fixed with its shaft (15.5 mm diameter) to the metal holder which allowed for pitch and yaw adjustments (the glass shaft allowed for adjustments in roll). In the first batches of receptive field mapping (n = 6 larvae) experiments, we noticed a problem regarding reflections on the glass bulb on the opposite side

of stimulation, resulting in detected neurons on the ipsilateral side of (intended) stimulation in the tectum (which were not plotted in Figure 3). In the second set of recordings (4 larvae), we wrapped a piece of black, half-cylindrical aluminum foil around the objective. The black aluminum foil was then lowered beyond the eye contralateral to the stimulus to prevent this eye from seeing the reflections. In these recordings, only very few ipsilateral tectal neurons were detected (and were not excluded in the anatomical registration figures). Both sets of recordings were included in data analysis, because only few additional neurons were detected due to the reflections in the ipsilateral tectum, suggesting that the vast majority of the detected neurons of the contralateral side were detected due to the stimulus presented to the intended eye.

2-photon microscopy of somatic calcium responses

Calcium imaging was performed with a two-photon microscopy setup based on the MOM microscope (Sutter Instruments; Euler et al., 2009), using a Coherent Vision-S Ti-Sa laser and a 20x/1.0 Zeiss objective to image calcium signals in the transgenic fish line HuC:GCaMP5G (*Tg(elavl3:GCaMP5G)a4598*) (Ahrens et al., 2013b). Calcium time series were recorded at 2 frames per second, with an image size of 512 × 512 pixels and 2 x magnifications, at 920 nm, pre-pulse compensation set to 9756 fs². The midbrain and diencephalon were sampled from +60 μm below the landmark (posterior commissure) to –80 μm above the landmark. Optical slices were taken every 20 μm in the dorso-ventral direction in individual fish and across individual fish, and all dorso-ventral positions were recorded in 10 μm increments relative to the landmark (i.e., no recording at e.g., 5 or 15 μm below the landmark). Since we only recorded every 10 μm in dorso-ventral extent, more than twice as many neurons should have been detectable in the respective brain areas, had we sampled the brain areas at optimal spacing given the neuron soma diameter of ca. 5 μm. Where specified, error bars correspond to measures per completely imaged brain volume. Care was taken to record the same number of slices in each anatomical region. Two animals were used to image one complete brain volume (at 10 μm spacing). Due to the long recording times and positioning instability (likely resulting from the fish drifting within its agarose embedding), we corrected position drifts along the optical axis manually during the recording (mostly less than 4 μm per 30 minutes). Using the 20x objective and a magnification of 2x, our spatial resolution was 0.43 μm/pixel on the x axis (medial-lateral) and the y axis (anterior-posterior).

LED arena for visual stimulation (Figures 1, 2, 3, and 4)

Visual stimulation of zebrafish was conducted with a cylindrical LED arena consisting of 14336 LEDs (Kingbright TA08-81CGKWA): 2 (arena halves) × 8 (rows) × 14 (columns) × 64 (8x8 multiplexed LED matrix) LEDs. The caudal-most column of each arena half was removed without LEDs (i.e., 14, not 15 columns), since the space was needed for the glass bulb stage metal holder. Therefore, the caudal-most stimulus patches were slightly cropped (18° azimuth instead of 30° azimuth for the last patch). The arena covered –168° to +168° in azimuth and –40° to 40° in elevation. A few degrees in angle of the dorsal field of view were likely blocked by the objective due to its access angle of 38.39° (< 40°), however the eyes were located ~200 μm below the objective focus which should have resulted in a maximal viewing angle exceeding 38.39° (i.e., 39.2°). The LEDs emitted at 570 nm and an additional high-pass filter foil (LEE no. 779, article 595-1700-7790, castinfo.de, Hagen, Germany) and diffusion filter foil (LEE no. 252, article 595-1780-2520) were placed in front of the arena to optimize GCaMP signal detection and make the stimulus appear more homogeneous. This resulted in a yellow appearance of the stimulus. The LED arena was controlled as described previously (Joesch et al., 2008; Reiser and Dickinson, 2008). LEDs lit during fly-back time of the scanning mirrors.

Identification of regions of interest (imaging of neuronal somata)

For analysis of neuronal activity, a custom MATLAB script (MOM Load) identified regions based on their correlation to the stimulus and ROIs were manually drawn as described previously (Kubo et al., 2014; Miri et al., 2011). The 3-dimensional mapping of cell location was performed using custom written MATLAB scripts (Midbrain_Localizer and Cell_Viewer), which allowed to register the 2 dimensional recordings to a 3D z stack which was acquired after recording sessions (Kubo et al., 2014). See Figure S4 from Kubo et al. (2014) for an illustration of the 3-dimensional mapping procedure.

Defining the borders of the tectum in our 3D datasets

To distinguish pretectal from tectal neurons, we proceeded as follows: For each fish, the whole z stack – which was imaged from the top of tectum to deep ventral pretectum and dorsal thalamus – was resliced to generate a transverse view. On selected, regularly spaced transverse planes (more than ~50 planes), the ventral border of the tectum was drawn: on each of these transverse plane (512 pixels from left to right, x dimension), a curve was drawn through the area devoid of neuronal somata or fluorescence that was ventrally adjacent to periventricular tectal area with densely packed, fluorescent somata. From each curve, 51 homogeneously distributed points were selected as key points with which a new boundary curve was generated by linear interpolation or three-term Gaussian fitting. Using this method, we obtained a boundary curve with 512 data points corresponding to the pixels in x/y dimensions (left-right and dorsal-ventral) for each transverse plane. In-between the annotated transverse planes, the 2D curves were interpolated to receive a surface that separated the tectum from the pretectum in all three dimensions (Wang et al., 2019). However, the boundaries between the caudal pretectum and adjacent brain areas in the posterior side (tegmentum) were not clearly visible in the GCaMP5G fish line. Referring to the AMC structure reported before (Kubo et al., 2014), and to the anatomical annotations of the

caudally adjacent tegmentum (Ronneberger et al., 2012; Randlett et al., 2015), the neurons below the tectal-pretectal boundary drawn above, which were located more than 140 μm caudally to the posterior commissure, were excluded from the pretectum in the current study.

Registration of 3D pretectal volume from Z Brain atlas (related to Figure S6)

The pretectal region mask, obtained from datasets MaskDatabase.mat and Ref20131120pt14pl2.nrrd (Z Brain atlas, <https://engertlab.fas.harvard.edu/Z-Brain/download>) was used as the standard brain corresponding to the pretectal region mask.

- (1) The brain regions corresponding to our recordings (mainly tectum and dorsal diencephalon) were cropped out from the standard brain (size 282 \times 282, pixel \times pixel; 1 pixel = 0.798 μm). The cropped image was resized to 512 \times 512 (1 pixel = 0.43 μm) to match our image size and scale.
- (2) The standard coordinate system which we use in our zebrafish brain was drawn in the standard brain of the Z Brain atlas (Figure S4 from Kubo et al., 2014). The relative locations of the pretectal region boundary to the point of origin (0, 0, 0) were calculated.
- (3) The angle of the pretectal neuropil from the standard brain of the Z Brain atlas was measured with ImageJ. Compared to the standard pretectal neuropil angle of our own recordings (17.4 $^\circ$), the corresponding angle of the standard brain from the Z Brain atlas is pitched up, with a pretectal neuropil angle of 36.5 $^\circ$. Therefore, the pretectal region mask was rotated to register with our standard fish brain.
- (4) The pretectal volume was plotted with MATLAB with the rotated data.

Movies of 3D brain volumes with neurons shown inside

The cell locations (e.g., the colored balls in Figure 2A) were registered to the 3D matrix which corresponds to a z stack of one larval brain, with the intersection point of the first two landmark lines as coordinate origin (0, 0, 0). In the 3D matrix, 3D spheres representing the neurons were plotted and the new 3D matrix was saved as an image series. Then the new image series and the standard zebrafish brain image series were merged with ImageJ. 3D brain volumes with neurons highlighted in different colors were generated with '3D Viewer' in ImageJ.

Monocular receptive field mapping

In the monocular receptive field mapping experiments, we used horizontally moving gratings, 0.033 cycles/ $^\circ$, moving at 30 $^\circ$ /s, as visual stimuli to induce the neural activities. 8 fish were recorded using naso-temporal motion, and 2 fish were recorded using temporal-nasal motion. The data was pooled because we didn't observe obvious difference in RF characteristics (RF size, RF centers). The additional recordings for Figures S1B, S4B, and S4F were performed using both naso-temporal and temporal-nasal motion for 6 fish (3 temporal-nasal and 3 naso-temporal, respectively). Three repetitions of the 57 stimulus phases were shown to the right eye of the fish using one half-cylindrical arena (Figure 1A). All the stimulus patterns were presented in the order depicted in Figure S1A. In each trial, every 4.8 s stimulus phase was preceded by a 4 s pause and followed by a 2 s pause with the same stationary visual stimulus pattern. At the beginning and the end of each repetition, we inserted 9 s pauses.

RF maps for individual neurons were calculated by a series of analysis steps. First, we filter the DFF fluorescence traces with a low pass wavelet decomposition [type Daubechies, MATLAB: `wavedec(DFF,1,'db4')`] and a sliding median filter (the median of three data points). Then deconvolution was performed to the filtered data with the decay time constant (τ) of GCaMP5G, 1.5 s. We calculated the mean of phase-averaged signal (MPAS, averaged over stimulus phase time) from the deconvolved traces. The baseline was defined as the MPAS of all the non-stimulus phases (i.e., without moving stimulus). The standard deviation (STD) of all phase-averaged signals was calculated for the non-motion phases. And the z-score was calculated using the equation:

$$z - score = (MPAS - mean(baseline)) / STD(baseline)$$

We then calculated the median MPAS z-score (i.e., the median across the three repetitions of a stimulus phase of the average of all data points within one stimulus phase).

To determine the size of receptive fields (RFs) of individual cells, we defined 5 subclasses of responses: small-size receptive fields, medium-size receptive fields, large-size receptive fields, bar-shaped receptive fields and double-field receptive fields (containing two discrete excitatory patches in the visual field). Since our stimulation protocol didn't allow for precise mapping of receptive fields (also Gaussian fits for larger receptive fields were problematic), we turned to a broad classification of RF sizes. To this end we used the smallest stimulation field (30 $^\circ$ in azimuth, 13 $^\circ$ in elevation) as a calculation unit (i.e., 1 "patch"). After manual inspection of the receptive field locations, we arbitrarily set the thresholds for the 3 size categories as 3 or less active phases (small, SM), 7 or less active phases (medium, ME) and 8 or more active phases (large, L). Bar cells were classified as having active phases only in the full vertical or full horizontal axis, while "double fields" were classified if they had two peaks of activation that were at least 60 $^\circ$ away from each other. Most double-field receptive fields likely resulted from experimental

artifacts, in which stimulus reflections can cause such double field RFs. Neurons with double-field RFs were therefore excluded from further analysis.

To classify cells according to their respective size criteria, we ran a 2-step process:

Step I

1. Calculate mean patch density (MPD)
 - a. If the cell responded maximally during the small 6x6 stimulus phases, the MPD corresponded to the average normalized activity of the cell in the phases of the 6x6 stimuli.
 - b. If the cell responded maximally for one of the larger stimulus phases, the MPD was calculated as the average normalized activity of the cell in the phases of the 6x6 stimuli that were covered by the field of maximum activation (e.g., the cell in [Figure 1](#) Div had its maximal activity during in the upper horizontal bar stimulus phase, so the mean patch density would correspond to the average activity of the 6 upper patches of the 6x6 stimulation phase).
2. Next, we set the threshold for classifying a part of the visual field as “active” as follows: **IF**
 - a. MPD is smaller than 30%:
 - i. $MPD * 3$
 - b. MPD is larger than 30% and smaller than 40%:
 - i. $MPD * 2$
 - c. MPD is larger than 40%:
 - i. 90%

By relating the activity during the small stimuli to the activity observed during the larger stimuli, these MPD thresholds helped to obtain a more accurate quantification of active patches of cells preferentially active during the small stimulation phases.

3. In *Step I*, cells were classified if following criteria were met:
 - a. The maximum activity in the 6x6 stimulation phase exceeded Mean patch density * factor (see step I.2) **or**
 - b. Maximum excitation in the 6x6 stimulation phase larger than 90%
4. To classify the number of active patches, we applied the threshold defined in **point I.2**

Cells were then either classified as ME or SM based on the number of active patches.

All cells that didn't meet the criteria from point I.3 were classified according to **Step II**. First, we calculated a second metric, the mean excitatory density (MED). We calculated the MED by multiplying the calcium response magnitude for each motion phase (excluding the 36 smallest motion phases) with an area factor (full size x 1, half size x 2 ...), resulting in a motion phase's calcium activity weighted by the visual field area in which the stimulus was moving. We call this parameter the “excitatory density” of the stimulated part of the visual field. A biologically plausible underlying cause for differences in excitatory density is the number of DS RGC inputs the cell receives from the portion of the visual field in which the stimulus moves. We then summed the excitatory densities from all larger stimulation fields together (1x1, 2x1, 1x2, 2x2, 1x6, 6x1) taking into account their spatial location in the visual field. This resulted in an excitatory density map of the complete visual field covered by the stimulus arena. In order to report a single number for the RF size, we then defined active phases as those having 75% or more of the normalized summed maximum activation. The difference between this threshold and the 90% threshold for SM cells is derived from comparing manual and automated classification methods.

This method favors smaller receptive fields, because the calcium indicator only shows disproportionately small fluorescence levels for low levels of calcium activity - i.e., it is non-linear - but it enables easy classification of cells size preferences with the given limitations of the calcium indicator ([Chen et al., 2013](#); [Pologruto et al., 2004](#)).

The results from our analysis, which is based on thresholding and classification, fits well with both the results obtained from an automated approach using PCA and clustering ([Figure S2](#)), and results from manual classification of receptive field sizes.

To determine if cells were small-size selective, we compared the responses to small-size and larger-size stimuli from our stimulus protocol. If (i) a cell was assigned to the small size (SM) or median size (ME) category and was identified during one of the 36 (6x6) small-size stimulation phases (see above), and (ii) the cell showed its maximum activity during the 6x6 stimulation then this cell was classified as being size selective ('Inhibition').

To determine the relative reduction in activity (relative to the response if only the small excitatory receptive field is stimulated) and to visualize the spatial structure of the inhibitory receptive field (“inhibitory density”), we summed the relative reduction of activity (analogous to the above described excitatory density) for every patch belonging to the RF and removed the patches that were part of the RF from the inhibitory field.

Please note that some cells were assigned SM or ME status based on the excitatory density map (and not based on the 36 small-size stimulation phases). We assigned the “no inhibition” status to all of these cells, because the maximal activity was not found in any of the small-size stimulation phases. However, the RFs of these cells could still show some form of inhibition (e.g., during presentation of larger half-field stimulus phases), which was not characterized here. The second cell in [Figure 1](#) Dii (an ME cell) is an example for such cells without assigned “inhibition” status.

We estimated the RF centers in XY space as the center of mass of the normalized activity in the active phases (those with red dots in Figure 1D), i.e., both location and level of activity in active phases determined the position.

The median receptive field size across the visual field was derived by calculating (for every visual field position) the median RF size of receptive fields that covered the respective visual field location to visualize the distribution of RF sizes in the visual space.

LED arena light rays that traveled roughly through the center of the glass bulb (where the fish head was located as well) hit the glass bulb wall on the opposite side with an angle of incidence of 90°. This resulted in about 4% of reflected light (according to the Fresnel equations) and this light was visible to fish eye that was not intended to be stimulated. In the first 6 animals, we noticed an unexpectedly high number of detected ROIs in the optic tectum ipsilateral to the stimulation. The vast majority of these tectal ipsilateral ROIs had a reversed retino-tectal topography indicating that these ROIs were detected because of the reflected light. We decided to exclude these ROIs in the anatomical reconstruction. For the other 4 animals, we blocked the non-stimulated eye by placing a half-cylindrical piece of black aluminum foil around the objective and lowering it below the level of the eye. In these animals, a much smaller number of neurons were detected in the ipsilateral tectum, and their anatomical location corresponded to the expected retino-tectal topography. In the data analysis, the small-size RF neurons in the ipsilateral hemisphere recorded from the first 6 animals were excluded. The laterality index for tectal neurons was -0.88 for the 4 animals with one blocked eye, and -0.46 for the 6 animals in which the eyes were not blocked.

In Figure 3A (locations of RF centers in the visual field for tectal small-size RF cells), only very few cells (55 out of 1074), which have RFs centers in the lower temporal of the visual field, were present. While we are convinced that this finding represents an actual under-representation of such cells in the optic tectum, we would like to discuss two experimental caveats, which can explain the effect partially (but not fully). First, the fish were mounted on a glass triangle and care was taken to allow free view of the stimuli from the position of the eye lenses by pushing the larva toward the tip of the glass triangle (thereby reducing the positional stability of the recording). However, for some animals, a small portion of the lower temporal visual field might have been blocked by the sides of the glass triangle. However, this caveat should only have affected extreme lower-temporal receptive field positions (e.g., $> 120^\circ$ in azimuth and $< -30^\circ$ in elevation). Second, the anatomical positions of those tectal neurons having lower temporal receptive field centers lie close to the border with the pretectum. The pretectum-classified small-size RF cells in proximity of the tectum (shade red dots in Figure 2A) can fill the gap in the ventral-caudal visual field in Figure 3A only partially (just 12 additional cells for the region $> 90^\circ$ azimuth and $< 0^\circ$ elevation) when such pretectal neurons are plotted together with the tectal neurons.

To characterize the distributions of RF centers across visual space, the density of the RF centers in the visual space was calculated with 'ksdensity' function in MATLAB. Contour lines were plotted based on the density.

One gap between the rostral diencephalic and caudal pretectal neurons is quite obvious (Figure 2A). Moreover, in the rostral diencephalon, many neurons are small-size selective (RFs with signs of inhibition). Therefore, a boundary was manually defined between the rostral diencephalon and caudal pretectum along this gap containing only few motion-sensitive neurons (Figure 2A). In the data analysis of the rostral diencephalic neurons, the rostral diencephalon was defined as follows: dorso-ventral axis $< 10 \mu\text{m}$ and anterior-posterior axis $< 60 \mu\text{m}$, or dorso-ventral axis $< -30 \mu\text{m}$ and anterior-posterior axis $< 110 \mu\text{m}$. $140 \mu\text{m}$ caudal to the posterior commissure along the anterior-posterior axis was conceded as the caudal boundary of the pretectum with other brain areas. The bilaterally symmetric anatomical distribution of the neurons relative to the midline was measured using a laterality index, which was calculated as,

$$(\text{neurons}_{\text{right}} - \text{neurons}_{\text{left}}) / (\text{neurons}_{\text{left}} + \text{neurons}_{\text{right}}).$$

Inclusion criteria for somatic calcium responses

We calculated the Pearson's linear correlation coefficients between the stimulus phase z-scores (see above) of the three stimulus protocol repetitions (for all 3 pairwise combinations) to characterize the reproducibility of stimulus-evoked calcium responses. In our further data analysis, we only kept the neurons for which all three correlation coefficients were higher than a certain threshold. The threshold was set between 0.65 and 0.75 to exclude around 30% neurons with low reproducibility of stimulus-evoked activity in the monocular receptive field mapping experiment (2004 out of 2995, 67% neurons were kept). We then performed signal-to-noise ratio (SNR) analysis to exclude neurons with unstable baseline. In the SNR analysis, a threshold of four was used on the z-score to detect positive neural responses. SNR was defined as the ratio of the average response of all the responsive phases to the standard deviation of the baseline. All neurons with SNR lower than a certain threshold were excluded. The threshold was set between 8 and 10 to exclude about 5% remaining neurons with low SNR. We kept about 96% (1926 out of 2004 neurons) in the monocular receptive field mapping experiment for further analysis.

Setup for measuring the receptive field of OMR behavior

The visual stimuli were presented binocularly with a 336° (from -168° to 168° in azimuth) surround LED arena (two half-cylindrical arenas, Figure 4A) from both sides of the fish, i.e., all stimulus phases (except the rotational and looming control stimuli) were mirror-symmetric across the midline. The image of the fish was reflected to a lens by a mirror positioned around 5 cm above the fish (1 cm above the glass bulb). An infrared-sensitive high speed camera (Model IDT iNdustry Speed I, Integrated Design Tools Inc.) with an IR bandpass filter (ET 850/40, CHROMA) recorded (250 Hz) the behaviors of the fish through the lens (diameter,

25.4 mm; focal length, 100mm; THORLABS, LB1676) mentioned above. Since the mirror above the fish is tilted 45 degrees vertically, the light path from the mirror to the camera was horizontal. The fish was illuminated from below with a high power infrared LED light (850 nm, Conrad, Item No. 491248-62) positioned 1 cm below the glass bulb. The infrared light was mounted below a piece of milk glass and provided homogeneous background illumination around the fish (Figure S5A). The infrared LED light and the camera were triggered by the motion signal of the visual stimulus recorded by a LabVIEW DAQ box. In our experiment, the camera started recording about 300 ms after the motion phase onset of the visual stimuli. The infrared LED light was only on during the motion visual stimulus phases to reduce potential harm to the fish.

Receptive field mapping of OMR behavior

For each recording, a larval zebrafish (6 dpf) was transferred into a Petri dish and embedded in low melting agarose (E3 medium) on a glass triangle such that the fish body completely protruded the tip of the glass triangle. The agarose surrounding the larval tail was removed to free the tail. To reduce the amount of agarose surrounding the animal, agarose surrounding the fish was trimmed on the sides and in front. Only the agarose caudal to the animal attached to the triangular stage. Therefore, a large view field was accessible for the fish, and - more importantly - the contours of the beating tail could be imaged without optical obstruction from the glass triangle. The fish and the glass triangle were fixed to an 8 cm diameter glass bulb filled with E3 medium in the same way as described above (see [Animal Preparation](#) in the [Method Details](#) section). The animal was illuminated from below with a high power infrared LED light, which was triggered on 150 ms after the start of the grating motion and lasted for 10 s. During the first 6 s of each grating motion phase (300 ms delay), the animal was imaged with a high speed infrared camera at 250 frames per second. The video data were saved during the pauses and analyzed with custom written MATLAB code offline.

In the OMR behavioral test, forward moving gratings, $0.033 \text{ cycles}^\circ$, moving at $30^\circ/\text{s}$, were used as visual stimuli to induce the optomotor response. Three repetitions of the 55 stimulus phases were shown to both eyes of the fish using two half-cylindrical arenas. All stimulus patterns were presented in each of the three randomized orders depicted in [Figure S5C](#) for the repetitions. The animals were adapted to the stationary gratings for about half an hour before motion stimulation started. In each trial, every 9.75 s stimulus phase was preceded by an 18 s pause and followed by a 51 s pause with the same stationary visual stimulus pattern. Before presenting the 2nd and 3rd repetition of the 55 stimulus phases, the animals rested for about 1 hour.

The motion of the larval tail was traced using a custom MATLAB algorithm for image processing and the 'alpha angle' (the angle between the fish anterior-posterior body axis and the tail tip, see [Figure 4A](#)) was calculated. The single tail beats were detected by labeling the peaks and troughs of the alpha angle traces. In our analysis, only swim beats meeting the following two criteria were considered as forward OMR beats: (1) the tail-beat frequency (during individual swimming bouts) was higher than 25 Hz; (2) for each beat, the difference of the amplitudes of adjacent peaks and troughs divided by the sum of them was smaller than 0.3 and larger than -0.3 (symmetrical tail beats/forward swimming).

Two types of OMR tail beats were distinguished: symmetrical and unsymmetrical tail beats ([Figures 4E](#) and [S5F](#)). Unsymmetrical tail beats oftentimes occurred at the beginning and the end of OMR tail beat bouts ([Figures 4E](#) and [S5F](#)), similar to the case of freely swimming larval zebrafish ([Marques et al., 2018](#)). As expected, the larval zebrafish tried to turn in response to the rotating visual stimulus used as control in our protocol, with tails beating mainly unilaterally to the reverse direction of the rotation ([Ahrens et al., 2013a](#)). However, symmetrical tail beats were observed in the turning swimming bouts as well ([Figure S5Fi](#)).

In [Figure 4](#) (and [Figure S5](#)), the shown tail-beat frequency does not correspond to the frequency reached during individual swim bouts, but instead corresponds to the average frequency during the stimulus phase, such that time periods without swim bouts lead to a reduction of tail-beat frequency.

QUANTIFICATION AND STATISTICAL ANALYSIS

The statistical information calculated with MATLAB R2014b built-in functions is provided in each of the sections above. For statements of significance an alpha level of 0.05 was used unless stated otherwise.

The analyzed number of zebrafish and brains is indicated in the main text and figure legends. Error bars correspond to SEM unless stated otherwise.

DATA AND CODE AVAILABILITY

The scripts for data pre-processing and the pre-processed data are freely available from our G-Node repository (https://gin.g-node.org/Arrenberg_Lab/monocular_receptive_field_mapping). The original raw datasets have not been deposited at G-Node due to the large data size. All raw and processed data and software used to generate the figures will be made available upon request.